Development of a holoscopic imaging system and applied high-resolution fluorescence microscopy

Dissertation

zur Erlangung des akademischen Grades
doctor rerum naturalium (Dr. rer. nat.)

vorgelegt dem Rat der Chemisch-Geowissenschaftlichen Fakultät der Friedrich-Schiller-Universität Jena

von M.Res. Marie Walde
geboren am 17. Juni 1987 in Berlin

Gutachter:
1. Prof. Dr. Rainer Heintzmann, *Friedrich-Schiller-Universität Jena*
2. Prof. Dr. Ute Neugebauer, *Friedrich-Schiller-Universität Jena*

Tag der Verteidigung: 28.06.2017

für Koko

Abstract

Biomedical imaging helps extending our comprehension of ourselves and our environment. Advances in camera, laser and computation technologies have enabled an ever-increasing number of imaging technologies. Imaging with visible and infrared light has the advantage that it is less harmful than other radiation and its wavelength is in the order of magnitude of cells and subcellular components. Fluorescence microscopy provides good chemical contrast and multi-colour imaging can help elucidate cellular architecture. Incoherent superresolution methods permit us to bypass Abbe's diffraction limit of lateral resolution and visualize previously unnoticed details. Coherent imaging methods such as optical coherence tomography or holoscopy do not require any previous labelling and have the advantage that they record both the amplitude and phase of the light emitted from a scattering sample by interferometric superposition with a reference wave. Both incoherent and coherent imaging methods are used in this thesis.

The results of two interdisciplinary research collaborations using different fluorescence microscopy methods, including superresolution methods, are presented. Podosomes in macrophages were studied with stimulated emission depletion microscopy, structured illumination microscopy and localisation microscopy and a distinctly polygonal shape in their vinculin rings was found. Image processing routines allowed for a quantitative analysis of the acquired images [1]. In the second study, chlorophyll, the most prominent natural pigments, and digested chlorophyll metabolites were detected in gut section of the herbivorous *Spodoptera littoralis* larva. Widefield and high-resolution autofluorescence microscopy revealed that the brush border membranes of their gut are covered with the chlorophyllide binding protein tightly bound to the gut membrane. A function in defense against gut microbes is discussed [2].

Optical coherence tomography (OCT) offers a slightly lower spatial resolution than light microscopy but generally better penetration depths. In order to use a higher numerical aperture for detection in OCT, the dilemma of the resulting reduced depth of field has to be overcome. Different extended focus possibilities are explored in this thesis. Bessel illumination is an established method to achieve an extended depth of field without compromising the lateral resolution. When broadband or multicolour imaging is required, wavelength-dependent changes in the radial profile of the Bessel illumination can however complicate further image processing and analysis. A solution for engineering a multicolour Bessel beam was implemented with a phase-only spatial light modulator in the image plane and an iterative Fourier Transformation algorithm [3].

For higher acquisition speed, full-field recording is favourable to scanning the scattering sample with a Bessel beam. OCT can be combined with reconstruction methods from digital holography to achieve an extended focus numerically. A suitable experimental imaging setup and a custom-written reconstruction algorithm are presented.

Zusammenfassung

Biomedizinische Bildgebung hilft unser Verständnis von uns selbst und unserer Umgebung jenseits der Auflösung unseres Auges zu erweitern. Fortschritte in Kamera-, Laser- und Computertechnologien ermöglichen die Entwicklung immer neuer Bildgebungsmethoden. Bildgebung mit sichtbarem und infrarotem Licht hat dabei den Vorteil, dass sie für den Menschen und ähnliche Lebewesen weniger schädlich ist als andere Strahlung und ihre Wellenlänge in der Größenordnung von Zellen und subzellulären Komponenten ist. Fluoreszenzmikroskopie bietet zudem eine sehr spezifische Kontrastmöglichkeit in mehreren Farben, womit zum Beispiel zelluläre Architekturen aufgeklärt werden können. Superauflösende Methoden der inkohärenten Mikroskopie umgehen Abbes Beugungsgrenze der optischen Auflösung und erlauben so die Visualisierung vorher unbemerkter Details. Kohärente Bildgebungsmethoden wie optische Kohärenztomographie oder Holoskopie benötigen keine vorher markierten Proben. Sie haben den Vorteil, dass sowohl die Amplitude als auch die Phase des Lichtes, das von einer Probe gestreut wird, durch interferometrische Überlagerung aufgenommen wird. Für diese Arbeit wurden sowohl inkohärente als auch kohärente Bildgebungsmethoden verwendet.

Die Ergebnisse zweier interdisziplinärer Forschungskollaborationen werden präsentiert, in welchen superauflösende Fluoreszenzmikroskopie verwendet wurde. Podosomen in Makrophagen wurden mittels stimulierter-Emissions-Mikroskopie (STED), strukturierter-Beleuchtungs-Mikroskopie (SIM) und Lokalisations-Mikroskopie untersucht. Dadurch konnten bisher unbekannte polygonale Strukturen in ihren Vinculin-Ringen beobachtet werden. Digitale Bildverarbeitung wurde genutzt, um die Bilder quantitativ zu analysieren [1].
In der zweiten Studie wurden das bedeutendste natürliche Pigment Chlorophyll und seine Metabolite in Darm-Schnitten pflanzenfressender *Spodoptera littoralis*-Larven detektiert. Weitfeld- und hochauflösende Autofluoreszenzmikroskopie offenbarten, dass der Bürstensaum ihrer Därme mit Chlorophyll bedeckt ist. Eine mögliche Funktion in der Mikrobenabwehr wird diskutiert [2].

Optische Kohärenztomographie (OCT) bietet zwar eine etwas niedrigere optische Auflösung als Lichtmikroskopie, aber eine größere Eindringtiefe ins Gewebe. Um eine höhere numerische Apertur in der OCT-Bildgebung zu nutzen, müsste das Dilemma der dadurch verkürzten Feldtiefe beseitigt werden. Verschiedene Ansätze für vergrößerte Feldtiefe werden untersucht. Bessel-Beleuchtung ist eine etablierte Methode, um die Beleuchtungstiefe zu vergrößern ohne die laterale Auflösung zu kompromittieren. Für breitbandige oder mehrfarbige Bildgebung können Wellenlängen-abhängige Veränderungen des radialen Strahlprofils die Bildverarbeitung jedoch erschweren. Eine Lösung zur Erzeugung eines mehrfarbigen Bessel-Strahls mithilfe eines Phasen-Modulators und eines iterativen Fourier-Transformations- Algorithmus wurde implementiert [3].

Für eine schnelle Bilderfassung ist es hingegen vorteilhaft, im Weitfeld-Modus aufzunehmen, anstatt die streuende Probe mit einem Besselstrahl abzuscannen. Hierfür kann OCT mit Rekonstruktionsmethoden aus der digitalen Holographie kombiniert werden, um numerisch einen vergrößerten Fokusbereich zu erzielen. Ein geeignetes experimentelles Bildgebungsystem für entsprechende Aufnahmen wurde gebaut und ein zugehöriger Rekonstruktionsalgorithmus geschrieben.

Contents

List of Figures

List of Tables

Nomenclature

Roman variables

Variable	*Physical quantity*
A	amplitude
APSF($\mathbf{r}$)	amplitude point spread function
ATF($\mathbf{k}$)	amplitude transfer function
$\mathbf{B} = (B_x, B_y, B_z)$	magnetic field
c	speed of light in vacuum
$\mathbf{E} = (E_x, E_y, E_z)$	electric field
D	grating distance
d	distance
d_f	interference fringe spacing
f	focal distance
$g_{+/-}$	constructive/destructive UZI channel
G	coherence function
h	Planck's constant
I	irradiance (also referred to as intensity)
$\mathbf{k} = (k_x, k_y, k_z)$	wave vector
$k = \lvert\mathbf{k}\rvert$	wave number
L	lens
l_c	coherence length
M	magnification
n	refractive index
N	diffraction order
OTF($\mathbf{k}$)	optical transfer function
p	real space propagator
$\tilde{p}$	Fourier space propagator
PSF($\mathbf{r}$)	(intensity) point spread function
R, r	radius
$\mathbf{r}$	spatial vector

S_0, S_1	electronic states
t	time
T	transmittance
v	velocity
w	(Gaussian) beam radius
x, y, z	Cartesian space coordinates

Greek variables

Variable	*Physical quantity*
α	(aperture) angle
γ	constant prefactor
ϵ_λ	molar extinction coefficient
ζ	scattering regime parameter
η	scattering potential
θ	angle
λ	(vacuum) wavelength
μ	attenuation coefficient
μ_a	absorption coefficient
μ	scattering coefficient
ν	optical frequency
ρ	(ring) radius
ϱ	fluorophore density
τ	time delay
Υ	interferogram
φ	angle
ω	angular frequency

Mathematical operators & symbols

Bold font denotes **vectors**.

For $\mathbf{u} = (u_1, u_2, u_3) : \mathbb{C}^3 \rightarrow \mathbb{C}^3$

Symbol	*Meaning*	*Definition*
$\lvert\square\rvert$	Absolute value	$\lvert\mathbf{u}\rvert = \sqrt{u_1^2 + u_2^2 + u_3^2}$
$\square^*$	Complex conjugate	
$f \otimes g$	Convolution	$f(\mathbf{r}) \otimes g(\mathbf{r}) = \int f(\mathbf{r}')g(\mathbf{r} - \mathbf{r}')\,\mathrm{d}\mathbf{r}$
$f \star g$	Crosscorrelation	$f(\mathbf{r}) \otimes g(\mathbf{r}) = \int f(\mathbf{r}')g(\mathbf{r} + \mathbf{r}')\,\mathrm{d}\mathbf{r}$
$\langle\square\rangle$	Expected value	
$\mathcal{F}$ or $\tilde{\square}$	Fourier transform (n: dimension)	$\mathcal{F}\{u(\mathbf{r})\} = \tilde{u}(\mathbf{k}) = \int\limits_{\infty}^{\infty} u(\mathbf{r})\, e^{-\mathrm{i}2\pi\mathbf{k}\cdot\mathbf{r}}\,\mathrm{d}\mathbf{r}$
$\mathcal{F}^{-1}$	Inverse Fourier transform	$\mathcal{F}^{-1}\{\tilde{u}(\mathbf{k})\} = u(\mathbf{r}) = \int\limits_{\infty}^{\infty} \tilde{u}(\mathbf{k})\, e^{-\mathrm{i}2\pi\mathbf{k}\cdot\mathbf{r}}\,\mathrm{d}\mathbf{k}$
$\Re\{\square\}$	Real part	
$\nabla^2\mathbf{u}$	Laplacian operator	$\frac{\partial^2 u_x}{\partial x^2} + \frac{\partial^2 u_y}{\partial y^2} + \frac{\partial^2 u_z}{\partial z^2}$

Abbreviations

1D, 2D, 3D	one-, two-, three-dimensional
3B	Bayesian analysis of blinking and bleaching
AC	auto-correlation
AP	aperture
APSF	amplitude point spread function
ATF	amplitude transfer function
BS	beam splitter
CAM	camera
CC	cross-correlation
CCD	charge-coupled device (imaging sensor)
Chl	chlorophyll
ChlBP	chlorophyll binding protein
CPU	central processing unit
DC	direct current
DH	digital holography
DIP	digital image processing
DOE	diffractive optical element
EM	electromagnetic
FA	field aperture
FM	flip-mount
FOV	field of view
fps	frames per second
FD	Fourier domain
FT	Fourier transformation
FWHM	full width at half-maximum
GPI-anchor	glycophosphatidylinositol
GPU	graphics processing unit
IFT	inverse Fourier transformation
IFTA	iterative Fourier transform algorithm
ISAM	interferometric synthetic aperture microscopy
L	lens
LC-MS	liquid chromatography-mass spectrometry
LCoS	liquid crystal on silicon
LUT	look-up table
MALDI-TOF	matrix-assisted laser desorption/ionization with time-of-flight mass spectrometry
MLD	maximum likelihood deconvolution

MS BLAST	mass spectrometry-driven basic local alignment search tool
NA	numerical aperture
NIR	near infrared
OBJ	objective
OCT	optical coherence tomography
OTF	optical transfer function
PALM	photoactivated localization microscopy
PBS	phosphate-buffered saline
PLC	phospholipase C
POL	polarizer
PSF	point spread function
PVA	polyvinyl alcohol
QWP	quarter-wave plate
REF	reference (arm)
ROI	region of interest
SAM	sample (arm)
SBP	space-bandwidth product
SDS-PAGE	sodium dodecyl sulfate polyacrylamide gel electrophoresis
SIM	structured illumination microscopy
SLM	spatial light modulator
SNR	signal to noise ratio
SS-OCT	swept source optical coherence tomography
STED	stimulated emission depletion
STORM	stochastic optical reconstruction microscopy
TD	time domain
USAF	United States Air Force (resolution target)
UZI	image inversion interferometer

Part I.

Introduction and Background

1

Introduction

From the days of Hooke [4] and Leeuwenhoek [5] to recent advances in superresolution fluorescence microscopy [6], the ability to observe tissues, cells and molecules through the microscope has enabled groundbreaking discoveries in biological and medical research - and repeatedly helped extending and revolutionizing our comprehension of ourselves and our environment.

Important milestones which have sparked a current *golden age of biomedical imaging*[1] include the "discovery and development of the green fluorescent protein" (2008 Nobel Prize in Chemistry) [7] and "the invention of an imaging semiconductor circuit – the CCD sensor" (2009 Nobel Prize in Physics) [8]. This has led to sophisticated optical instrumentation, such as superresolved fluorescence microscopy (2014 Nobel Prize in Chemistry), which provide unprecedented amounts of sample data in both time and space.

Digital optics and image processing play an increasingly important role for advanced imaging schemes, computational image reconstruction and quantitative image analysis and have created a large spectrum of future applications.

Emerging biomedical imaging technologies thus rely on interdisciplinary research drawing from a number of different fields such as cell and molecular biology, medicine, biochemistry, biophotonics, optical physics, informatics and engineering. A central challenge of interdisciplinary research is to establish constructive communication across the sciences. Different approaches to research design and methodology, as well as differing technical vocabularies and disciplinary jargon often need to be consolidated for fruitful collaboration [9].

Although the field is constantly growing with new enabling technologies and physical concepts, no single imaging tool exists that works for all biological and medical questions. Instead, a vast range of biomedical imaging modalities (and combinations thereof) exists which can be compared in terms of spatial resolution, imaging depth, acquisition time, complexity, sample intrusiveness, utilized radiation, contrast mechanism, etc. The first two are plotted for several common imaging methods in Fig. 1.1.

Conventional **optical microscopy** opens a window into spatial structures of a few micrometer to 200 nm. Superresolution fluorescence methods (→ 3.2) have extended this window to the 10 to 100 nm range, approaching the size of biological molecules. This has enabled better insight into protein localizations and molecular

---

[1] Prof. M. Unser, Ecole Polytechnique Fédérale de Lausanne, Biomedical Imaging Group Plenary. *IEEE International Conference on Image Processing (ICIP)*, 27-30 September, 2015, Québec City, Canada.

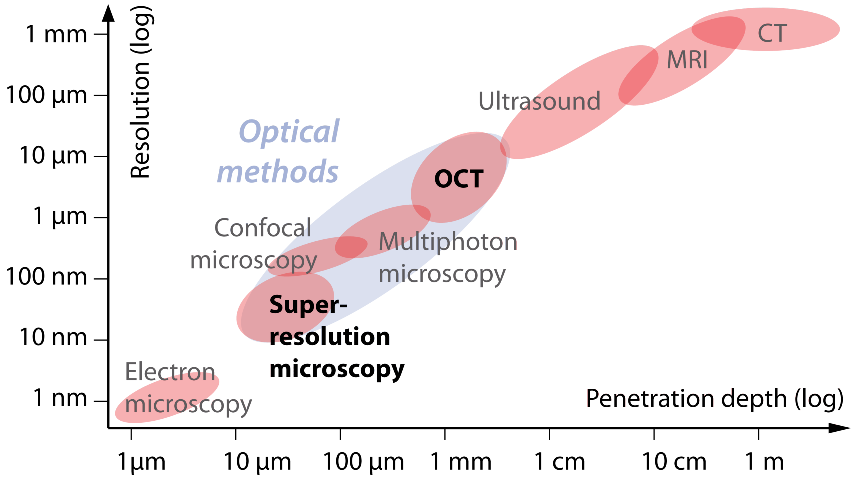

Figure 1.1.: **Typical penetration depth and spatial resolution** for common biomedical imaging methods. Figure modified from [10].

mechanisms on the subcellular level.

A greater penetration depth up to a millimeter into living tissue can be achieved by **two-photon** (TPM) and **multiphoton microscopy** (MPM) due to their longer illumination wavelength [11, 12]. The absorption of two or more photons in the focal layer is a non-linear effect that also provides optical sectioning.

Even smaller features become observable with **electron microscopy**. It does, however, not offer the chemical contrasting possibilities of light microscopy and is not compatible with living samples as sample preparation includes fixation (e.g. by freezing) [6].

For non-invasive insights on the scale of the human body, penetration depths in the centimeter to meter range are required. With **magnetic resonance imaging** (MRI) and **X-ray computed tomography** (CT) entire organs can be visualized and both are routinely used in medical diagnostics. MRI requires long exposure times of several minutes and uses strong magnetic fields and radio waves, neither of which have been proven to cause measurable harm [13]. CT produces cross-sectional images of the body from X-ray images taken at different angles. Due to the utilized ionizing radiation, the benefits of this method need to be weighted against radiation exposure for living humans [14]. The inventors of both methods were awarded a Nobel Prize in Physiology or Medicine (CT 1979, MRI 2003).

Medical **ultrasonography** routinely achieves millimeter resolution at video rate several centimeters deep inside the human body. Ultrasound pulses ($>$20,000 Hz) are sent into tissue and the reflected echoes are collected. Its spatial resolution is limited by the ultrasound wavelength. High-frequency ultrasonography can resolve features as close as 10-100 m at the cost of lower penetration depth. Powers used for imaging have has no proven harmful effects and is applied, for example, in cardiology (using the *Doppler effect*) as well as prenatal diagnostics.

Optical coherence tomography (OCT) occupies a niche between microscopy and ultrasound imaging. OCT was first introduced in 1991 by Hitzensberger et al. [15] and Fujimoto et al. [16]. It addresses applications where ultrasonography lacks resolution, but a deeper penetration or larger field of view than in microscopy is required. OCT probes tissues typically with infrared light. The backscattered and reflected light is recombined with a reference signal. The propagation time of the collected light is a measure of the depth of scattering tissue structures [16]. Cross-sectional images are synthesized from a series of adjacent depth scans.

OCT is usually implemented as a point-scanning technique and thus compatible with endoscopic and catheter-based optics [17]. Unlike ultrasonography, it does not require physical contact with the sample. The most prominent clinical application is ophthalmology [18, 19], but diagnostic fields also include dermatology [20], oncology [21, 22] and gastroenterology [23].

Extended Focus

From Fig. 1.1 a roughly linear correlation in the log-log plot of spatial resolution and penetration depth becomes evident. In OCT, this dilemma is determined by the employed wavelength of light and the numerical aperture of the imaging optics (3.3.4). An obvious solution is to record tomograms with different focal positions and fuse them into a larger focal stack, but this would also increase acquisition time or experimental complexity [24].

Bessel beam illumination is an established method in optical imaging and manipulation to achieve an extended depth of field without compromising the lateral resolution (→ Section 3.5). This has been previously demonstrated for light sheet microscopy [25], dark-field optical coherence microscopy [26, 27] and Optical Tweezers [28].

Bessel beams can be generated with an axicon as well as with a phase mask or computer-generated hologram. Botcherby et al. used a fixed binary phase-only grating in the plane conjugate to the image plane and a narrow annular aperture in the Fourier plane [29].

Instead of the conjugate plane, it is also possible to alter the phase distribution of the incoming light in the Fourier plane of the desired extended beam with a spatial light modulator (SLM) as a hologram [30]. SLMs reflect (or transmit) a light beam while altering its phase distribution. They usually act as a second screen to a computer and the applied discrete phase shift in each pixel can be controlled by displaying grey-level images. This ability to control and change wavefronts is used in beam shaping, pattern formation and aberration correction applications. Working with an SLM permits to correct for wavefront distortions of the incoming beam and optical flatness inaccuracies of the device itself (→ Section 7.1). When broadband or multicolour imaging is required, wavelength-dependent changes in the radial profile of the Bessel illumination can complicate further image processing and analysis (→ Section 7.2).

Holography was invented in 1948 [31], but has only come into widespread use with the advent of lasers in the 1960s. It captures both the amplitude and phase of the light that is reflected or scattered by the object, by superimposing it with a reproducible reference wave and recording the resulting interference pattern [32]. The development of digital imaging sensors and computers enabled **digital holography** (DH) [33, 34], with applications ranging from art to science and security.

Ferraro et al. have suggested using the capability of DH to capture amplitude and phase to extend the depth of focus in microscopy [35]. A major advantage over scanning techniques is the reduced acquisition time. The developments of swept source laser technologies [36] and high-speed area cameras have opened up the possibility of combining OCT with DH, to a method that Hillmann et al. have called **holoscopy** [37]. It is based on the theoretical framework by E. Wolf on three-dimensional structure determination from holographic data [38] and the angular spectrum representation of electromagnetic waves [39]. Many low-coherence holograms are recorded at different wavelengths. Holographic reconstruction allows for virtual focusing of the reconstructed wave field (→ Chapter 8).

About this Thesis

The work presented in this thesis has been carried out in the Biomedical Imaging group of Prof. Dr. Rainer Heintzmann at the Leibniz Institute of Photonic Technology in Jena between 2011 and 2015. It focuses on the application of state-of-the-art fluorescence microscopy and image processing to advance biological research in and the development of an image acquisition and reconstruction system for holoscopic imaging. The thesis consists of three parts and an appendix.

Part I – Introduction and Methods gives a brief introduction to a selection of optical concepts and establishes the mathematical notation which will be used throughout the thesis. Its purpose is a quick recapitulation of the Optics background that will be required for parts II and III. Furthermore, it provides an introduction to the methods used in this thesis which include structured illumination microscopy (SIM), optical coherence tomography, Bessel beam generation, and holoscopy.

Part II focuses on fluorescence microscopy and quantitative image analysis. The results of two interdisciplinary research collaborations are presented and discussed.

Part III explores options for extended focus imaging in optical coherence microscopy. In Chapter 7, a method for Bessel beam engineering is proposed and the applicability of an image inversion interferometer is investigated. Chapter 8 covers the development of a holoscopic imaging system based on a frequency-tuning light source and a fast camera. In Chapter 9, an algorithm for computational image reconstruction is presented and further possibilities and challenges are discussed.

2

Theoretical Background

The behaviour of light may be described by the wave-particle dualism model. It exhibits both, properties of a propagating transverse electromagnetic (EM) wave and of massless particles which are called *photons*. For most concepts and experiments presented in this thesis, the EM wave model is more appropriate.
The following chapter establishes the most important physical and mathematical concepts which constitute the theoretical framework of this thesis. Readers not familiar with optical theory can find a more detailed treatment in [40]. Readers not familiar with Fourier optics may refer to [41].

2.1. Electromagnetic Waves

Light propagation can be described by the *wave equation*, a partial differential equation derived from the *Maxwell equations* [42]:

$$\left(\nabla^2 - \frac{n^2}{c^2}\frac{\partial^2}{\partial t^2}\right)\mathbf{E}(\mathbf{r},t) = 0, \tag{2.1}$$

where $c = 1/\sqrt{\epsilon_0\mu_0}$ is the speed of light. In vacuum it is: $c_0 = 2.9979 \times 10^8 \frac{m}{s}$. The electric field vector $\mathbf{E}$ can oscillate in any direction perpendicular to the direction of propagation. If the wave oscillates only in a single plane, it is *linearly polarized* and it suffices to consider the scalar wave equation

$$\nabla^2 E(r,t) - \frac{n^2}{c^2}\frac{\partial^2}{\partial t^2}(r,t) = 0.$$

In the strict sense, it applies only to homogeneous media, but it can also be applied approximately to locally homogeneous media (whose refractive index $n(\mathbf{r})$ varies slowly with distances of the order of a wavelength).

2.1.1. Monochromatic Waves

Plane Waves

One solution to the above equation is a plane, monochromatic wave with a harmonic time dependence and *angular frequency* ω

$$\mathbf{E}(\mathbf{r},t) = \mathbf{E_0}\cos(\mathbf{k}\cdot\mathbf{r} - \omega t) \tag{2.2}$$

or in complex notation

$$\mathbf{E}(\mathbf{r},t) = \mathbf{A}e^{\mathrm{i}(\mathbf{k}\cdot\mathbf{r}-\omega t)} = \mathbf{A}e^{\mathrm{i}\mathbf{k}\cdot\mathbf{r}}e^{-\mathrm{i}\omega t}$$

with *wave vector* $\mathbf{k}$ whose magnitude is the *wave number* $k = |\mathbf{k}| = \omega/c$ and *amplitude* A. The wave number is related to the spatial frequency $\mathfrak{K}$ as

$$\mathfrak{K} = \frac{k}{2\pi} = \frac{1}{\lambda}.$$

The term $\varphi = \mathbf{k}\cdot\mathbf{r} - \omega t$ is the *phase* of the wave and any plane normal to the direction of propagation satisfying $kr_\perp - \omega t = \text{const.}$ is called a *wavefront*. Consecutive planes are separated by the *wavelength* $\lambda = 2\pi/k$. An idealized plane wave has a constant *irradiance* $I(\mathbf{r}) \sim |A|^2$.

Unless stated otherwise, the z-direction will be taken along the direction of propagation throughout this thesis. This simplifies Eq. 2.2 to

$$\mathbf{E}(z,t) = \mathbf{E_0}\cos(kz - \omega t).$$

Spherical Waves

A spherical wave originating at position $\mathbf{r}_0$ is described by

$$\mathbf{E}(\mathbf{r}) = \frac{\mathbf{A}}{|\mathbf{r}-\mathbf{r}_0|}e^{\mathrm{i}(k|\mathbf{r}-\mathbf{r}_0|-\omega t)}.$$

Remarks

In theory, monochromatic light has only a single frequency. In practice however, light sources are not monochromatic but operate in a small range of frequencies known as the *spectral linewidth*. Filtered light, diffraction grating separated light and laser light are all commonly referred to as monochromatic.
Frequencies of optical waves lie in the range of $3 \cdot 10^{11}$ to $3 \cdot 10^{16}$ Hz. Visible to the human eye are only wavelengths from approximately 380 to 750 nm (or frequencies from 7.9 to $4 \cdot 10^{14}$ Hz), depending on the sensitivity of photoreceptor cells in the individual's retina.
In this thesis, optical waves in the ultraviolet and visible range are employed for fluorescence excitation (Chapter 4) and the demonstration of a Bessel illumination (Chapter 7) and near-infrared waves for holoscopic imaging (Chapter 9).

2.1.2. Polychromatic Light

Polychromatic waves contain radiation of more than one wavelength, but may be expanded to a superposition of monochromatic waves. For an arbitrary function $u(\mathbf{r},t)$ at a fixed position $\mathbf{r}$ this superposition of waves of different frequency, amplitude and phase is represented by the Fourier transform integrals

$$\begin{aligned} u(t) &= \int\limits_{-\infty}^{\infty} v(\nu)\, e^{\mathrm{i}2\pi\nu t}\, \mathrm{d}\nu \\ v(\nu) &= \int\limits_{-\infty}^{\infty} u(t)\, e^{-\mathrm{i}2\pi\nu t}\, \mathrm{d}t. \end{aligned}$$

2.2. Coherence

Temporal Coherence

Temporal coherence is the auto-correlation of a wave as a function of the time delay τ between any pair of times. The *temporal coherence function* $G(\tau)$ is defined as

$$G(\tau) = \langle E^*(t)\, E(t+\tau)\rangle = \lim_{T\to\infty} \frac{1}{2T} \int\limits_{T}^{-T} E^*(t)\, E(t+\tau)\, \mathrm{d}t.$$

For $\tau = 0$, this is equal to the irradiance I.

$$G(0) = \langle E^*(t)\, E(t)\rangle = I.$$

The *complex degree of temporal coherence* $g(\tau)$ is defined as

$$g(\tau) = \frac{G(\tau)}{G(0)} = \frac{\langle E^*(t)\, E(t+\tau)\rangle}{\langle E^*(t)\, E(t)\rangle}, \quad g(\tau)\,\epsilon\,[0,1].$$

It is 1 for perfectly monochromatic light and 0 for completely incoherent light.

2.3. Interference

The wave equation is linear and the principle of superposition applies: If each wave $\mathbf{E}_i(\mathbf{r},t),\ i = 1,2,...,N$ is a solution of the wave equation (2.1), then

$$\sum_{i}^{N} \beta_i \mathbf{E}_i(\mathbf{r},t)$$

also represents a solution.

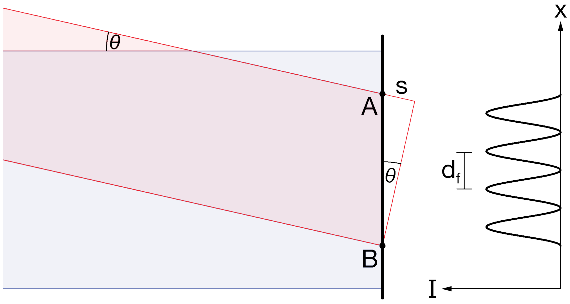

Figure 2.1.: **Interference of two plane waves** under an angle θ

2.3.1. Two-Beam Interference

The coherence function can be used to describe the interference of two partially coherent waves $E_1(t)$, $E_2(t)$ at time delay τ

$$\begin{aligned} I_{1,2}(\tau) &= \left\langle \left| E_1(t) + E_2(t+\tau) \right|^2 \right\rangle && (2.3)\\ &= \left\langle \left| E_1 \right|^2 \right\rangle + \left\langle \left| E_2 \right|^2 \right\rangle + \left\langle E_1^* E_2 \right\rangle + \left\langle E_1 E_2^* \right\rangle \\ &= I_1 + I_2 + 2\Re \left\{ \left\langle E_1^*(t) \, E_2(t+\tau) \right\rangle \right\} \\ &= I_1 + I_2 + 2\Re \left\{ G_{1,2}(\tau) \right\} \\ &= I_1 + I_2 + \Upsilon_{1,2}(\tau) \, . && (2.4) \end{aligned}$$

The *interferogram* $\Upsilon_{1,2}(\tau)$ equals twice the real part of the *coherence function* $G_{1,2}$ of the two beams

$$\Upsilon_{1,2}(\tau) = 2\sqrt{I_1 I_2} \cdot g(\tau) \cdot \cos(\varphi_0 - \Delta\varphi_{1,2}) \, ,$$

with phase difference $\Delta\varphi_{1,2} = 2\pi\bar{\nu}\tau$ and constant phase term φ_0.

Interference of Plane Waves

For two monochromatic waves with equal frequencies and the same polarization, it is sufficient to consider scalar theory

$$A_1(\mathbf{r}) = a_1 \, e^{\mathrm{i}\varphi_1(\mathbf{r})} \quad \text{and} \quad A_2(\mathbf{r}) = a_2 \, e^{\mathrm{i}\varphi_2(\mathbf{r})} \, .$$

For waves with different polarization directions it can also be applied if the different components of the electric field vector are considered separately. The resulting amplitude is the sum $A = A_1 + A_2$ and the intensity can be calculated as

$$I = I_1 + I_2 + 2\sqrt{I_1 I_2} \cos \Delta\varphi_{1,2} \, . \tag{2.5}$$

The separation d_f between the resulting interference fringes (the distance between two interference maxima) on a screen or camera depends on their incidence angles θ as shown in Fig. 2.1). *Constructive interference* appears for $\Delta\varphi = 2n\pi$ and *destructive intereference* appears for $\Delta\varphi = (2n+1)\pi$ for $n = 0, 1, 2, ...$ (n is the *intereference order*).

If we assume that both waves are in phase at point A, the phase difference $\Delta\varphi$ at point B is given by

$$\Delta\varphi = \frac{2\pi}{\lambda} \cdot s = \frac{2\pi}{\lambda} \cdot x \cdot \sin\theta = \Delta\varphi(x).$$

The interference finge separation is thus

$$d_f(\theta) = \frac{\lambda}{\sin\theta}\,. \tag{2.6}$$

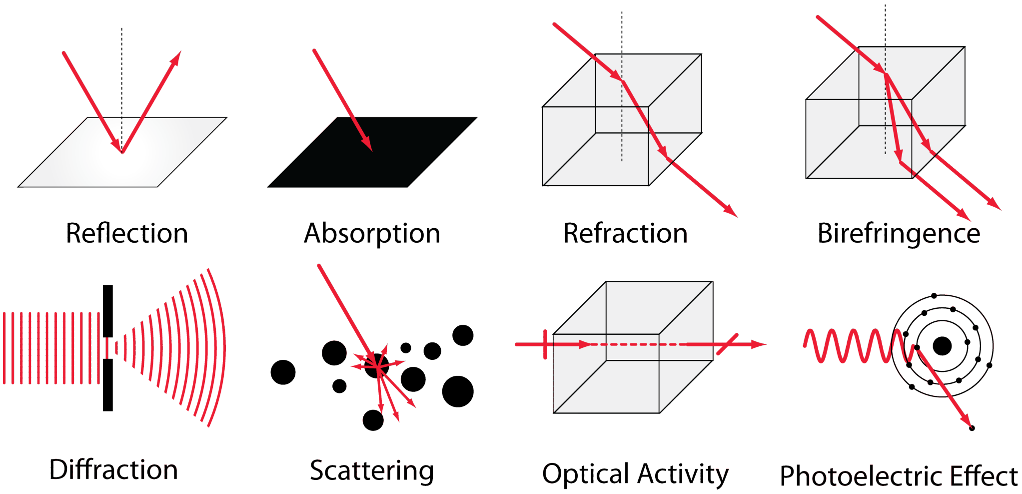
Reflection
Absorption
Refraction
Birefringence
Diffraction
Scattering
Optical Activity
Photoelectric Effect

Figure 2.2.: **Overview of light-matter-interactions**

2.4. Light-Matter Interactions

Light-matter interactions include *reflection*, *refraction*, *absorption*, *diffraction*, *birefringence* and *optical rotation*, different ways of *scattering*, and the *photoelectric effect* (see Fig. 2.2).
Diffraction and scattering are particularly important for this thesis and briefly introduced in sections 2.5 and 2.7 below.

2.4.1. Light Propagation in Matter

In free space, light travels at speed c_0. A homogenous transparent medium (i.e. glass or water) is characterized by its *refractive index* n (typically≥ 1). In such a medium, the phase velocity of light is slower than in vacuum and the wavelength is shorter, while the frequency typically remains constant.

$$v_{ph}(n) = c/n \qquad\qquad \lambda(n) = \lambda_0/n.$$

2.5. Diffraction and Propagation

Diffraction occurs whenever a light wave encounters an obstacle or a slit and is most pronounced when the diffracting object is comparable in size to its wavelength. The resulting intensity distribution at some distance in free space is called the *diffraction pattern*. Diffraction is essential for holographic imaging. Both diffraction and propagation can be described by a similar same mathematical formalism, the *angular spectrum* approach.

2.5.1. Huygens' Principle

Every point of the wave front can be considered as a virtual point emitter that is the source of secondary waves. These *wavelets* form the wavefield at any other position by coherent superposition [43]. With the *Huygens' principle* the phenomenon of diffraction can be explained as an effect of interference. It predicts nicely the diffraction pattern formed when a plane wave encounters a grating (see Fig. 2.3). The angle α of the diffraction orders N depends on the *grating distance* D and wavelength λ

$$D\ \sin\alpha = N\ \lambda.$$

Diffraction gratings are used on several occasions throughout this thesis. In Structured Illumination Microscopy, which is introduced in Section 3.2.2), a diffraction grating creates a Moiré effect to enhance resolution. For the generation of the Bessel beam in Chapter 7 a spatial light modulator with a pixel grid is used.

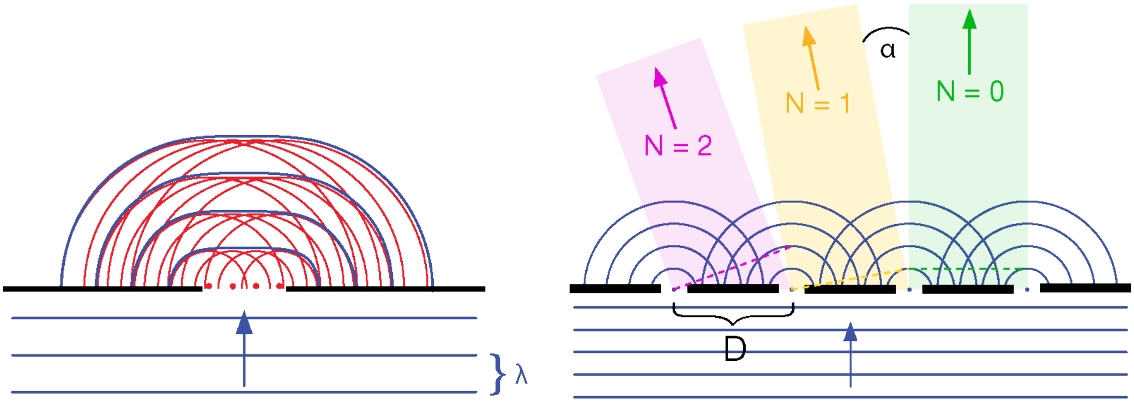

Figure 2.3.: **Huygen's principle** considers every point on a wavefront as the source of spherical wavelets. The diffraction pattern results from the interference of secondary wavelets. *Left:* A plane wave incident on a small slit. *Right:* An incident wave incident on a grating and resulting diffraction orders.

2.5.2. Angular Spectrum

Any arbitrary field can be decomposed into a series of plane (and evanescent) waves with different directions and amplitudes which is called the *angular spectrum representation* and a powerful method to describe light propagation and diffraction. If the complex field distribution $\mathbf{E}(x_0, y_0, z_0 = 0)$ across a plane is known (see Fig.

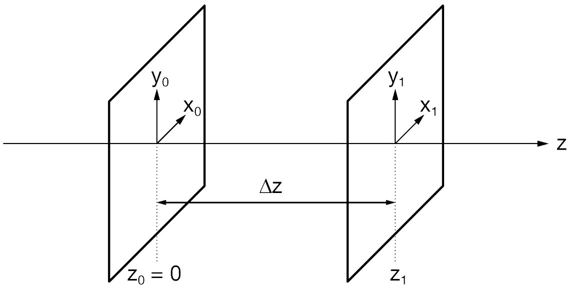

Figure 2.4.: **Coordinate system for angular spectrum propagation.** If the field at z_0 is known, the field at z_1 can be calculated with a propagator.

2.4), the field $\mathbf{E}(x_1, y_1, z_1)$ across any other parallel plane can be calculated from the individual plane wave contributions. The Fourier spectrum at z_0 is given by the 2D FT

$$\tilde{\mathbf{E}}(k_x, k_y, z_0) = \iint_{-\infty}^{\infty} \mathbf{E}(x_0, y_0, z_0)\; e^{-\mathrm{i}2\pi(k_x x_0 + k_y y_0)}\; \mathrm{d}x_0 \mathrm{d}y_0.$$

As the angular spectrum $\tilde{\mathbf{E}}$ along the z-axis, a phase factor has to be multiplied to the spectrum

$$\tilde{\mathbf{E}}(k_x, k_y, z_1) = \tilde{\mathbf{E}}(k_x, k_y, z_0) \cdot e^{\pm \mathrm{i} k_z \Delta z}$$

with $k_z = \sqrt{k^2 - k_x^2 - k_y^2}$ and $\Delta z = z_1 - z_0$. The phase factor $\tilde{p}(k_x, k_y, \Delta z) = e^{\pm \mathrm{i} k_z \Delta z}$ is called the *propagator*. Its inverse Fourier transform yields the real-space propagator $p(x, y, z)$

$$\begin{aligned} p(x, y, \Delta z) &= \mathcal{F}^{-1}\{\tilde{p}(k_x, k_y, \Delta z)\} \\ &= \iint_{-\infty}^{\infty} e^{\pm \mathrm{i}2\pi(k_x x + k_y y \pm k_z \Delta z)} \mathrm{d}k_x \mathrm{d}k_y. \end{aligned} \tag{2.7}$$

The ± sign denotes forward and backward propagation. In real space, the field at $z_1 = z_0 + \Delta z$ is then given by the convolution

$$\mathbf{E}(x_1, y_1, z_0 + \Delta z) = \mathbf{E}(x_0, y_0, z_0) \otimes p(x, y, \Delta z).$$

In terms of diffraction it can be interpreted as a modified Huygens-Fresnel principle which operates with secondary plane waves rather than with secondary spherical waves [39]. The plane wave decomposition of the angular spectrum approach is essential for the holographic reconstruction in Chapter 9. A more extensive treatment may be found in [41, 44].

2.6. Absorption

A collimated beam that passes through tissue is gradually losing intensity, mainly due to absorption and scattering. This attenuation is wavelength-dependent and different for each tissue component *tc*.

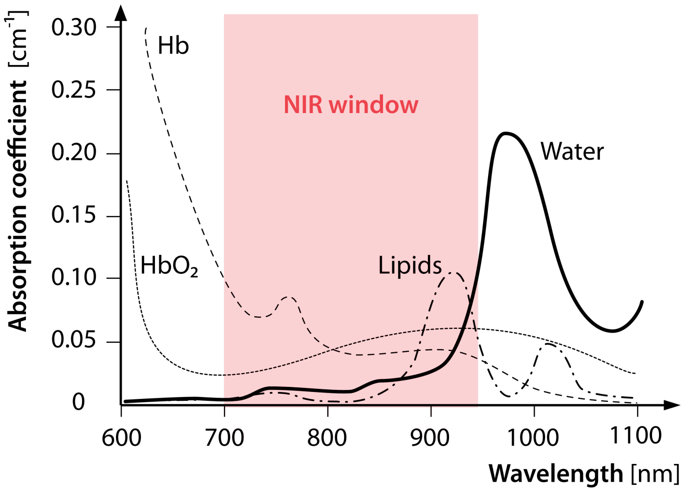

Figure 2.5.: **The NIR window** in the absorption spectra of typical human tissue components such as water, lipids, oxygenated and desoxygenated haemoglobin (HbO_2, Hb) [45].

The absorption of light of a certain wavelength by a material is described by the *molar extinction coefficient* ε_λ according to the Lambert-Beer-law [46]:

$$\lg \frac{I_0}{I_1} = \varepsilon_\lambda \; c \; d$$

with transmitted intensity I_1, incident intensity I_0, concentration c and path length d.

The molar extinction coefficient is related to the *absorption coefficient* μ_a via the molar concentration C. μ_a is defined as the probability of photon absorption per unit path length.[47]

$$\mu_a(\lambda) = \ln(10) \; \varepsilon_{tc}(\lambda_1) \; C_{tc}$$

The *attenuation coefficient* μ of a volume is the sum of its absorption and scattering coefficients

$$\mu = \mu_\mathrm{a} + \mu_\mathrm{s}.$$

Figure 2.5 shows the absorption coefficients for typical human tissue components such as water melanin and haemoglobin over the visible and near infrared (NIR) range. Light has its maximum penetration depth between 650 and 1350 nm. This range is called the *NIR window* and is limited by the absorption of blood at shorter wavelengths and water at longer wavelengths. Within this range scattering is the most dominant light-tissue interaction.

2.7. Optical Scattering

One characteristic of a medium is its refractive index $n(\mathbf{r})$. Inhomogeneities of n scatter the incident field. The relative amplitudes of the scattered field compared to the incident field are described by the *scattering potential* $\eta(\mathbf{r})$. It is related to the (complex) refractive index distribution $n(\mathbf{r})$ as

$$\eta(\mathbf{r}) = k^2 \left[n^2(\mathbf{r}) - 1\right].$$

2.7.1. Born Approximation

Throughout this thesis, scattering is treated within the first order Born approximation. It assumes that the field inside the scattering volume is constant and equal to the incident field. Multiple scattering is neglected. This is usually fulfilled well, if there are only sparse and weak scatterers in a medium. A detailed treatment of the Born series and the inhomogeneous Helmholtz equation can be found in [48]. For an incident monochromatic plane wave

$$\mathbf{E}_i(\mathbf{r}) = \mathbf{A}_i \, e^{\mathrm{i}\mathbf{k}\cdot\mathbf{r}},$$

with amplitude distribution $\mathbf{A}_i$, the scattered field $\mathbf{E}_s(\mathbf{r})$ in the first order Born approximation is given by [38, 48]

$$\mathbf{E}_s(\mathbf{r}) = \int \mathbf{A}_i \frac{e^{\mathrm{i}\mathbf{k}|\mathbf{r}-\mathbf{r}'|}}{|\mathbf{r}-\mathbf{r}'|} \, e^{i\mathbf{k}\cdot\mathbf{r}'} \, \eta(\mathbf{r}') \, \mathrm{d}^3\mathbf{r}', \tag{2.8}$$

2.7.2. Types of Scattering

Scattering phenomena can be classified into three general types. If the scattered light is of the same frequency as the incident light, the scattering is *elastic*. Examples are Rayleigh and Mie scattering. If the emitted frequency is different than the incident radiation, as in Raman scattering or fluorescence, the scattering is *inelastic*. This wavelength shift can utilized to separate the Raman or fluorescent signal from elastically scattered light. A third type, *quasi-elastic scattering*, contains frequency shifts of the scattered light that are due to other effects, e.g. the Doppler effect.

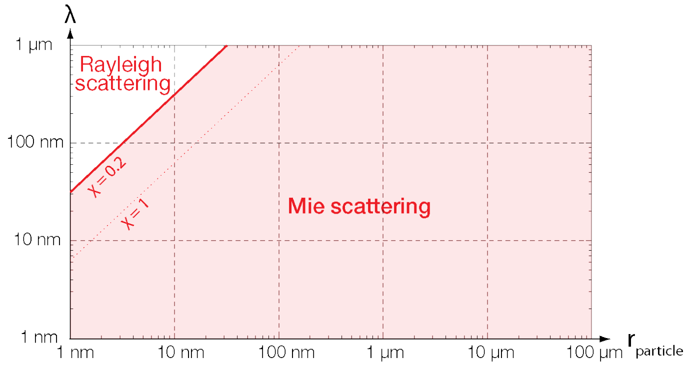

Figure 2.6.: **Scattering regimes** of Mie and Rayleigh scattering.

Scattering Regimes

If scattering is primarily caused by scattering particles which can be approximated as spheres of radius r, a rough classification of different scattering regimes can be made based on a size parameter

$$\zeta := \frac{2\pi r}{\lambda}.$$

Rayleigh scattering is predominant for $\zeta \ll 1$, in the $\zeta \approx 1$ range *Mie scattering* is most relevant and for $\zeta \gg 1$ *geometric scattering* is to be considered. The dominant scattering regimes depending on particle radius and wavelength are plotted in Fig. 2.6. It can be seen that for particles in the range of 0.1 μm to 10 μm and wavelengths between 500 nm and 1 μm, Mie scattering is predominant.

2.7.3. Ewald's Sphere

The experimental access to the spatial frequency range by backscattering experiments is intrinsically limited. For each incident wave vector $\mathbf{k}_i$, all possible scattering vectors $\mathbf{K}$ (forward and backward) describe a spherical shell in Fourier space, the *Ewald sphere* [49]

$$\mathbf{K} = \mathbf{k}_s - \mathbf{k}_i$$

with $|\mathbf{k}_s| = |\mathbf{k}_i| = k_0$ It is shown in Fig. 2.7. For a given $\mathbf{k}_i$, the highest possible $\mathbf{K}$ obtainable in backscattering geometry is

$$\mathbf{K}_{max} = 2\mathbf{k}_i.$$

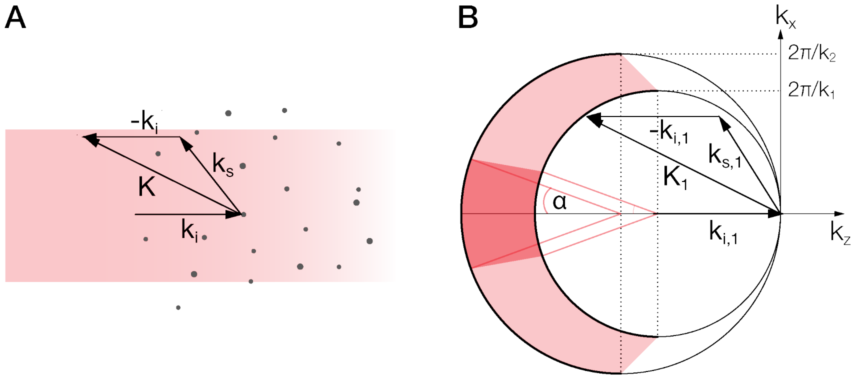

Figure 2.7.: **Backscattering geometry**. *A:* Incident wave $\mathbf{k}_i$, scattered wave $\mathbf{k}_s$, scattering vector $\mathbf{K}$. *B:* The arrowheads of all possible $\mathbf{K}$ describe *Ewald spheres* in Fourier space, shown here for wavelength range $[\lambda_1; \lambda_2]$ and backward scattering. The detectable backscattered waves are limited by the numerical aperture of the detection optics (dark shaded area)

2.8. Image Formation

Imaging systems are generally linear systems in which the superposition principle holds. The light distribution in the detection plane of an imaging system can be described as a superposition of plane waves with different amplitude and angle. For each wavelength, the k-vectors of these plane waves in Fourier space also lie on an Ewald's sphere (see Fig. 2.9) where the k-vectors correspond to all possible propagation angles of the plane waves.

2.8.1. 4-f Imaging Systems

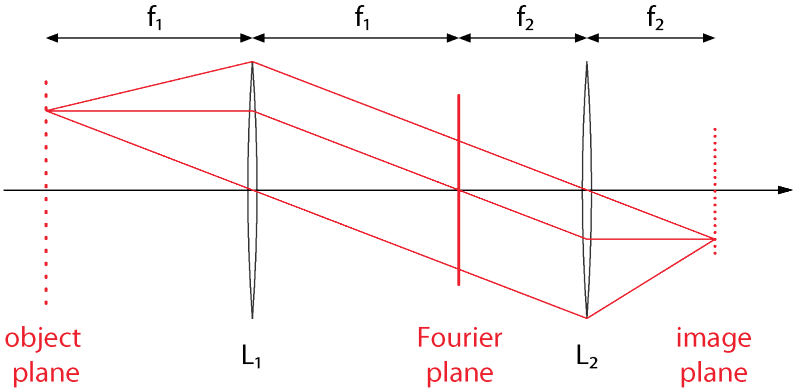

Figure 2.8.: **A 4-f imaging system** performs a Fourier transform of the object followed by an inverse Fourier transform. The coordinate system in the image plane is inverted.

A simple 4-f imaging system, as shown in Fig. 2.8, consists of an *object plane*, a (thin) lens with focal length f_1, a *Fourier plane*, a second lens with focal length f_2, and finally an *image plane*. Wave propagation in such a system can be conveniently described by two Fourier transforms: A 2D Fourier transform from the object plane to the Fourier plane and another 2D Fourier transform from the Fourier plane to the image plane. Each point in the Fourier plane corresponds to a particular spatial frequency component of the object. Object and image plane (and all intermediate image planes for more complex systems) are sometimes also referred to as *conjugate planes*. A few Fourier transform pairs which are relevant for this thesis are summarized on page 99 in the Appendix A.1.

If two lenses of different focal lengths are used, the image will be magnified compared to the object. The *magnification* is

$$M = -\frac{f_2}{f_1}.$$

2.8.2. Point Spread Function

The performance of an optical imaging system such as a microscope is fundamentally limited by diffraction and the loss of light during the imaging process. A point in the sample (i.e. a point source emitting light in all spatial directions) will not be resolved as a point in the image but as a spot of finite size called the *point spread function* (PSF).

Depending on the size and shape of the PSF, two points close to each other may no longer be distinguishable in the image. The PSF of an optical system can thus be used to determine its resolution capability (see 2.8.4).

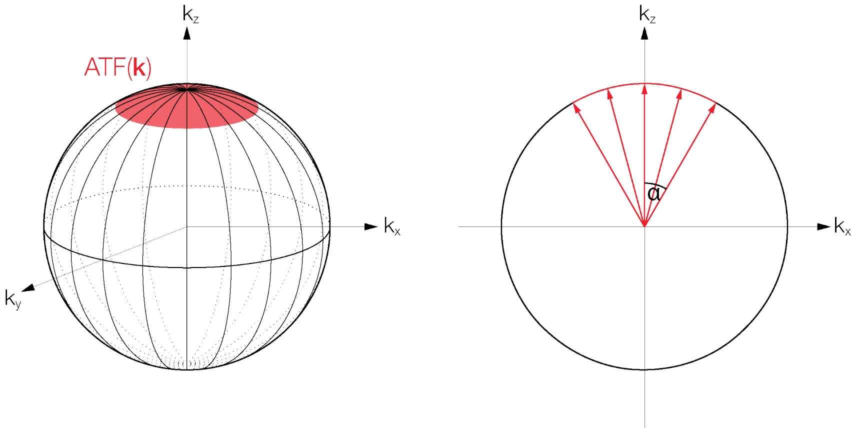

Figure 2.9.: **Ewald sphere, pupil function, and the amplitude transfer function**

2.8.3. Optical Transfer Function

The *optical transfer function* (OTF) is the Fourier transform of the PSF.

$$\mathrm{OTF}(\mathbf{k}) = \mathcal{F}\{\mathrm{PSF}(\mathbf{r})\}$$

It is a measure for how well different spatial frequency components are transmitted through the imaging system. The range of spatial frequencies that are transmitted is called the *support of the OTF* and fundamentally limits the resolution. Frequencies outside of this support are lost in the imaging process. However, several fluorescence microscopy techniques have been developed in order to circumvent this limit (see Section 3.2.2).

Pupil Function & Generalized Aperture

Expressed by its *numerical aperture* (NA), the objective of a microscope has a limited acceptance angle α at which it can capture light

$$\mathrm{NA} = n \ \sin\alpha. \tag{2.9}$$

As a consequence, only a limited range of optical frequencies can contribute to the image formation. This is described by the objective's *pupil function* that is illustrated in Fig. 2.9. Projecting the pupil function onto the Ewald sphere yields a spherical shell called the *McCutchen generalized aperture* [50] or three-dimensional *amplitude transfer function* ATF($\mathbf{k}$) of the system which is shown in Figure 2.9. Its inverse FT is the *amplitude point spread function* APSF($\mathbf{r}$) which corresponds to the amplitude distribution in the image plane of the optical system. The PSF can be calculated as the absolute square of the APSF

$$\mathrm{PSF}(\mathbf{r}) = |\mathrm{APSF}(\mathbf{r})|^2 = \mathrm{APSF}(\mathbf{r}) \ \mathrm{APSF}^*(\mathbf{r})$$

and the OTF is the auto-correlation of the ATF. The meaning of these functions will be further discussed in the context of coherent and incoherent imaging methods (Section 3.1).

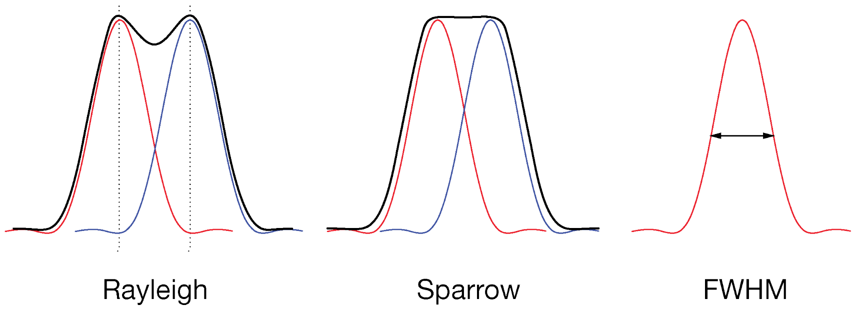

Figure 2.10.: **Resolution criteria.** The point spread function can be used to determine the resolution limit of an optical system.

2.8.4. Resolution

The resolution of an imaging system can be quantified in different ways as illustrated in Fig. 2.10. The *Sparrow criterion* [51] defines the resolution limit as the distance $d_{Sparrow}$ at which the a central dip in the sum of the PSFs of two points ceases to be visible. A lens under paraxial approximation yields:

$$d_{Sparrow} = 0.61\,\frac{\lambda}{\mathrm{NA}}.$$

According to the *Rayleigh criterion* [52] the minimum resolvable distance corresponds to the distance $d_{Rayleigh}$ between the PSFs' maximum and first minimum. Within the paraxial approximation this results in

$$d_{Rayleigh} = 0.475\,\frac{\lambda}{\mathrm{NA}}.$$

Another measure is the full width at half-maximum (FWHM) of the PSF

$$d_{FWHM} = 0.52\,\frac{\lambda}{\mathrm{NA}}.$$

Abbe's Diffraction Limit

Ernst Abbe showed experimentally that a diffraction grating image is resolved when the NA of the objective is large enough to capture the first diffraction order (see Figure 2.11) [53]. In terms of observable sample frequencies, the reciprocal grating distance has to lie within the support of the OTF. This also means that higher magnification does not equal the ability to see finer detail. The Abbe resolution limit for straight illumination is defined as:

$$d_{Abbe} = \frac{\lambda}{\mathrm{NA}}. \tag{2.10}$$

Throughout this thesis, Abbe's resolution limit will be the measure of lateral optical resolution.

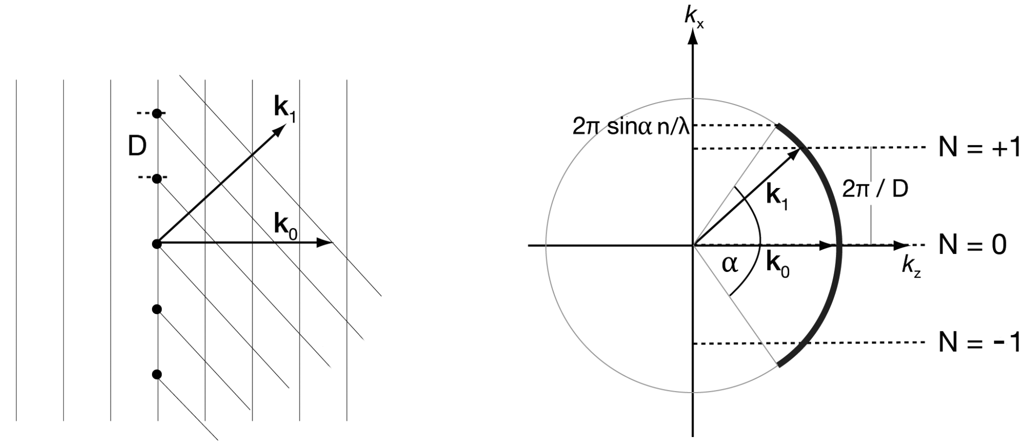

Figure 2.11.: **Abbe's diffraction limit.** *Right*: real space. *Left*: Fourier space. A similar figure has been previously provided to [54].

2.8.5. Spatial Filtering

An number of optical or computational filtering operations can be conveniently applied to the phase and amplitude of light in a Fourier plane (e.g. the back focal plane) of the imaging system. These operations essentially modify the spatial frequency spectrum of the image. Examples are low-pass and high-pass filtering for image enhancement. It is also possible to use a spatial filter in an image plane, for instance to a pinhole to "clean up" a laser output.

2.9. Gaussian Beams

Laser beams can usually be considered as Gaussian beams whose transverse intensity profiles are given by a Gaussian function. They are widely discussed in the optics literature and only a few relevant characteristics are mentioned here. Figure 2.12 shows a focused Gaussian beam.

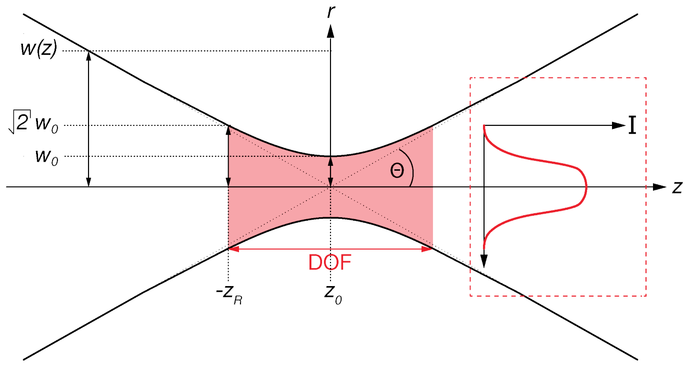

Figure 2.12.: **Focus of a Gaussian beam** with waist radius w_0 and a depth of field of $\pm z_R$

When focused by a lens to a plane $z_0 = 0$, the beam assumes a minimum width with *waist radius* w_0. It is inversely proportional to the beam's divergence angle Θ. At the radial distance w_0 from the optical axis, the beam intensity decreases by $1/e^2$.
Its intensity profile along the radial and axial directions is given by

$$I(r,z) = I_0 \left(\frac{w_0}{w(z)}\right)^2 e^{\left(\frac{-2r^2}{w(z)^2}\right)},$$

where I_0 is the intensity at the center of the beam waist.
The distance (along the propagation direction) from the beam's waist w_0 to where its cross section area is doubled is the *Rayleigh length* z_R. For a Gaussian beam in free space, the Rayleigh length is given by

$$z_R = \frac{\pi\ w_0^2}{\lambda}. \tag{2.11}$$

The axial distance $[z_0 - z_R, z_0 + z_R]$ is the *depth of field* (DOF).
At any position z, the beam's radius is

$$w(z) = w_0\sqrt{1 + (\frac{z}{z_R})^2}.$$

The 2D FT of a Gaussian is another Gaussian. Strictly speaking, since the Gaussian spectrum is infinite, a Gaussian beam does not exist in reality, but only approximations of it.

2.10. Fluorescence

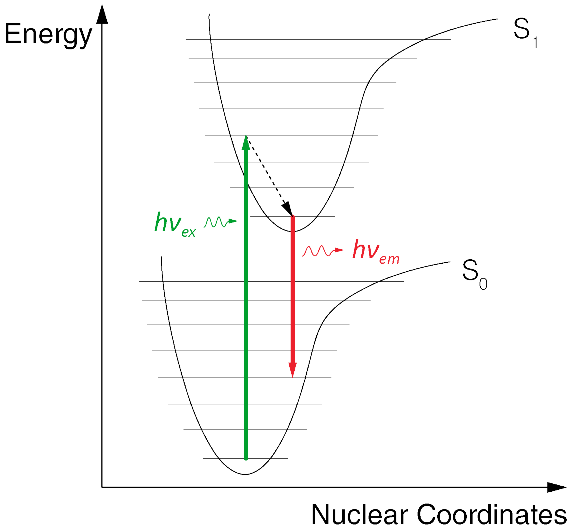

Figure 2.13.: **Franck-Condon principle and Jablonski diagram** explain why the light emitted by a fluorophore is red-shifted compared to the excitation light.

Fluorescent molecules can absorb a photon and re-emit another photon of longer wavelength. The absorbed photon excites the fluorophore from a ground electronic state S_0 to an excited state S_1 on a femtosecond time scale. The Franck-Condon principle states that nuclear motions can be neglected within the time scale of electronic transitions and vibrational levels that correspond to a minimal change in the nuclear coordinates are favored.

Each electronic state has several vibrational states. The molecule relaxes to the lowest vibrational level of the excited state by non-radiative transitions within picoseconds. Typical fluorescence lifetimes are the range of nanoseconds. When the fluorophore returns to an S_0 vibrational level, we observe the release of a photon whose energy corresponds to the difference between these two states (see Fig. 2.13). Another vibrational relaxation follows.

The difference between the absorption and emission wavelength depends on the fluorophore and its environment and is called the *Stokes shift*. In fluorescence microscopy this can be conveniently used to separate the illumination from the detection path by using dichroic filters.

3
Methods and Material

3.1. Coherent and Incoherent Imaging

The imaging techniques used in this thesis can be classified based on the way the studied sample emits light: While the light emitted from fluorescent samples can usually be considered as incoherent, interference-based techniques such as optical coherence tomography and holography rely on the coherence between scattered light from the sample and a reference wave. Both classes of imaging methods have characteristic advantages and drawbacks which are summarized in table 3.1.

In incoherent imaging, it is sufficient to superimpose intensities. Assuming a shift-invariant PSF and incoherent detection, an image consisting of point emitters is the sum of the individual PSF images of all emitters which can calculated as a convolution of the sample light distribution with the PSF. In fluorescence microscopy, the detected sample light $I_{\text{det}}(\mathbf{r})$ is the emission pattern $I_{\text{em}}(\mathbf{r})$, which is (ignoring saturation and effects) a product of the local fluorophore density $\varrho(\mathbf{r})$ and the illumination intensity $I_{\text{illu}}(\mathbf{r})$

$$\begin{aligned} I_{\text{det}}(\mathbf{r}) &= (\text{PSF} \otimes I_{\text{em}})(\mathbf{r}) \\ &= [\text{PSF} \otimes (\varrho \cdot I_{\text{illu}})](\mathbf{r}). \end{aligned} \tag{3.1}$$

For a uniform illumination, as in widefield fluorescence microscopy, $I_{\text{illu}}(\mathbf{r})$ is a constant I_0.

Incoherent imaging		**Coherent imaging**	
advantages	disadvantages	advantages	disadvantages
specific and multi-colour labelling	photo-toxicity	label-free	precise path alignment required
good contrast	bleaching	less photo-toxicity	phase information should be recorded
resolution beyond diffraction	low signal/noise	longer observation time possible	interference from unwanted reflections
		high signal/noise	

Table 3.1.: General advantages and disadvantages of incoherent and coherent imaging methods

In coherent imaging the amplitudes and phases of the complex wave fields have to be accounted for. Under the first Born approximation, a scattered light field $E_d(\mathbf{r})$ captured by a microscope objective can be described in the image plane as a convolution of electric field $E(\mathbf{r})$ (ignoring polarization) scattered by the sample $\eta(\mathbf{r})$ and the APSF [55]

$$E_d(\mathbf{r}) = [(E\ \eta) \otimes \mathrm{APSF}](\mathbf{r}). \tag{3.2}$$

3.2. High-Resolution Fluorescence Microscopy Methods

With highly specific fluorescent labelling with antibodies or genetically encoded fluorophores available, biological molecules of interest can be localized and monitored under the microscope with high specificity. Fluorescence microscopy enables three-dimensional multi-colour imaging in fixed or living cells. However, most subcellular or molecular structures are well below the Abbe limit (Eq. 2.10), which is approximately between 200–300 nm for visible light. A number of far-field super-resolution techniques have emerged that bypass this limit. Some of them, including *structured illumination microscopy*, are now established commercial techniques. Detailed overview articles may be found in [56, 57, 58].

3.2.1. Confocal Microscopy

Confocal microscopy is a widely used spot-scanning method for imaging fluorescence. By introducing a pinhole in the detection path, the out-of-focus light from planes other than the focal plane can be reduced and image contrast considerably improved. The confocal system used for Figure 4.1 on page 46 is a LSM 510 confocal microscope by Zeiss (Germany) with a 63× objective.

3.2.2. Structured Illumination Fluorescence Microscopy

Structured illumination microscopy (SIM)[60, 61] employs spatially modulated light to illuminate the sample. The illumination intensity I_{illu} in Eq. 3.1 becomes a two-dimensional harmonic pattern of spatial frequency $\mathfrak{K}$

$$I_{\mathrm{illu,SIM}}(\mathbf{r}) = I_0 \left(1 + \cos(\mathfrak{K}\mathbf{r} + \varphi_0)\right).$$

The $\mathrm{FT}_{\mathrm{2D}}$ of such an illumination pattern contains three Dirac's delta distribution $\delta\mathbf{k}$

$$\tilde{I}_{\mathrm{illu,SIM}}(\mathbf{k}) = I_0 \left(\delta(\mathbf{k}) + \frac{1}{2}\left[e^{\mathrm{i}\varphi_0}\delta(\mathbf{k}+\mathfrak{K}) + e^{-\mathrm{i}\varphi_0}\delta(\mathbf{k}-\mathfrak{K})\right]\right).$$

Thus the Fourier transform of Eq. 3.1 for a sinusoidal illumination becomes:

$$\begin{aligned}\tilde{I}_{\mathrm{det}}(\mathbf{k}) &= \left(\mathrm{OTF}\cdot\left[\tilde{\varrho}\otimes\tilde{I}_{\mathrm{illu,SIM}}\right]\right)(\mathbf{k})\\ &= I_0\ \mathrm{OTF}(\mathbf{k})\cdot\left[\tilde{\varrho}(\mathbf{k})\otimes\left(\delta(\mathbf{k}) + \frac{1}{2}\left[e^{\mathrm{i}\varphi_0}\delta(\mathbf{k}+\mathfrak{K}) + e^{-\mathrm{i}\varphi_0}\delta(\mathbf{k}-\mathfrak{K})\right]\right)\right].\end{aligned}$$

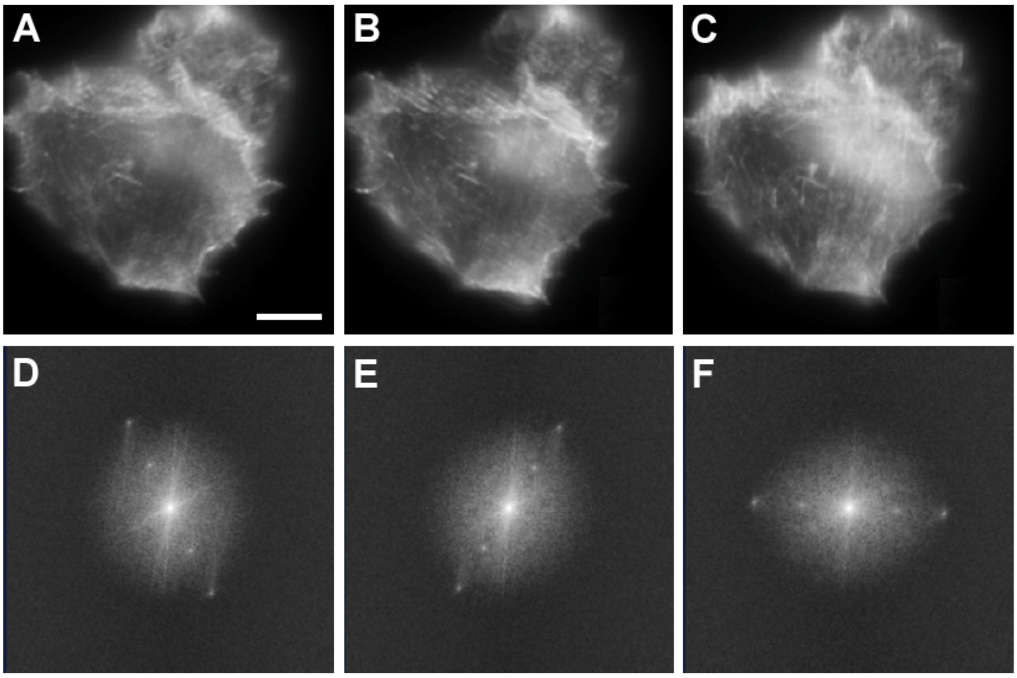

Figure 3.1.: **Image acquisition in structured illumination microscopy.** *A–C:* Raw images with three different grating directions. *D–F:* Corresponding FT_{2D}. This image is reproduced from [59]

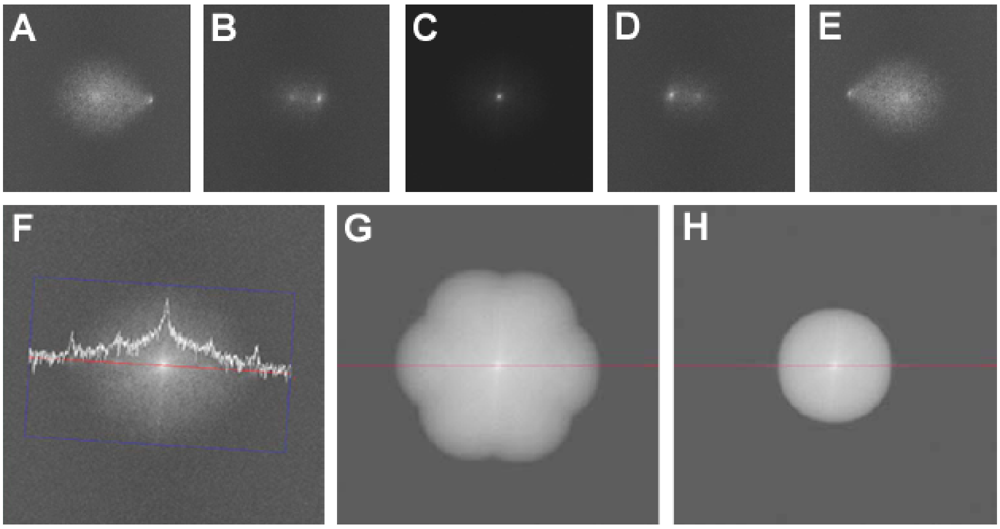

Figure 3.2.: **Image reconstruction in structured illumination microscopy.** *A–E:* separated peaks in Fourier space. *F:* Image information attached to one peak. *G:* The enhanced support region of the OFT after the separated peaks haven been shifted back and weighted. *H:* Comparison to the widefield OTF. This image is reproduced from [59]

The convolution with $\delta(\mathbf{k}\pm\mathfrak{K})$ shifts the zero position frequency to the delta peaks at $\mathbf{k}\pm\mathfrak{K}$. Hence structured illumination creates two additional peaks in Fourier space which contain the same sample information as the middle peak. Thereby otherwise unresolvable spatial frequency components are down-modulated and shifted into the support of the OTF. Acquisition of three or more images with different illumination grating positions and three to five different grating angles (9-20 images in total) allows to separate the information from the different peaks and computationally reconstruct one optically sectioned image with two-fold enhanced resolution [62]. The image recording and reconstruction process is illustrated in Figs. 3.1 and 3.2 for the example of 5 peaks (instead of 3) in Fourier space.

Setup

The SIM system used in chapters 4 and 5 is a commercial Elyra S (Zeiss, Germany) with a 63× NA 1.4 oil immersion objective. Available excitation light sources were 405 nm, 489 nm, 561 nm and 635 nm laser lines. For structured illumination, three different gratings were used, one 29 lines/mm grating and two 41.2 lines/mm gratings. Images were recorded with a CCD camera (Andor, USA), cooled to -25°C. Reconstructions were done with the commercial ZEN software installed on the system (based on [63]).

3.2.3. Stimulated Emission Depletion

In *stimulated emission depletion* microscopy (STED) [64, 65] is a spot-scanning method which used a doughnut-shaped depletion beam that de-excites fluorophores around its center and thereby narrows the effective detection PSF.

The STED system used in Chapter 4 is the commercial TCS-SP5 STED system from Leica (Germany). Excitation was carried out by a 635 nm pulsed diode laser and de-excitation by a MaiTai tunable fs laser at 750 nm. A resolution of 80 nm has been demonstrated with this system using bead samples.

3.2.4. Localization-based Methods

If the emissions of individual fluorophores can be separated temporally due to stochastic blinking (STORM [66]) or photoactivation (PALM [67], fPALM [68]), their position may be localized with greater accuracy than the system's optical resolution. Individual molecule positions are reconstructed by centroid fitting of their detected PSFs. STORM acquisition times are generally several minutes. For live cell imaging in Chapter 4, *Bayesian analysis of blinking and bleaching* (3B analysis) is used. It has been developed by Susan Cox et al [69]. Because 3B analysis can deal with significantly more dense datasets it needs less acquired raw images. Images of 50 nm resolution from data taken over 4 s have been demonstrated.

The microscopy setup for live-cell experiments is identical to the setup in [69]:
A wide-field Olympus IX81 is used with an oil immersion objective (Olympus 100×/NA 1.4). Illumination is provided by a Sutter Lambda LS xenon arc lamp

(Sutter Instruments, USA) coupled with a liquid light guide, with a Comar GFP-RFP filter set (Comar Optics, UK). Images are recorded using a Cascade II EM-CCD camera (Photometrics, USA).

3.2.5. Cell Culture and Immunocytochemistry

All podosome samples were prepared from the THP-1 human monocytic leukaemia cell line, which was obtained from the ATCC collection (LGC Standards, Middlesex, UK). This cell line was stimulated to differentiate into macrophages. Podosome formation was induced in these cells by seeding them on fibronectin coated cover glasses in the presence of the cytokine TGF-β-1 (1 ng/ml). Vinculin staining was conducted using VN-1 antivinculin mouse monoclonal antibody (Sigma, UK), conjugated to an anti-mouse secondary antibody. For Paxillin-staining anti-paxillin mouse monoclonal antibody (Sigma, UK) conjugated to an anti-mouse secondary antibody was used. The conjugates for SIM and confocal samples were Alexa488 and Alexa568 and for STED samples ATTO anti-mouse 647N (Sigma). For parallel labelling of vinculin and paxillin, a vinculin-GFP-lifeact construct was expressed. Actin was visualized by staining samples with Alexa488-, Alexa568- or Alexa633-conjugated phalloidin (Molecular probes). For talin experiments, THP-1 cells expressing an mCherry-tagged truncated talin construct were used (for transduction details see [69]).

3.2.6. Digital Image Analysis

The podosome core distance analysis is based on the automated podosome detection by Meddens et al [70] and was written in Matlab (The Mathworks, US) using the DIPimage toolbox (TU Delft, NL).

3.3. Optical Coherence Tomography

Optical coherence tomography (OCT) is an interferometric label-free biomedical imaging technique which utilizes light that is backscattered by refractive index variations in a sample. The backscattered signal is coherently amplified by interference with a strong reference wave. The limited coherence length of the light source creates a *coherence gate* to discrimate signal from different sample depths [71].

3.3.1. Classic Optical Coherence Tomography

The classic OCT setup is based on the Michelson interferometer with a light source of low time-coherence. Changing the path length of the reference arm provides a depth scan (also referred to as *A-scan*). The sample is scanned point-wise in the lateral direction. A series of adjacent depth scans (*B-scans*) forms the tomogram.

3.3.2. Fourier-Domain & Swept Source OCT

Instead of mechanically translating the reference mirror, it is also possible to encode the sample depth information spectrally in a single data acquisition. To this end,

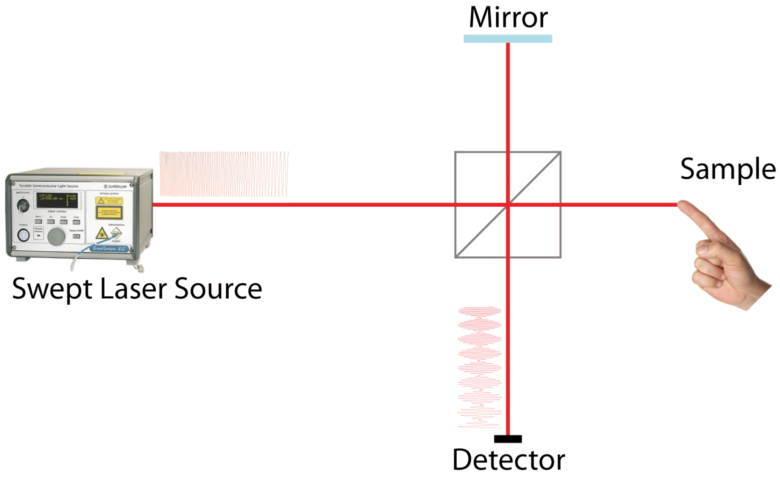

Figure 3.3.: Basic swept-source OCT setup. A tunable laser sweeps over a range of wavelength. The light is split by a beam splitter into sample and reference arm. The sample is scanned and backscattered light is superimposed with the reference light and measured.

either a light source which sweeps across a broad spectrum in time as in **Swept-Source OCT** (SS-OCT) or a spectrometer (or grating) to spatially disperse the spectrum across an array-type detector as in **Fourier-Domain OCT** (FD-OCT) is used. According to the theorem of diffraction tomography [72], the inverse Fourier transformation in the axial direction of the backscattered interference spectrum contains the sample's *scattering potential* $\eta(z)$.

3.3.3. The OCT Signal

The incident electric field is a function of the spectral envelope of the source field amplitude $A(k)$. For a narrow output spectral width Δk, it can be approximated as quasi-monochromatic with the central wavenumber $\bar{k}$. The light is split by a beamsplitter into the relative amplitudes A_R and A_S. The sample is illuminated by a plane wave propagating along the optical axis

$$E_0(z,k) = A_S\ A(|k|)\ e^{\mathrm{i}(kz)}.$$

According to Eq. 2.8 the scattered field is given by

$$E_S(k) = A(k) A_S \int \eta(z_s)\ \mathrm{d}z_s\ e^{\mathrm{i}k(z_0+2z)}$$

where z_0 denotes the plane of equal optical path length to the detector as the reference wave

$$E_R(k) = A(k) A_R\ e^{\mathrm{i}kz_0}.$$

The coherent wave fields interfere in the detector plane

$$I(k) = |E_S(k) + E_R(k)|^2 = \underbrace{E_S(k)E_S^*(k) + E_R(k)E_R^*(k)}_{\text{auto}-\text{correlations}} + \underbrace{2\Re(E_S(k)E_R^*(k))}_{\text{cross}-\text{correlation}}.$$

The first two terms are auto-correlation terms: $E_S E_S^*$ is caused by interference of the scattered light with itself and typically small. $E_R E_R^*$ creates a background offset which can be subtracted. The OCT signal is the cross-correlation term

$$\begin{aligned} I_{\mathrm{OCT}}(k) &= 2\ \Re\left\{E_S(k)E_R^*(k)\right\} \\ &= 2\ A^2(k)\Re\left\{A_R A_S \int \eta(z_s)\ \mathrm{d}z_s\ e^{\mathrm{i}2kz_s}\right\}. \end{aligned}$$

The scattering potential η can be obtained by an inverse Fourier transform [38, 72]

$$\begin{aligned} I(z) &= \mathcal{F}_z^{-1}\{I_{\mathrm{OCT}}(k)\} \\ &= 2A_R A_S\ \mathcal{F}_z^{-1}\left\{A^2(k)\left[\int \eta(z)\ e^{\mathrm{i}2kz}\ \mathrm{d}z + \int \eta(z)\ e^{-\mathrm{i}2kz}\ \mathrm{d}z\right]\right\} \\ &= A_R A_S\ \tilde{A}(k)\ \left[\eta\left(\frac{z}{2}\right) + \eta\left(-\frac{z}{2}\right)\right]. \end{aligned}$$

The two complex conjugate terms create an overlapping real and mirror image. This can be prevented by adjusting the reference path length such that all scattering structures lie on one side of the virtual reference plane in the sample. Then it can be assumed that $\eta(z) = 0$ for all $z < 0$

3.3.4. Resolution and Penetration Depth in OCT

One of the unique properties of OCT is that its axial and lateral resolution are effectively decoupled. The axial resolution is coherence-limited and depends on the *coherence length* l_c of the source spectrum (so-called "round-trip coherence length" since light travels twice through the sample). For a Gaussian spectrum it is given by: [72]:

$$l_c = \frac{2\ln 2}{\pi}\frac{\bar{\lambda}^2}{\Delta\lambda}. \tag{3.3}$$

The lateral resolution depends on the imaging optics and is governed by Abbe's diffraction limit as stated in Eq. 2.10 on page 19.
The size of the *coherent probe volume* in the sample is the product of the coherence length and the focal cross-section of the scanning beam.
A fundamental trade-off in OCT is that higher lateral resolution entails a smaller depth of field as illustrated in Fig. 3.4. High NA optics yield a good lateral resolution but only a very short DOF. As a result, most OCT systems work with very low NA (< 0.1) and achieve lateral resolutions in the range of 10-20 μm.

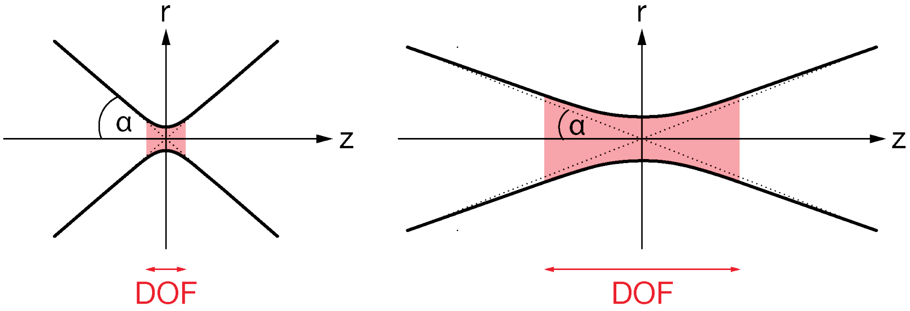

Figure 3.4.: **The spatial resolution versus depth of field dilemma in OCT**.

3.3.5. Full-field OCT

The acquistion of A-scans can be parallelized with an area camera which considerable improves acquisition speed. Full-field OCT has been demonstrated for time-domain [73] and Fourier-domain OCT [74]. With tunable lasers and high-speed cameras it has been applied *ex-vivo*[75] and *in-vivo* [76]. If high NA detection optics are used, the intrinsic advantage of fast axial acquisition is compromised and additional axial scanning becomes necessary.
For biomedical applications it would be desirable to enable the usage of a high-aperture objective and thus a lateral resolution in the micrometer range, comparable to other optical microscopy techniques.

3.4. Extended Focus

Different approaches have been followed to acquire deep volumes at high resolution. An obvious solution is to record a series of high-resolution tomograms with different focal positions. A general issue with these approaches is that the coherence gate and focal volume need to be matched. Schmitt et al. solved this issue with multiple sources and detectors combined with high-numerical-aperture optics [24].

Instead of Gaussian beams, **Bessel beams** can be used to illuminate the sample. They are also called "needle beams" in the literature and their properties and previous implementations are discussed in section 3.5 below.

Interferometric synthetic aperture microscopy (ISAM) achieves spatially invariant resolution and an improved depth of field with a numerical post-processing routine based on inverse scattering theory. The experimental setup uses phase-shifting interferometry (three measurements of the interference intensity distribution with different reference mirror delays) or assumes that the sample surface coincides with the focal plane of the objective and use only the half-space $z > 0$, such that conjugate and real image do not overlap. A method for inverse scattering in full-field OCT has so far only been demonstrated on simulated data [77, 78].

Ferraro et al. have suggested using the capability of **digital holography** to capture both amplitude and phase to extend the depth of focus in microscopy [35]. An advantage compared to scanning extended focus techniques is the full-field detection with an area camera which reduces acquisition time. Hillmann et al. have combined SS-OCT with digital holography (DH) to a method called **holoscopy** [37]. Many holograms are recorded with a low-coherence tunable laser. Holographic reconstruction allows for virtual focusing of the reconstructed wave field. Basic concepts of holography and their application to holoscopy are introduced in section 3.8 on pp. 35.

All methods mentioned above assume that the scattering is well modelled by the first-order Born approximation and neglect polarization effects.

3.5. Bessel Beams

Parts of this section have been previously published in [3]. Results are presented in Chapter 7.

Bessel beams were first presented by Durnin et al. [79]. They have the same intensity distribution (proportional to a zero-order Bessel function of the first kind) in every plane normal to the optical axis [80]

$$E\left(r,\phi,z\right)=E_0\cdot e^{ik_z z}\cdot J_0\left(k_r r\right).$$

The radially symmetric beam profile exhibits a central maximum surrounded by many concentric side lobes. Theoretically, these side lobes extend indefinitely and carry infinite amount of energy. Since real Bessel beam realizations are always aperture-limited, they are only approximations with an unchanged intensity profile over an extended, but finite region. For simplicity, we will refer to such zero order quasi-Bessel beam realizations as *Bessel beams* throughout this thesis.

The two-dimensional Fourier transform of a Bessel beam amplitude distribution yields a ring spectrum in k-space (see also Section A.2 in the Appendix). For an ideal Bessel, this spectrum only consists of an off-axis delta function at constant $|k|$. In an experimental realization the approximated Bessel beam is composed of a set of plane waves under a small range of angles and the interference maxima of their superposition form the Bessel beam. Hence, the interference at any position z_0 on the optical axis is independent of previous z and, unlike a Gaussian beam, the Bessel beam's central maximum can reappear behind a partial obstruction on the optical axis [25], which is interesting for Optical Tweezers [28] and Extended Focus microscopy [27].

3.5.1. Generating Bessel Beams

There are several established methods of generating Bessel beams. The refractive axicon [81, 82] generally uses light efficiently, but can be difficult to align and has little design flexibility. Furthermore, the tip of the axicon and other imperfections can cause strong axial intensity fluctuations of the Bessel beam that need to be

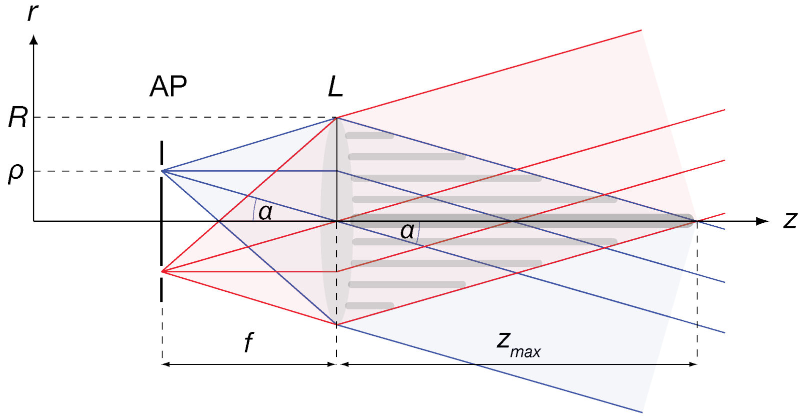

Figure 3.5.: **Geometry of the ring aperture and resulting Bessel beam**. Blue and red areas indicate diametrically opposed amplitude contributions. Horizontal grey bar indicate the resulting interference pattern. z optical axis; r radial coordinate; AP ring aperture; L lens; R lens radius; ρ annulus radius; f focal length; $\mathbf{z_{max}}$ axial Bessel beam extend; α angle.

appropriately compensated [83]. In analogy to the refractive axicon, a diffractive "axicon" can be implemented with a spatial light modulator (SLM) [84].

Ring illumination of the back focal plane of a lens (with the help of a ring-shaped aperture) will also generate a Bessel beam [29]. This method wastes a lot of the incoming light if simply a ring aperture is used to truncate any undesired light in the back focal plane (BFP), but the loss can be greatly reduced in combination with diffractive elements that fill the aperture, such as holograms [85] or SLMs [86].

Botcherby et al. [29] used a fixed binary phase-only grating in the plane conjugate to the image plane to produce the intermediate ring distribution and a narrow annular aperture in the Fourier plane to truncate undesired areas of the field and thereby suppress an undesired strong second ring close by. Instead of the conjugate plane, it is also possible to alter the phase distribution of the incoming light in the Fourier plane of the desired extended beam as demonstrated by Čižmár & Dholakia with an SLM as a hologram [30].

3.5.2. Geometry of the Bessel Beam

The radius of the angular spectrum $k_{r,0}$ defines the size of the central maximum and the distance to consecutive maxima. The axial beam extend z_{max} scales inversely with the radius of the ring ρ in k-space and proportionally to the radius of the imaging lens R and its focal length f, as can be seen from Fig. 3.5

$$\begin{aligned} \tan\alpha &= \frac{\rho}{f} = \frac{R}{z_{max}} \\ \Leftrightarrow z_{max} &= \frac{R}{\rho} \cdot f. \end{aligned}$$

with α: angle between plane wave propagation and optical axis.

As mentioned previously, a practical Bessel beam realization is made up of a range of angles α_i, the smallest of which (corresponding to the largest k_i in the spatial spectrum) determines z_{max}.

3.5.3. Bessel Beams for OCT

Bessel illumination with an axicon has been implemented by Ding et al. [87]. The axicon was placed directly in front of the sample instead of a microscope objective and 10 μm resolution of 6 mm depth were reported. This solution has the disadvantages that the backscattered light is also detected through the axicon. Beam scanning is not possible and the sample has to be scanned instead. Since the focal volume starts right behind the axicon tip, the working distance is very small.
Lasser and co-workers have decoupled the illumination and detection path and demonstrated how Bessel illumination (with an axicon) can be used for dark-field FD optical coherence microscopy [26, 27].
In Chapter 7, an alternative approach to Bessel illumination for OCT is proposed which is not based on an axicon, but a phase SLM. The material used for the experimental setup is listed below.

3.5.4. Setup

The setup is shown in Fig. 7.7A on page 72. Light from a green (532 nm) and red (635 nm) laser pointer (Coherent, Germany) is collimated and expanded such that the beam diameter fits the shorter side of an SLM display (X10468 by Hamamatsu, Japan). The parallel light is reflected from the SLM under a small angle and focussed through an achromatic doublet lens ($f = 50$ mm, AC254-050-A-ML, Thorlabs Inc, USA). A flip mirror allows to direct the light to a CCD webcam (Philips SPC900NC, Netherlands) to evaluate the intensity distribution in the ring plane. In the back focal plane of a second achromatic doublet lens ($f = 200$ mm, AC254-200-A-ML, Thorlabs Inc, USA), all undiffracted light is blocked by an opaque disk, such that only the ring illumination passes, which is then focussed onto a second CCD webcam mounted onto a motorized precision translation stage (Standa 8MT167-100, Lithuania) to evaluate the beam profile along the optical axis.

3.6. Iterative Fourier transform algorithm (IFTA)

IFTAs jump back and forth between two spaces connected by a Fourier transform to iteratively find a desired goal function. In each space, constraints are applied to the output function and at each iteration the error to the goal function is evaluated. These algorithms are commonly applied for phase retrieval problems in the design of diffractive optical elements. Originally published by Gerchberg & Saxton in the 1970's [88, 89], this group of algorithms has seen many improvements and adaptations since [90].

For chapter 7, a custom-written IFTA for phase pattern optimization was written in Matlab 7.7 (The MathWorks, USA) with the DIPimage 2.3 & DIPlib toolboxes (Quantitative Imaging Group, TU Delft, Netherlands).

3.7. Image Inversion Interferometry

Another interesting idea for extended focus imaging has been proposed by K. Wicker in his PhD thesis [62]: In an image inversion interferometer, "self-interference of a point source's coherent point spread function with its inverted copy leads to a reduction in the integrated signal for off-axis sources compared to sources on the inversion axis." This has been demonstrated to improve the lateral resolution in confocal laser scanning microscopy [91]. The detection PSF of such an interferometer is essentially independent of the axial position and could therefore be combined with Bessel beam illumination to reduce the high side-lobes and improve contrast and resolution.
In section 7.4 this idea will be further investigated. A custom-built image inversion interferometer (short:UZI) has been assembled for this purpose and is shown in figure 3.6.

Descanned light coming from a microscope is split into an U- and a Z-shaped and then recombined. The effect of the UZI can mathematically be modelled by a flip of the lateral coordinates in one arm, from $\mathbf{r} = (x, y, z)$ to $\hat{\mathbf{r}} = (-x, -y, z)$, followed by interference in an constructive ($g_+(\mathbf{r}_{x,y})$) and destructive ($g_-(\mathbf{r}_{x,y})$) channel. Acquisition by detectors corresponds to taking the absolute square and summing over the lateral coordinates

$$g_{+/-}(\mathbf{r}_{x,y}) = \int |A(\mathbf{r}) \pm A(\hat{\mathbf{r}})|^2 \mathrm{d}x \mathrm{d}y. \tag{3.4}$$

After image inversion, the channels are typically subtracted

$$\mathrm{PSF}_{\mathrm{UZI}}(\mathbf{r}_{x,y}) = g_+(\mathbf{r}_{x,y}) - g_-(\mathbf{r}_{x,y}). \tag{3.5}$$

The overall UZI PSF for any two interfering amplitude distributions A and B is given by

$$\begin{aligned} \mathrm{UZI}_{ges} &= \mathrm{UZI}_+ - \mathrm{UZI}_- && (3.6)\\ &= \left(|A|^2 + |B|^2 + 2\Re\left(AB^*\right)\right) - \left(|A|^2 + |B|^2 - 2\Re\left(AB^*\right)\right) \\ &= 4\Re\left(AB^*\right). && (3.7) \end{aligned}$$

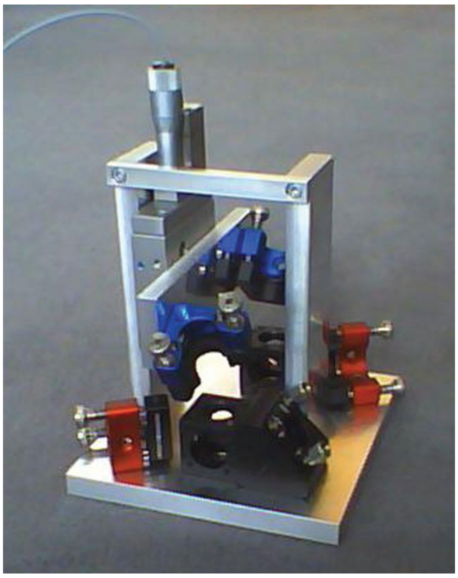

Figure 3.6.: **The custom-built image inversion interferometer** (shown without mirrors). Red and blue mounts belong to the different optical paths. Design by Dr. K. Wicker.

3.8. Holography

Holography is an interferometric imaging technique orginally introduced by Dennis Gabór for electron microscopy [31]. The first optical holograms of 3D object were recorded by Y. Denisyuk [92] and by E. Leith & J. Upatnieks [93] in 1962 after the development of the laser.

An object is illuminated with coherent light. To capture both the amplitude and phase of the light $E_O(x, y)$ that is reflected or scattered by the object, it is superimposed with a reproducible reference wave $E_R(x, y)$. The resulting interference pattern or *hologram* is imprinted on a recording medium

$$\begin{aligned} I(x,y) &= |E_O(x,y) + E_R(x,y)|^2 \\ &= |E_O|^2(x,y) + |E_R|^2(x,y) + E_O E_R^*(x,y) + E_O^* E_R(x,y). \end{aligned}$$

Early holograms were recorded on photo-plates of silver halide photographic emulsions which required an extended recording time. After development, the transmittance distribution $T(x, y)$ on the photo-plate linearly encodes the original intensity distribution

$$T(x,y) = \gamma \; I(x,y).$$

To develop the hologram, it is illuminated with a wave E'_R which is typically identical to the reference wave. The resulting diffraction pattern of the recorded hologram will produce an image and a twin-image of the object as shown in Figure 3.7.[1] For

---

[1] An unknown author once explained holography very nicely with music:
"Holography can be thought of as somewhat similar to sound recording, whereby a sound field created by vibrating matter like musical instruments or vocal cords, is encoded in such a way that it can be reproduced later, without the presence of the original vibrating matter."

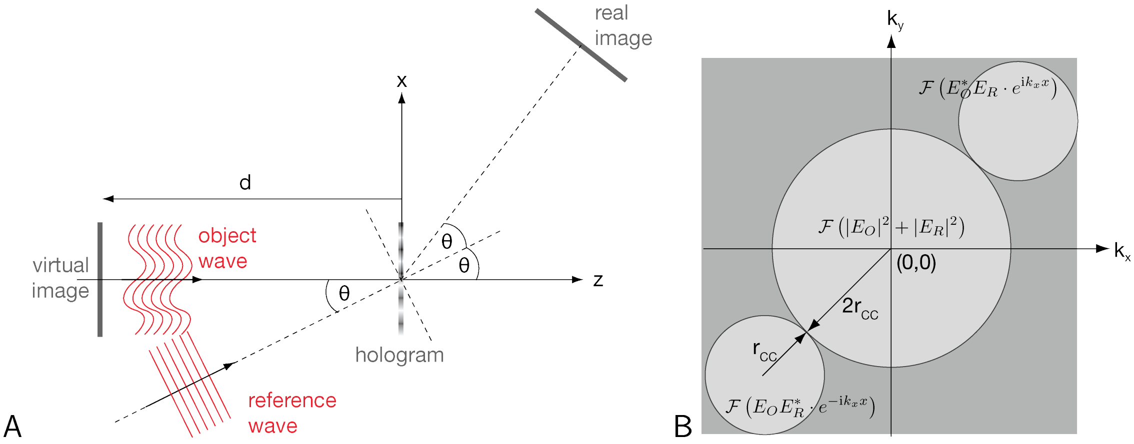

Figure 3.7.: **Recording principle of off-axis holography**. *A:* A small angle θ is introduced between the reference and object beams. *B:* This enables to reconstruct the information contained in the cross-correlation term using a single hologram acquisition.

simplicity the coordinate dependencies are dropped here.

$$\begin{aligned} E_H &= T \cdot E_R \\ &= \gamma |E_O|^2 E_R' + \gamma |E_R|^2 E_R' + \underbrace{\gamma E_O E_R^* E_R'}_{\substack{\text{real}\\ \text{image}}} + \underbrace{\gamma E_O^* E_R E_R'}_{\substack{\text{conjugate}\\ \text{image}}} \end{aligned} \tag{3.8}$$

3.8.1. Digital Holography

J. W. Goodman & R. W. Lawrence demonstrated 1967 that holograms can also be digitized and reconstructed numerically [33]. Instead of photo-plates, holograms can nowadays be recorded by digital imaging sensors. A large variety of applications and methods based on holography has developed. For a general overview, the reader may refer to [32].

According to the work of E. Wolf [38] & A. Fercher [94] it is not sufficient to record *one* hologram to image a three-dimensional volume. Instead, holograms under different illumination angles or at multiple wavelengths are required to obtain sufficient Fourier transform components of the sample's scattering potential. This is illustrated in Fig. 2.7B on page 16.

3.8.2. Off-Axis Holography

An established method in digital holography to separate the real and conjugate image is to introduce an angle θ between the optical axis of the reference beam and the camera normal, as shown in Fig. 3.7, such that the reference wave becomes

$$E_{R,off} = E_R \cdot e^{\mathrm{i}k_x x}.$$

The recorded intensity distribution on the camera then consists of the interference terms

$$\begin{aligned} I &= |E_O + \left(E_R \cdot e^{\mathrm{i}k_x x}\right)|^2 \\ &= |E_O|^2 + |E_R|^2 + E_O E_R^* \cdot e^{-\mathrm{i}k_x x} + E_O^* E_R \cdot e^{\mathrm{i}k_x x} \\ &= I_O + I_R + I_H \; e^{-\mathrm{i}k_x x} + I_{H^*} \; e^{\mathrm{i}k_x x}, \end{aligned}$$

where $I_H \; e^{-\mathrm{i}k_x x}$ and $I_{H^*} \; e^{\mathrm{i}k_x x}$ denote the the cross-correlation contributions. According to the Fourier shift theorem, the resulting additional phase term $e^{\mathrm{i}k_x x}$ with $k_x = k \cdot \sin\theta$ in real space introduces a lateral shift in Fourier space. (The z-component produces a constant phase shift $k_z = k \cdot \cos\theta$, which is ignored here.)

$$\mathcal{F}\{I_H(x,y)\}e^{-\mathrm{i}k_x \Delta x} = \mathcal{F}\{I_H(x + \Delta x, y)\} \tag{3.9}$$

Another consequence are finer interference fringes which need to be adequately sampled. In chapter 8 the implementation of such an holographic recording platform is presented. The material and parts used for it are listed below.

3.9. Holoscopy Platform

3.9.1. Parts

	Part	Manufacturer	Item	Specification
	Swept source	Superlum, Ireland	BroadSweeper BS-840-2 HP	790–880 nm; *see 3.9.2*
	Polarization-maintaining fibre	Thorlabs, USA	P3-780PM-FC-2	770–1100 nm
L1	Achromatic lens	Thorlabs	AC254-050-B-ML	$f = 50$ mm
PBS	Polarizing beam splitter cube	Thorlabs	CM1-PBS252	50:50, 620–1000 nm
M1, M2, M3	Mirrors	Thorlabs	PF10-03-P01	1", silver coated
	Mirror mounts	Fine Adjustment, Germany	13.00043.001	Earth series
FA	Field aperture	Thorlabs	SM1D12	
L2	Achromatic lens	Thorlabs	AC254-075-B-ML	$f = 75$ mm
BS	Non-polarizing beam splitter cube	Thorlabs	CM1-BS014	50:50; 700–1100 nm
OBJ	Objective			*see 3.9.4*
QWP	Quarter-wave plate	Thorlabs	WPQ10E-830	Polymer zero-order, 830 nm
XYZ	Translation stage (XY)	Thorlabs	XYFM1/M	
	Micrometer head (Z)	Mitutoyo, Japan	150-801ME	25 mm travel, 10 μm graduations
POL	Linear polarizer	Bolder Vision, USA	BVO IR	∅ 25.4 mm
CAM	Camera	IDT, USA	NX4-S2	*see 3.9.3*
	Camera angle mount	Thorlabs	AP180/M	tilted to 45°
USAF	Resolution target	Thorlabs	R3L3S1N	
	Infrared viewing card	Thorlabs	IRC3	

3.9.2. Light source

The tunable semiconductor laser in this setup is a Superlum BroadSweeper BS-840-2 with a spectral range of 790–880 nm. The sweep speed can be set between 100 and 100'000 nm/s. The output power of the light source is 3–4 mW.

The linewidth (instantaneous bandwidth) of the light source determines the (instantaneous) coherence length $l_{c,i}$, which is the range in which interferometric measurements can be obtained

$$\begin{aligned} l_{c,i} :=& c \cdot \tau_{c,i} = \frac{c}{\pi \Delta\nu_i} \\ \Delta\nu_i =& \frac{c \cdot \Delta\lambda_i}{\lambda^2} \\ \rightarrow l_{c,i} =& \frac{\lambda^2}{\pi \cdot \Delta\lambda_i}. \end{aligned}$$

It is shortest for $\lambda = 790$ nm. In the brighter mode (4 mW) the linewidth is 0.11 nm, thus

$$l_{c,i} = \frac{790 \text{ nm})^2}{\pi \cdot 0.11 \text{ nm}} \approx \mathbf{1.8} \text{ mm}.$$

The total wavelength tuning range $\Delta\lambda_t$ determines the axial resolution

$$\Delta z = \frac{2\ln(2)}{\pi} \cdot \frac{\lambda^2}{\Delta\lambda}. \tag{3.10}$$

For the BroadSweeper parameters the best achievable axial resolution is thus

$$\Delta z = \frac{2\ln(2)}{\pi} \cdot \frac{((880+790) \text{ nm}/2)^2}{880-790 \text{ nm}} \approx 0.44 \cdot \frac{835^2}{90} \text{ nm} \approx \mathbf{3.4}\ \mu\text{m}.$$

3.9.3. Camera

The camera is a IDT NX4-S2. Key specifications are listed below

Maximum resolution	1024 × 1024 pxl (= 1 MP)
Maximum frame rate @ 1 MP	2000 fps
Minimum exposure time	1 μs
Sensor size	13.9 x 13.9 mm^2
Pixel size	13.68 μm^2
Pixel depth (mono)	10 bit
Trigger	TTL
File format	proprietary RAW
Convertible to	TIF, BMP, JPG, PNG, AVI, MPG, TP2, MOV, MRF, MCF

3.9.4. Objectives

Different objectives were available for achromatic performance in the NIR range. The Olympus MPlan delivers a lateral resolution in the range of the axial resolution (given in 3.9.2). For even higher lateral resolution, the Zeiss EC EPIPLAN 20× 0.4 can be installed.

	M	NA	α	WD	f_{TL}	$\mathrm{f}_{\mathrm{Obj}}$	$\mathrm{d}_{\mathrm{min}}$	$\mathrm{R}_{\mathrm{BFP}}$
	×		°	[mm]	[mm]	[mm]	[μm]	[mm]
Zeiss EC EPIPLAN	20	0.4	23.6	3.2	164.5	8.2	1.98	3.3
Olympus MPlan	10	0.25	14.5	10.5	180	18	3.16	4.5
Nikon	4	0.2	11.5				3.95	
Zeiss EPIPLAN	5	0.13	7.5	19.8	164.5	33	6.08	4.3

Table 3.2.: **Objective specifications** (for $\lambda = 790$ nm and $n = 1$). WD: working distance, f_{TL}: tube length, $\mathrm{f}_{\mathrm{Obj}}$: focal length, $\mathrm{R}_{\mathrm{BFP}}$: radius of the back focal plane

3.9.5. Scattering Phantoms

To create a scattering phantoms agarose (3810.1, Carl Roth, Karlsruhe) was mixed with water and polystyrene beads of 0.75 μm (07309-15, Polysciences, USA) or 2.0 μm (L4530-1ML, Sigma-Aldrich, USA) diameter.

Preparation Protocol

1. 0.5 g agarose + 30 ml aqua dest. in a 100 ml (or bigger) beaker
   ⚠ agarose solutions can degas strongly
2. carefully heat on magnetic stirrer set to 140°C until agarose has been completely dissolved and stopped degassing (🕒 approx. 10 min)
3. after boiling add 1 drop of bead solution
4. pour solution into small petri dishes (∅ 4 cm)
5. let cool for 🕒 30 min

3.9.6. Reconstructions

All reconstructions shown here were processed on a 64bit Windows 10 Pro computer with a Intel Xeon CPU E5-2680v3 2.5 GHz processor and 64bit RAM. The NVIDIA GeForce GTX Titan X graphics card (3072 CUDA cores).
The reconstruction algorithm was written and executed in Matlab 2016a (Mathworks, USA) with DIPimage 2.8 (TU Delft, Netherlands).

Part II.

Fluorescence Microscopy

In the following Chapters 4-6, it is explored how recent advances in fluorescence microscopy can be translated into biomedical research to visualize previously unnoticed or unresolvable features and help answering questions about the morphology and biochemistry of the studied structures. The results of two interdisciplinary research collaborations using fluorescence microscopy and subsequent quantitative image analysis are presented.

In the first study, the possibility to specifically label proteins of interest with antibodies is exploited to elucidate the molecular architecture of podosomes in macrophages. Due to their small size (typically below 1 μm), super-resolution methods promise to yield new insights compared to previous studies with confocal microscopy. Complementary super-resolution techniques are performed to rule out imaging or reconstruction artifacts and different image analysis algorithms are applied to quantitatively analyze the acquired image data.

In the second study, autofluorescence of metabolites in gut sections is excited at 4 different wavelength. The different spectral properties of metabolites are used as a chemical contrast and the results are compared with other biophysical and biochemical methods.

Additional biological background information about the samples under study and experimental details where necessary will be given in each chapter.

4

Structured Illumination Microscopy of Macrophages

This chapter including figures has been previously published in [1][1].

4.1. Podosomes

Podosomes and the related invadopodia are receiving increasing attention due to their potential involvement in physiological events, such as monocyte extravasation and tissue transmigration, and pathological conditions such as atherosclerosis [95], osteoporosis [96] and cancer metastasis [97]. Normal podosome formation and dissociation accompanies the migration of myeloid cells. However, failure to make podosomes, as in the immunodeficiency disorder *Wiscott-Aldrich syndrome*, severely compromises the migration and chemotaxis of macrophages and dendritic cells. Podosomes share many similarities with focal adhesions, but in contrast to these more ubiquitous adhesion structures contain proteins that regulate actin polymerisation (the Wiskott-Aldrich syndrome protein WASp amongst others [98]), and seem to have the ability to tubulate and remodel the plasma membrane and degrade components of the extracellular matrix [99].

Podosomes are typically located at the ventral cell surface and mark sites of contact with the extracellular matrix or a substratum [100]. Each podosome consists of a core of actin filaments surrounded by a ring containing integrin-associated proteins such as talin, vinculin and paxillin, amongst others [101]. The ring complex connects cell surface integrin with the cytoskeleton. They have a dot or rosette-like appearance and measure 0.5–1.0 μm in diameter and 0.2–0.4 mm in depth [102]. The integrin-associated proteins, such as vinculin, appear to form round ring-like structures surrounding the acting core when imaged using confocal fluorescence microscopy (Figure 4.1A). Since their size is close to the diffraction limit (about 200 nm for standard labels) they are prime candidates for super-resolution imaging, as few details of the structure can be seen by standard fluorescence imaging.

The aim of this work was to investigate the structure and composition of podosomes by means of multi-colour high-resolution fluorescence microscopy and investigate whether new details of these structures could be revealed. We have identified the

---

[1] The manuscript was published under the Creative Commons Attribution (CC BY) license and no permission for reprinting it here is required.
The study was conducted in collaboration with Dr. Susan Cox, Dr. James Moneypenny and Prof. Gareth E. Jones from the Randall Division of Cell and Molecular Biophysics, King's College London.
Prof. G. E. Jones, Prof. R. Heintzmann and Dr. S. Cox conceived and designed the experiments and provided the material and reagents. M. Walde, Dr. J. Monypenny and Dr. S. Cox performed the experiments. M. Walde and Dr. S. Cox analysed the data.

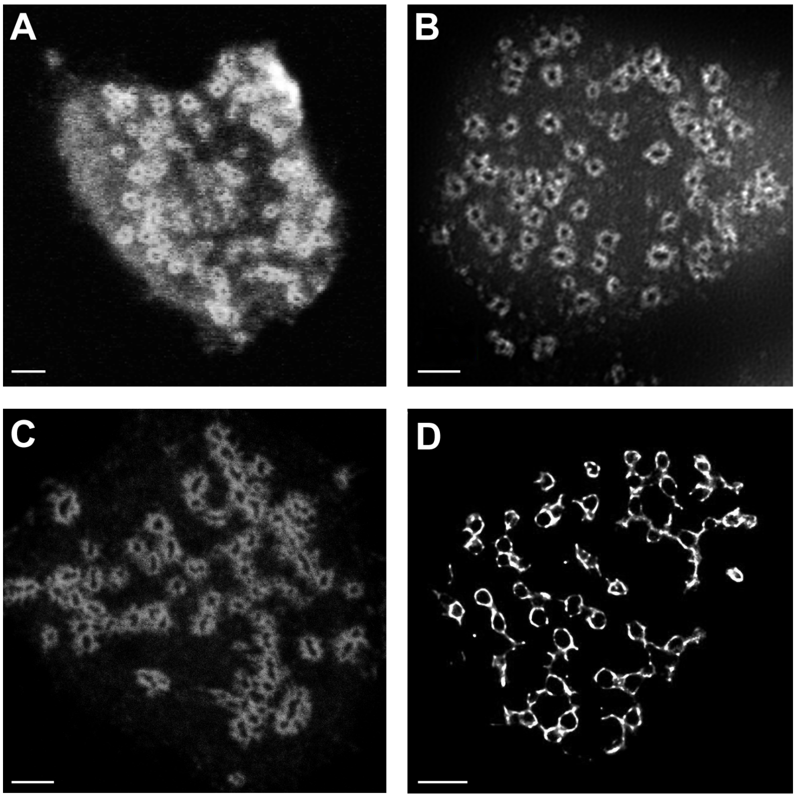

Figure 4.1.: **The podosome ring of actin associated proteins in THP-1 cells imaged with four different microscopy techniques.** *A:* A confocal image where vinculin is labelled with Alexa488. *B:* A SIM image where vinculin is labelled with Alexa488. *C:* A STED image where vinculin is labelled with ATTO-647. *D:* A 3B image where vinculin is labelled with Alexa488. All scale bars are 2 μm.

surrounding ring by labelling paxillin, talin and vinculin, which are a key components of this adhesion structure. Talin is an actin-binding protein composed of a head domain, which can dock onto the plasma membrane and bind actin and integrin, and a rod domain with several vinculin-binding sites. Talin is auto-inhibited in the cytosol, but it has been shown that mechanical stretching forces expose the vinculin-binding sites and thereby allow for the translation of a mechanical signal into a chemical one [103] Talin is regarded as a structural platform necessary for linking sites of adhesion with the contractile cytoskeleton [104]. Vinculin can bind to talin, paxillin, α-actinin and actin filaments, depending on its structural state. Its head domain regulates integrin dynamics, while the tail domain is involved in the mechanotransduction of forces [105]. Recruitment of vinculin to the podosome ring has been shown to be driven by myosin-dependent tension on the actin network [101]. Paxillin is a multi-domain scaffolding protein that contributes to the coordination of cell adhesion dynamics by interacting with numerous regulatory and structural proteins [106, 107].

The actin cores of podosomes have been imaged using scanning electron microscopy [108]. A dense actin core is clearly visible, with radiating actin fibres. However, sample preparation for this technique requires removing the plasma membrane, leading to an unquantified level of structural damage to the podosomes. Optical microscopy does not require this damaging sample preparation, and therefore should provide a more reliable structural characterisation; additionally, protein-specific staining is simple to perform for optical microscopy, allowing the structures formed by a number of proteins to be characterised.

4.2. Image Processing

4.2.1. Skeletonization

In order to measure the angles at which the strands of vinculin joined, the images were skeletonized (reduced to a set of lines). The resulting lines will be 8-connected, where a pixel can be connected to any of its eight nearest neighbours. This was used to identify corners where vinculin strands joined, and then the raw image in the region of these corners was fitted by modelling the corner as a number of line segments.

Skeletonization reduces an image to a set of lines which largely preserve the connectivity of the image [109]. First the images were thresholded, then repeated morphological thinning was carried out with the hit-and-miss transform, which matches pixel shapes with a specific pattern. Eight kernels, all rotations of a single kernel, were used. The resulting images were pruned by finding all endpoints and junctions, and removing all endpoint-junction segments that were less than 150 nm long (see Figure 4.4D, which shows the skeletonization of Figure 4.4C). Next, all *corners* of this skeleton were identified: Corners were defined as all such points where 3 or more lines join. These types of corners were present in those STED images where vinculin strands could be observed at the corners of podosomes. We then fitted a model which consists of several blurred line segments radiating from a point. The position of this point is the position of the corner, and the number of line segments is determined by the number of lines at the corner. The line segments are blurred with a Gaussian. The model is then fitted to the underlying image, keeping the position of the corner fixed and allowing the blur, segment intensity and intersection angle to vary.

The probability distribution was obtained using kernel density estimation [110]. The control for bias in the skeletonization process was performed by changing the intensity threshold to an extremely low value so that the skeletonization result obtained did not relate to the podosome structure. The observed angular distribution was compared using a chi-squared test to two null hypotheses: a uniform background and the background observed with incorrect skeletonization. Both tests found $P < 0.001$, confirming the significance of the result.

4.2.2. Immunolocalization Analysis

In order to quantify the immunolocalization of the ring proteins with respect to the actin core, podosomes are automatically identified in Matlab with a recently published algorithm [70], which separates podosomes in samples stained with phalloidin (for F-actin) based on intensity, size and shape. This algorithm has previously been applied to wide-field and confocal images of human dendritic cells. After segmentation, the distribution of ring proteins can be measured. Here, the average normalized intensity in a podosome with respect to the distance in nanometres from the centre of its actin core is calculated. Ring masks of 25 nm thickness and increasing radius around the core are analysed.

4.3. Experiments & Results

4.3.1. High-Resolution Microscopy

Both SIM and STED were used to image the vinculin ring of podosomes, with the SIM measurements also imaging actin (Figure 4.2A). Podosomes were found to be widely distributed over the substratum-attached side of the cell. It was clearly visible that each podosome consisted of an actin core surrounded by a vinculin-rich ring, as expected from the current podosome model.
However, the vinculin rings appeared to be polygonal rather than round (Figure 4.2B–D). For SIM, images were taken with both three and five grating directions, with the observed structures remaining the same.
Samples stained for paxillin and F-actin showed similar polygonal structures for paxillin to those seen for vinculin. These structures did not appear to be made up of straight strands, as observed for vinculin, but much more punctate (Figure 4.2E, F). We noticed two different talin configurations: it can be localized at the podosome core, co-localizing with actin (Fig. 4.3A–C) or in the adhesion ring (Fig. 4.3D–F). In many cases, Talin was observed to co-localize with vinculin forming very similar rings (Figure 4.3E).
The polygonal structures appeared to be made up of straight strands of vinculin 400-–600 nm long. Primarily pentagonal and hexagonal shapes were visible (Figure 4.2C, D). Joining points between two vinculin strands often had enhanced intensity, suggesting a higher concentration of vinculin. Vinculin strands were observed extending from the corner points of the structures, suggesting that new podosome growth is nucleated from the corners. Strands that connect neighbouring podosomes were observed as well (Figures 4.2C, D and 4.4B).

4.3.2. Skeletonization Analysis

Since the two dominant types of polygons observed have a similar binding angle, the angles at which the strands of vinculin joined were measured, to see if there was a dominant binding angle for vinculin strands within podosomes. To achieve this, first the image was skeletonized (reduced to a set of lines) (see Figure 4.4C–D). Figure 4.4E shows the fit of the skeletonization to the original image. The values of all intersection angles were plotted as histograms. Figure 4.4F shows a probability distribution of the angular distribution for the 1761 corner points over four STED images including Figure 4.4A–C. These images were selected because they displayed distinct podosome structures in which the vinculin strands were well defined. In other images, podosomes could be partially joined into ill-defined structures, mak-

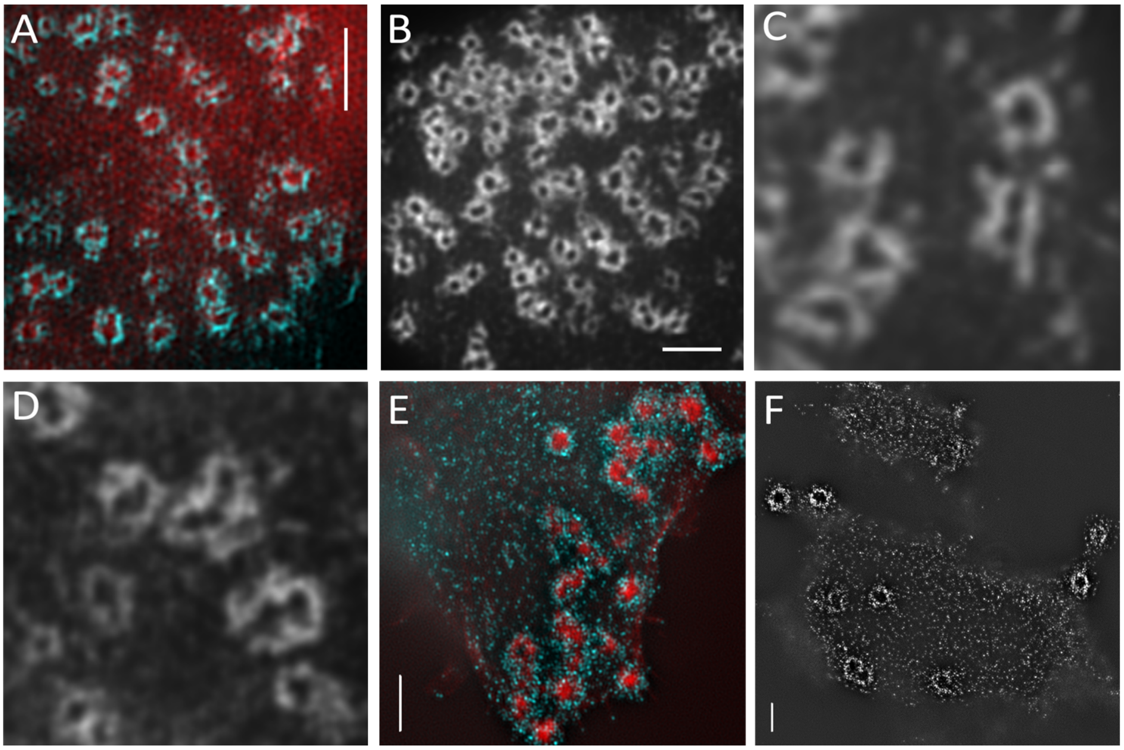

Figure 4.2.: **SIM images show polygonal structure of podosomes.** *A:* Immunolocalization of actin (red) and vinculin (blue) in podosomes. SIM image of podosomes recorded with 3 different grating directions and 5 grating phase positions showing the actin core surrounded by a vinculin-enriched protein ring. *B:* SIM images of vinculin rings of podosomes, imaged with 5 different grating directions. The podosome rings appear to have a polygonal structure with both 3 and 5 grating directions. *C, D:* SIM images of vinculin rings. Vinculin strands on the corners of podosomes are visible. (*E, F:*) Immunolocalization of actin (red) and paxillin (blue) in podosomes. SIM images were recorded with 5 grating directions and 5 grating phase positions. Paxillin rings appear polygonal, too, but are more punctate than the vinculin rings. All scale bars are 2 μm.

ing analysis difficult, or the vinculin strands could appear thicker, probably due to the lack of z-resolution in our STED system (700 nm). The probability distribution is plotted against a control for bias (see Methods section). It can be clearly seen that while the skeletonization does appear to have an intrinsic trend, there is a clear peak above background when the podosomes are correctly identified. The modal binding angle of vinculin strands in the STED images was found to be 116°with a shoulder at 135°(Figure 4.4D). The skeletonization analysis was also performed on the SIM images. However, the background distribution for the SIM images was found to have an inherent bias towards values just above 100°, probably because the deconvolution process leads to artefacts in the background which intersect at angles determined by the number of grating directions used.

Susan Cox also carried out live cell imaging with 3B localization analysis to find out more about the dynamics of the binding angles. Images were taken every 10 s (9 s for the last image). Analysis of these images showed that the binding an-

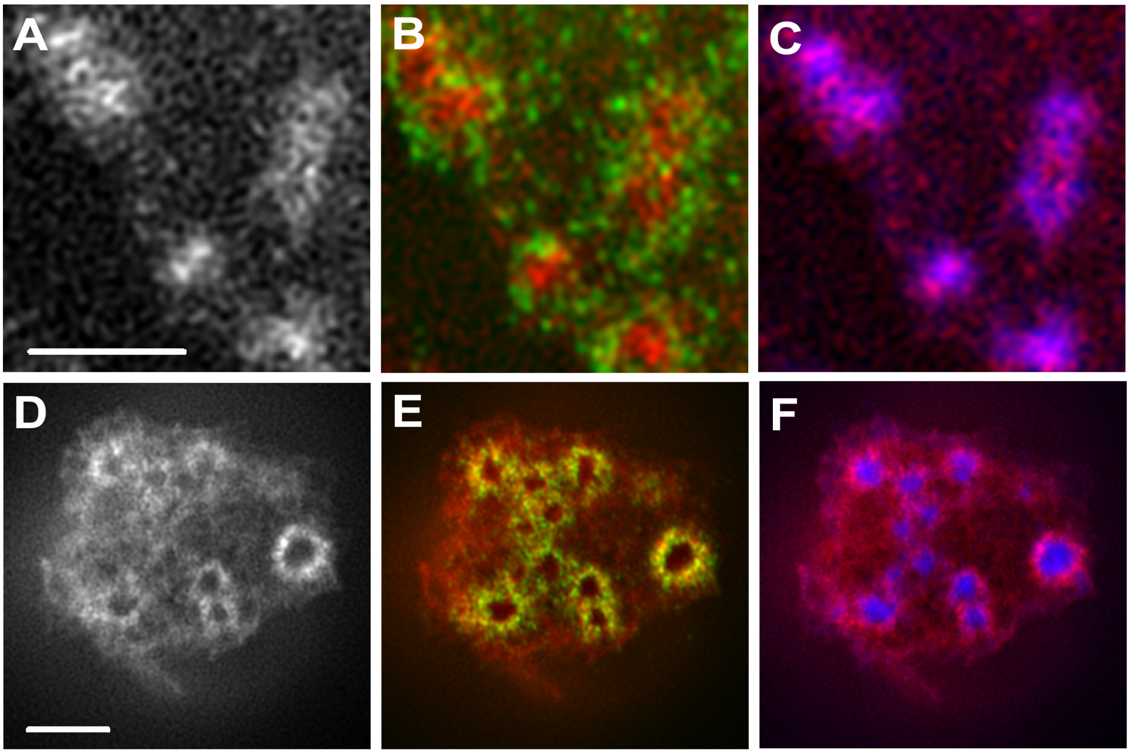

Figure 4.3.: **Talin was observed in two different configurations.** *A–C:* Talin is localized at the podosome core, possibly due to podosome dissociation. *D–F:* Talin is localized in the adhesion ring in steady-state podosomes. *A,D:* SIM immunolocalization of talin. Scale bars are 1 μm. *B,E:* SIM immunolocalization of talin is shown in red and paxillin (B) or vinculin (E) in green. *C,F:* SIM immunolocalization of talin is shown in red and actin in blue.

gle in podosomes fluctuates with peaks between 120°and 135°with mean peak at 130.5°±5°(Fig. 4.4E). For comparison, the inner corners of flat, regularly shaped pentagons (108°), hexagons (120°), heptagons (128.6°) and octagons (135°) are given as grey lines (Fig. 4.4F).

4.3.3. Immunolocalization Analysis

Protein distributions around the actin cores were evaluated in 480 podosomes stained for actin, 339 for paxillin, 401 for talin and 141 for vinculin. The resulting normalized intensity distributions are shown in Fig. 4.5 and results are summarized in Table 1. Paxillin and vinculin form distinct rings with peaks at distances $d_{pax} <$ 275 nm and $d_{vin} <$ 225 nm. The paxillin ring is broader ($FHWM_{pax} <$ 385 nm) than the vinculin ring ($FHWM_{vin} <$ 320 nm). In the histogram, talin appeared almost homogeneously distributed, because the calculated average distribution contains a mixture of the different observed and possibly intermediate situations.

Furthermore it was investigated whether the distributions of actin and vinculin in podosomes that occur in clusters differ from individual ones. A distance matrix for all identified podosomes was calculated and a threshold 1.075 μm of mean

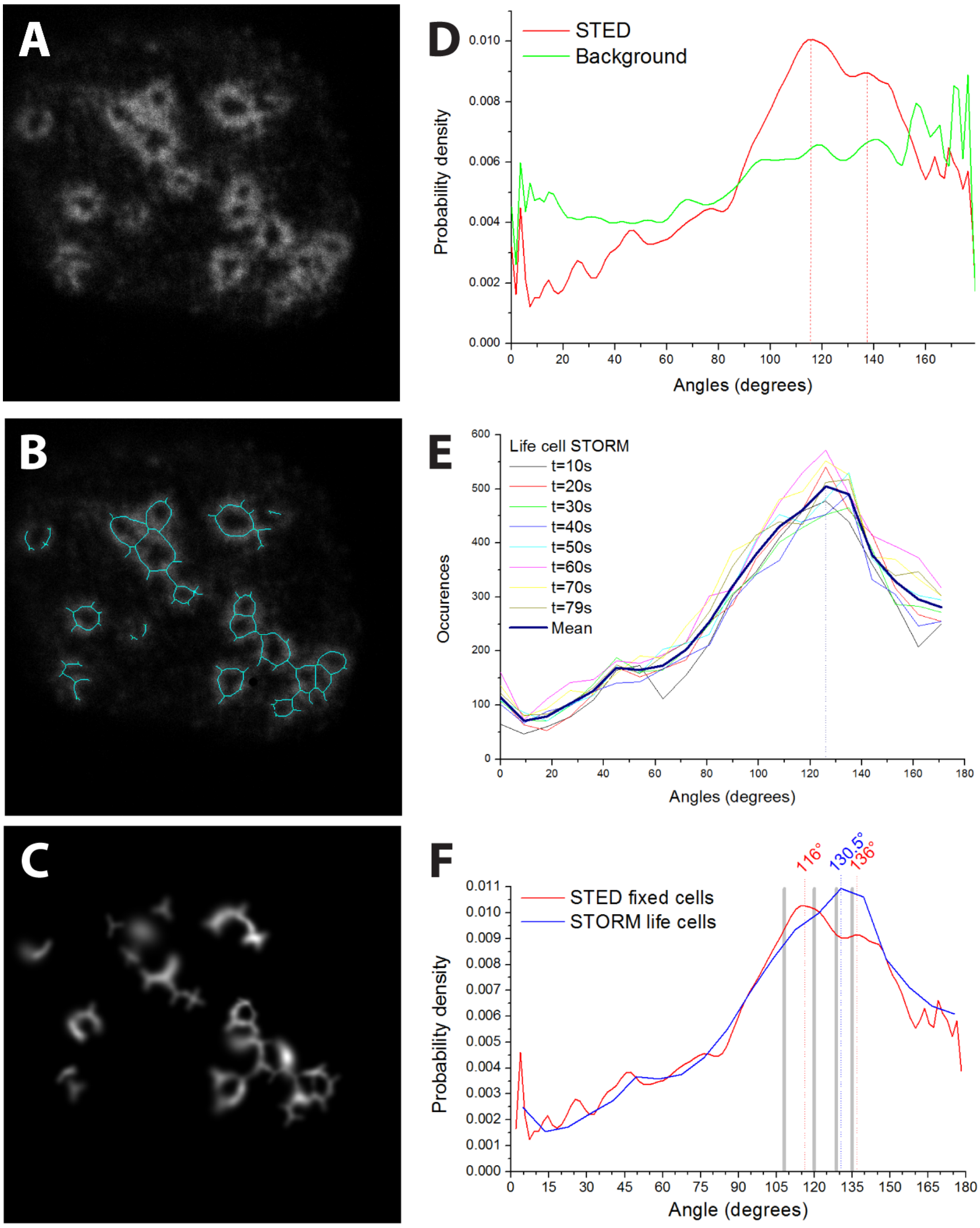

Figure 4.4.: **Dominant vinculin binding angle in podosomes.** *A:* STED image of vinculin rings of podosomes. The vinculin rings appear distinctly polygonal, with vinculin strands apparently nucleating from corner points. *B:* Skeletonisation of image A shown in blue. *C:* Result of fitting blurred line segments to the underlying image A at corners shown in B. The intensity of the Gaussian line segment is displayed. The background and line segments wider than 10 pixels are not displayed for clarity. *D:* Probability distribution of angles at vinculin corners in STED images of fixed cells: a peak at 116°with a shoulder at 136°is observed above the background. *E:* Localization microscopy on live cells shows that the binding angle in podosomes fluctuates in the range of 120°to 135°(mean peak 130.5°±5°), but is not time-dependent. *F:* Overlay of results from E & F. Dotted lines indicate dominant binding angles. Grey bars represent the inner angles of flat pentagons (108°), hexagons (120°), heptagons (≈128.6°) and octagons (135°).

Protein	Plot colour	Peak of distribution	FWHM	R^2 of Gaussian fit
		[nm] from core centre	[nm]	
Actin	black	0 [ref]	349	0.9888
Paxillin	red	275	385	0.9025
Talin	green	0	244	0.9904
Vinculin	blue	225	320	0.9709

Table 4.1.: **Results of immunolocalization distance analysis.** Radial distance of the peaks, FWHM and R2 of fit to Gaussian is given for fluorescence intensity distributions of different proteins of the podosome scaffold. Distributions are plotted in Fig. 4.5.

distance to the 3 closest neighbours was determined to select clusters. 207 clustered and 297 individual podosomes were analysed. The resulting average normalized intensities with respect to the distance from the core are plotted in Fig. 4.5A&B. The typical distance (core-to-core) between neighbouring clustered podosomes was (730 ± 125) nm, while actin cores of individual podosomes were on average (1.3 ± 0.4) μm apart. Differences concerning the vinculin binding angle between clustered and peripheral podosomes were not found. Actin cores did not appear polygonal in our images, possibly because of limited optical resolution.

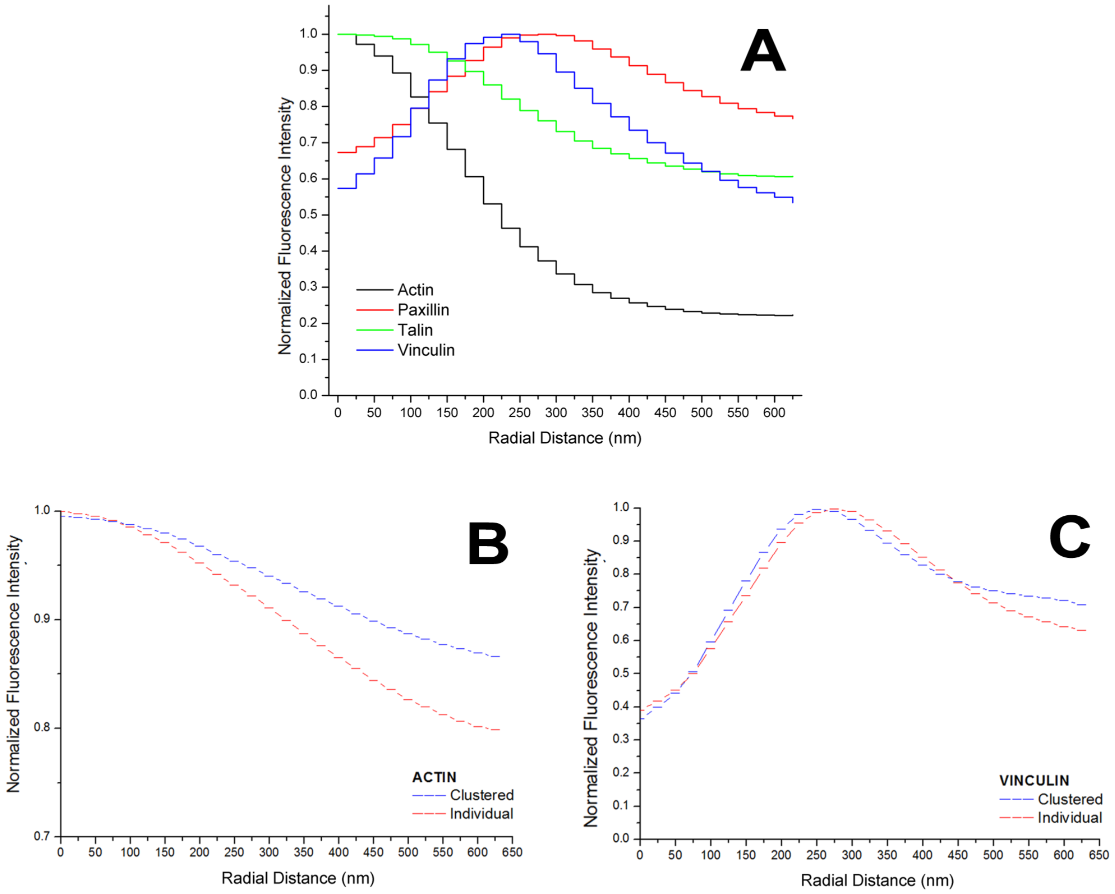

Figure 4.5.: **Immunolocalization analysis and comparison of clustered and individual podosomes.** *A:* Radial distributions of actin (black), paxillin (red), talin (green) and vinculin (blue). The normalized average intensity of the immunolocalization is plotted with respect to the radial distance from the centre of the actin core. *B-C:* Comparison of actin (B) and vinculin (C) distributions in clustered (blue) and individual cells (red).

4.4. Discussion

Two-colour SIM and STED imaging reveals previously unnoticed detail of podosome architecture. Immunofluorescent staining of paxillin and vinculin shows rings surrounding the actin core, confirming the current podosome model. However, their shape does not appear round, but exhibits distinct corners. This is unexpected since the actin structures observed using scanning electron microscopy do not appear polygonal [108], and when using optical imaging methods at standard diffraction-limited resolution the vinculin ring appeared roughly circular.

Different talin localizations were observed. Talin localized in the centre of the podosome suggests podosome dissociation in which talin is drawn to the centre and eventually removed, as revealed by live cell microscopy [69]. At steady-state, the talin ring co-localizes roughly with vinculin.

With a skeletonization algorithm a modal binding angle of around 116°in the vinculin rings of podosomes in our STED data was identified. To control for bias in the skeletonization algorithm a chi-squared test was used. A distinct modal binding angle is already known for filaments such as those of the actin core which bind at 70°[111]. This dominant binding angle is thought to arise from interaction between actin and the nucleator known as the Arp2/3 complex [112]. The binding angle that was observed for vinculin is close to the outer binding angle of actin (180˘70 = 110), and actin strands have been observed in the region of the vinculin rings [113]. 3B localization microscopy of live cells showed that the binding angle in live podosomes fluctuates on a time scale of seconds in the range of 120°to 135°.

Image analysis of the immunolocalization experiments shows that the different proteins of the ring have different localizations within the podosomes as suggested in previous studies [69, 70]. It can be confirmed that the vinculin ring is closer to the core than the paxillin ring. The diameter (FWHM) of the actin core was found to be approximately 350 nm, which matches other fluorescence and EM studies.

The morphology of clustered and individual podosomes was found to be very similar. While the typical distance between vinculin ring and podosome centre remained the same, actin levels were higher in the periphery of clustered podosomes. Actin fibres are known to radiate from podosome cores. A likely explanation for the increased actin levels are interactions between neighbouring podosomes [108].
Vinculin strands that are observed at the corners of podosomes may be starting points for the self-assembly of new podosomes. This observation strongly suggests that new podosomes can nucleate from the corners of existing structures. In another study using 3B localization microscopy S. Cox et al were able to show evidence for this hypothesis [69]. Podosomes that appeared to be connected to each other via vinculin strands were also observed. It raises a number of interesting questions with regard to how the podosomes form: Does the vinculin structure of podosomes predominantly form by a strand being continuously laid down from one nucleation point? What determines when a new strand in a different direction is initiated? And what is the relationship between the formation of the actin core and the protein-enriched ring?
The fact that the modal vinculin binding angle is in the range of the inner angle in flat pentagons (108°) and hexagons (120°) to heptagons (≈128.6°) and octagons (135°) suggests that podosomes may tile the cell adhesion sites with a mix of polygonal structures.

Mixed hexagonal and pentagonal tiling is frequently found on curved surfaces (the tiling pattern of a football being a nice example). The choice between different lattices allows for adaptation to arbitrary surface shapes, which is probably relevant for migrating podosome-forming cells in vivo. In such a lattice, vinculin has a high packing efficiency: the attachment area can be covered with minimal amounts of vinculin molecules.

5

Auto-fluorescence Microscopy in Insect Larvae Guts

This chapter including figures has been previously published in [2][1].

5.1. Motivation

Chlorophylls (Chls), the green pigments required for photosynthesis in plants, algae, and bacteria, are also part of the daily diet of herbivorous insects [114]. Chlorophyll degradation occurs in nature during leaf senescence and fruit ripening, but also is noticed as a response to biotic and abiotic stresses [115, 116, 117]. The biochemistry of Chl degradation to linear tetrapyrroles has been studied in higher plants over the last three decades [118] . While the process of Chl degradation is largely known *in planta* [117], our knowledge on the chemistry and biochemistry of Chl degradation in plant-feeding insects is rather limited. The only qualitative analysis of Chl degradation products has been reported for the frass of the silkworm *Bombyx mori* [119]. Chlorophylls and their derivatives generally form pigment–protein complexes to participate in photochemical processes of biological importance [120].
As larvae of Lepidopterans feed exclusively on plant leaves, chlorophyll and its catabolites occur in their gut juice and fecal matter, and are utilized in the biosynthesis of pigment–protein complexes, like the red fluorescent proteins [121]. Most of the lepidopteran guts contain a peritrophic membrane lining in their midgut that shows the presence of several polycalin isoforms in their proteome [122, 123, 124] . Polycalins are most likely GPI-anchored to the brush border membrane, but they also are found in soluble forms in the guts of several Lepidopterans [122]. In B. mori, polycalin binds and reacts with chlorophyllide, producing a protein complex with broad-spectrum anti-microbial activity [125] that may account for the insect's enhanced resistance when fed a Chl-rich diet and exposed to light [122, 126].

---

[1] It is reprinted here with kind permission of Springer Science+Business Media, New York.
The study was conducted in collaboration with Amarsanaa Badgaa & Prof. Boland and several other scientists (see below) from the Max Planck Institute for Chemical Ecology in Jena.
Dr. A. Badgaa and Prof. W. Boland designed the study and wrote the manuscript for this publication. In particular, the ecological background (5.1) and the discussion of the biological relevance of the results (5.4) have been contributed to the manuscript by Dr. A. Badgaa and Prof. W. Boland and are quoted here to clarify the context of this study. Dr. A. Badgaa also conducted the experiments and analysed the data. Dr. R. Büchler, Dr. N. Wielsch, Dr. A. Svatos, Dr. Y. Pauchet and Prof. R. Heintzmann participated in the experimental design. M. Walde conducted the microscopy experiments and image analysis and contributed the experimental description to the manuscript.

5.2. Experiments

A range of biochemical and biophysical techniques have been applied in this study, including gel electrophoresis (SDS-PAGE), liquid chromatography-mass spectrometry (Nano LC-MS), bioinformatic data analysis with MS BLAST, flash chromatography and matrix-assisted laser desorption/ionization time-of-flight mass spectrometry (MALDI-TOF).

The publication reports the identification of the binding protein(s) as a known lipocalin-type chlorophyllide-binding protein (ChlBP) [124, 127] that was originally isolated and described for *B. mori* [125]. Using MALDI-TOF and auto-fluorecence microscopy, the distribution of chlorophyll degradation products along the insect gut is visualized. Auto-fluorescence results are presented below. The results of all other experiments are not shown here, but relevant results are mentioned where necessary.

5.2.1. Visualization of ChlBPs in the Gut of *S. littoralis* Larvae by Auto-fluorescence Microscopy

Larvae of *S. littoralis* (3rd instar) reared on lima bean for 2 days were anesthetized by chloroform absorbed on cotton wool. Amarsanaa Badgaa dissected the guts of the anesthetized insects under a microscope for further experiments. The dissected guts were washed 3 times with phosphate buffered saline (PBS) and immediately frozen in liquid nitrogen. The sample was embedded with 70% polyvinyl alcohol (PVA, Tissue-Tek, Sakura Europe, The Netherlands) and maintained at -55°C. Embedded samples were cut to 60 μm cross-sections by a Microtome (Cryo-Star HM 560 M, MICROM Int. GmbH). Thin slices were mounted onto SuperFrost Ultra Plus glass slides (Thermo Scientific) and covered by glass (18×18×0.17 mm, ZEISS, Germany).

All auto-fluorescence images were acquired on the ZEISS Elyra S.1 microscope. For an initial overview, transmission and dual-color laser widefield images of the microtome cross-sections were acquired in laser widefield mode without pre-treatment with a 1.4/63× oil immersion objective.

To achieve a bigger field of view and capture the entire gut sections, a tile scan mode was selected. Images at hundreds to thousands of adjacent positions over several square millimeters were acquired and fused to large tile images. Each tile consists of 1004×1002 pixels. Samples were excited with 100 mW of 488 nm and 3.5 mW of 642 nm laser light for 50 ns.

For a more detailed gut surface analysis, four different sample preparations of gut membrane were prepared: Samples of larvae raised on chlorophyll-free food were compared to samples of larvae raised on plant-food after short-term and long-term washing. Additionally, tissue samples of chlorophyll-free larvae were washed in a chlorophyll solution. The dissected guts were cleaned in 0.9% NaCl for 20 min on the shaker.

Microscopy samples of the inner and outer membrane were prepared for each category. Areas of outer and inner membrane were determined from transmission microscopy images.

5.2.2. Localization of ChlBPs in the Gut Membrane of *S. littoralis* Larvae by SIM

Sample preparation was identical to the short-term washed plant-food samples described above. SIM images over a range of focal positions were acquired with a 1.4/63× oil immersion objective and reconstructed by the commercial ZEN software (ZEISS, Germany).
Excitation dosages for the focal series were 1.25 mJ at 561 nm and 0.175 mJ at 642 nm. The focal range is 69 μm, and the lateral size is approx. 75×75 μm^2. Three grating pattern directions were recorded. Image analysis was conducted with the View5D plugin (written by R. Heintzmann) for ImageJ (v 1.45 s, NIH, USA).

5.2.3. Enzymatic Degradation of the GPI-Anchor

Dissected guts were cut longitudinally into two segments. One was incubated at 30°C with phospholipase C (Sigma-Aldrich Chemie GmbH, Germany) for 30 min, while the other served as a control.
To calculate the mean auto-fluorescence intensities of each sample, the dark background (which had a different area for each sample and could thus distort the result) was removed by a threshold mask. The mean was calculated from the intensities of the remaining pixels. Image analysis was conducted in Matlab (v7.7, The Mathworks, USA) with the DipImage toolbox (v2.3, TU Delft, The Netherlands).
To determine the mean auto-fluorescence intensities over the entire gut sections, tile scans were acquired with 10× magnification in laser widefield mode. Each image consists of 1002×1004 pixels (800×800 μm^2), and approximately 10×10 images were tiled together to cover an entire sample. After subtraction of the dark background offset, the mean fluorescence intensity over the entire sample was calculated. In order to compare the results from different larvae, mean fluorescence levels and errors were normalized. The average fluorescence intensity after washing with phospholipase C was taken from three biological replicates.
Image analysis was conducted in Matlab (v7.7, The Mathworks, USA) with the DipImage toolbox (v2.3, TU Delft, The Netherlands).

5.3. Results

5.3.1. Visualization of ChlBPs in the Gut of *S. littoralis* Larvae by Auto-fluorescence Microscopy

The isolated and dissected the gut tissue of *S. littoralis* were imaged and show the presence of the ChlBP in cross-sections and longitudinal sections. The images show that the inner surface of the gut membrane is covered with auto-fluorescent molecules, that show a fluorescence emission characteristic for the ChlBP [125]. The fluorescence distribution in a gut cross-section of *S. littoralis* is shown in Fig. 5.1. Samples were excited at 488 and 642 nm and previously calibrated with references of Chl a, pheophorbide a and pyropheophorbide a, the major catabolites in Chl degradation. The recorded auto-fluorescence is shown in forced colours as green

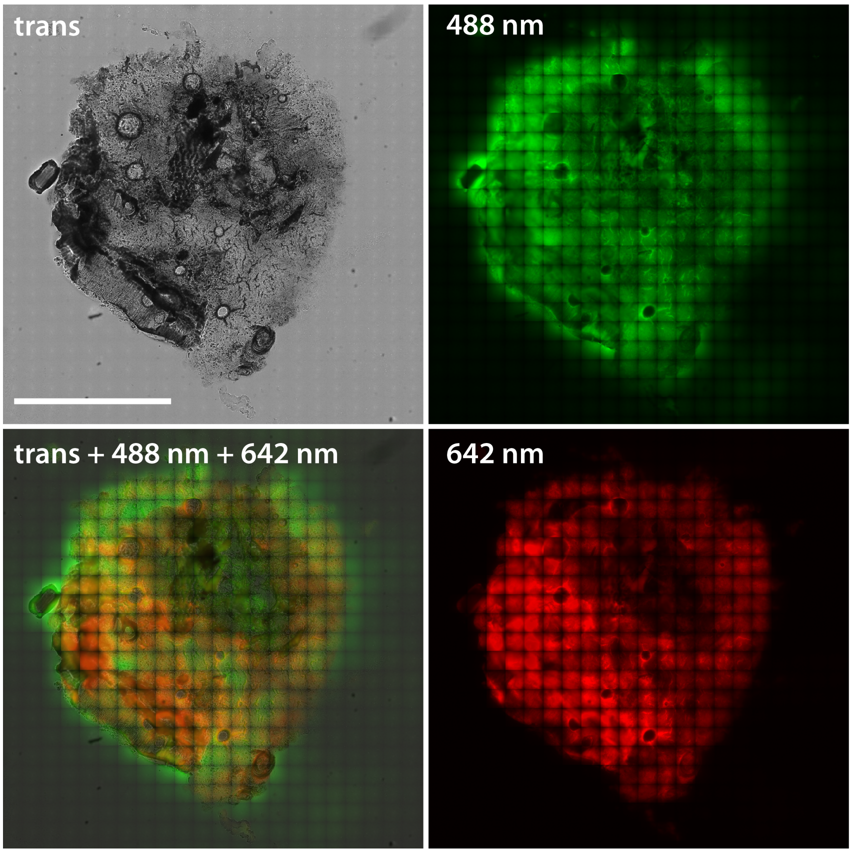

Figure 5.1.: **Combination of transmission microscopy with laser widefield auto-fluorescence imaging** of a cross-section of the gut of *S. littoralis*. The unstained gut membrane and the gut lumen show the presence of the chlorophyllide binding protein along with free Chl catabolites. Emission was monitored after excitation at 488 nm (green) and 642 nm (red) (forced colours). Large gigapixel tiles scans were recorded to capture the entire sections. Scale bar: 1 mm.

(λ_{em}=495-550 nm) and red ($\lambda_{em} > 655$ nm), respectively, and are superimposed with a transmission image shown in grey.
Overview tile scans in the inner membrane (upper image) and outer membrane (lower image) were acquired for four different sample preparations:

A) The gut tissue from larvae raised on artificial diet (Chl-free food) were short-term (20 min) washed and show no occupation of Chl.

B) Same as A, but shortly (20 min) immersed in Chl-containing solution. They are slightly emitting Chl fluorescence.

C) Gut tissue from larvae raised on plant leaves were washed for short-term and show full occupation with Chls.

D) Same as C, but washed overnight. These samples show a significant removal of Chl from the gut wall.

The overview image on page 59 shows a matrix of images with the experimental results. Rows contain the preparations (A–D) for an inner and an outer membrane

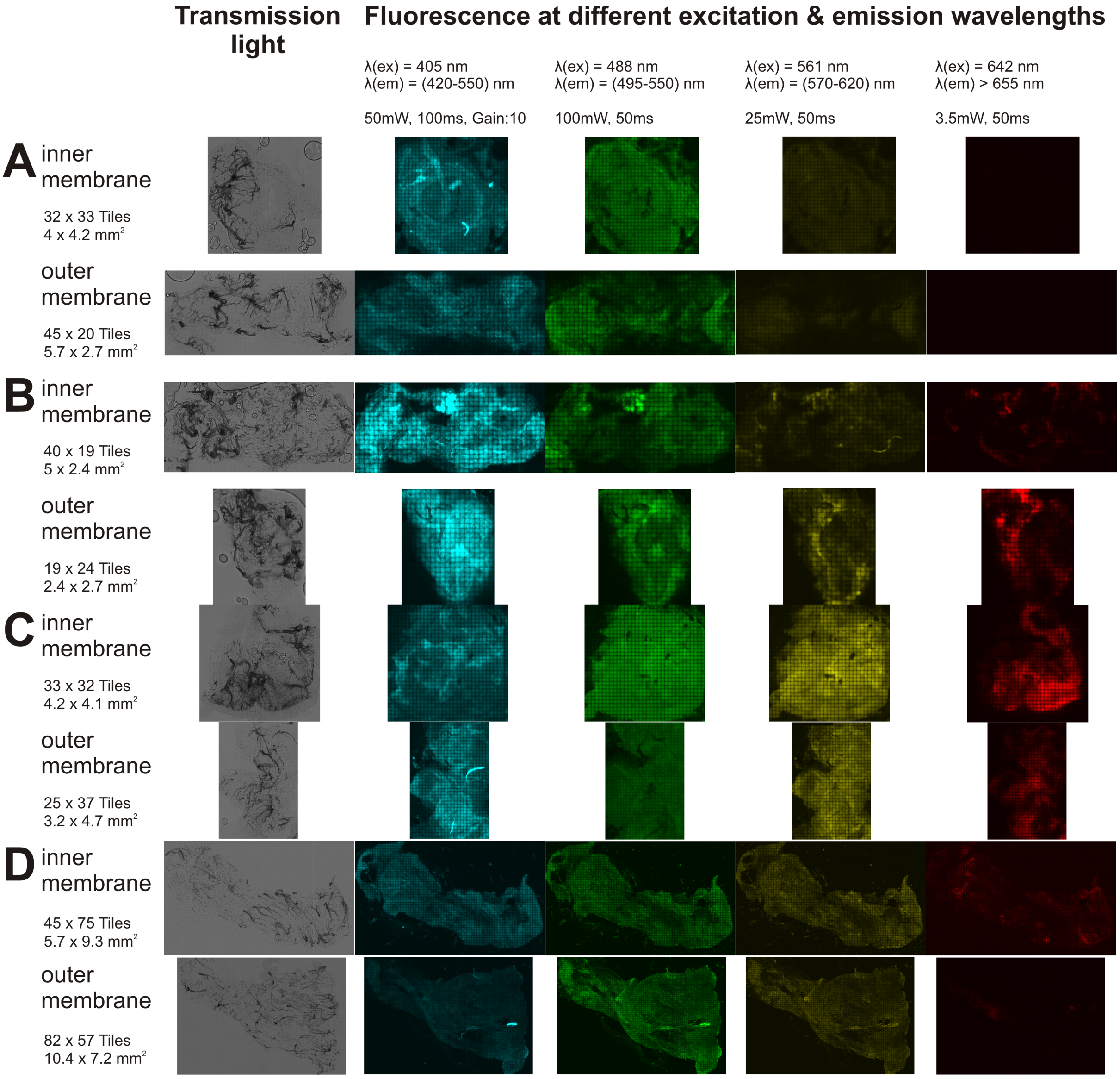

Figure 5.2.: **Combination of transmission microscopy with laser widefield autofluorescence imaging** of gut cross-sections from different preparations of *S. littoralis*. *A-B:* were raised on Chl-free artificial diet, *C-D* were raised on plant food, but D was washed overnight.

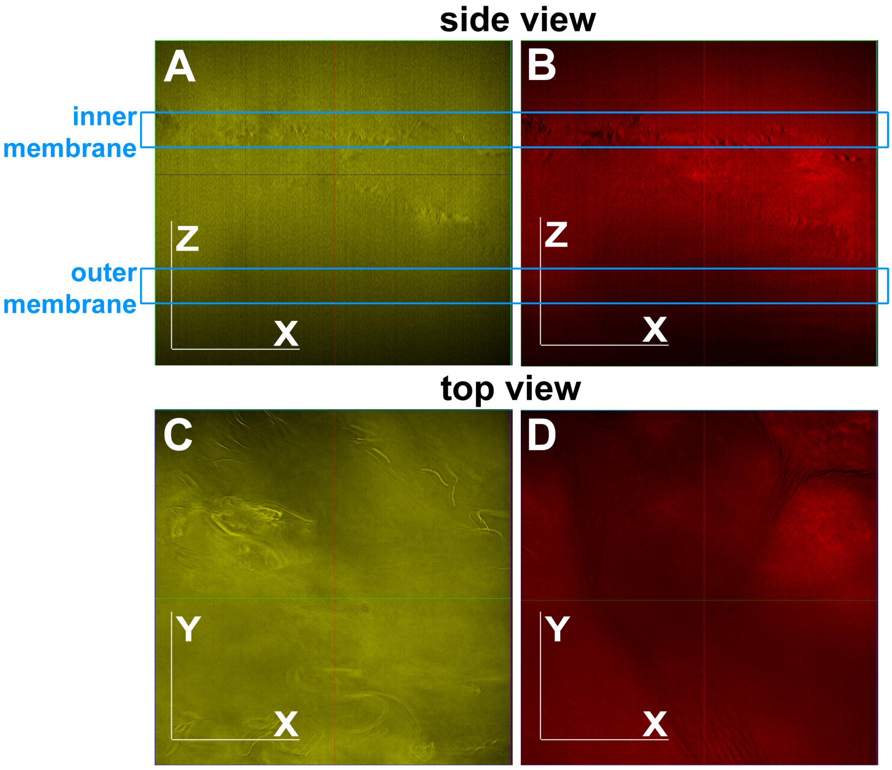

Figure 5.3.: **Focal series of SIM images** across dissected gut of *S. littoralis* larvae upon excitation at 541 nm (yellow) and 642 nm (red). The emission intensity in the outer membrane layers is only 66% of the intensity in the inner membrane.

sample. The sizes of the recorded areas are given for each sample. Columns contain the different excitation wavelengths, emission ranges, laser power and exposure times.

The samples from insects hatched and reared on artificial diet showed no auto-fluorescence upon illumination with 642 nm, in line with the lack of chlorophyll catabolites bound to ChlBP. According to the presence of a GPI-anchor in the ChlBP, the protein complex should be attached to the brush border membrane of the intestinum [123]. Prolonged washing (12 h) of fluorescent gut tissue from plant-reared insects with buffer diminished the fluorescence, thus indicating a non-covalent binding of the chlorophyll metabolites to the gut membrane.

5.3.2. Localization of the Chlorophyllide-Binding Protein in the Insect Gut by SIM

To reduce the abundant out-of focus light and achieve a better localization of ChlBP emission in the gut membrane, SIM images were acquired. We recorded a focal series through the gut membrane for 561 nm and 642 nm excitation.

The focal series across the dissected gut was merged into a 3D volume (X×Y×Z) which is shown in Fig. 5.3. The side view of the recorded volume shows a cross-section through the examined tissue (upper images). Areas that correspond to

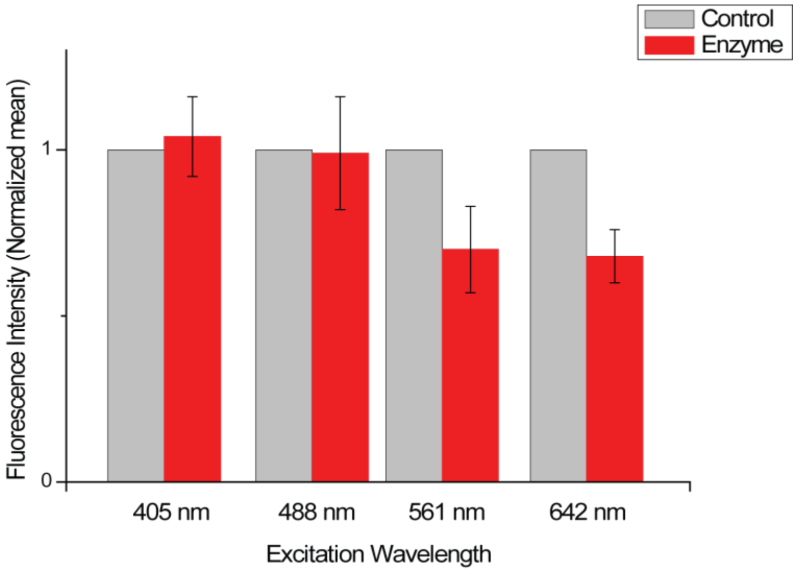

Figure 5.4.: **Effect of phospholipase C on the chlorophyll binding protein (ChlBP).** Shown are fluorescence intensities (normalized mean) of Chlide-binding protein attached to the dissected gut wall of *Spodoptera littoralis.* Phospholipase C treatment of the gut tissue (red bars) was compared with buffer-treated controls (gray bars). Measurement was done using four different illumination lasers for excitation. Exitation at 405 and 488 nm served as controls. Exitation at 561 and 642 nm affect the protein bound Chl-catabolites. Error bars indicate mean of three replicates.

the inner and outer membrane were determined from transmission images and are highlighted in blue. A drop in fluorescence intensity from the inner to the outer membrane is visible. Lower images show one focal slice of the volume (position indicated by a line through the side view).

5.3.3. Degradation of the GPI-Anchor of ChlBP by Phospholipase Treatment

Phospholipase C (PLC) is an enzyme that is known to cleave the phospho-glycerol bond typical for GPIanchored proteins [128]. Thus, treatment with PLC should cause a release of the GPI-linked ChlBP from the gut membrane. In consequence, the auto-fluorescence should vanish in a time dependent manner after treatment with PLC. As shown in Fig. 5.4, the fluorescence intensity of the ChlBP attached to the gut membrane was significantly reduced after 30 min treatment with a solution of phospholipase C. Affected were only the emission bands resulting from excitation at 561 and 642 nm. The latter are typical for ChlBP, while the excitations at 405 and 488 nm showed no effect (controls, aromatic amino acids, phenols, and free chlorophyll catabolites).

The effect of phospholipase confirms that the fluorescence observed at the gut membrane is, in fact, due to the ChlBP that is loaded with chlorophyllide and eventually other chlorophyll catabolites. The phenomenon is observed along the whole gut, and is dependent on the uptake of chlorophyll with the ingested food. Due to reversible binding, the coverage of the gut membrane with the ChlBP is reduced upon prolonged uptake of Chl-free diet. The same effect was achieved by prolonged washing of the fluorescent gut membrane.

5.4. Discussion of Biological Relevance

In summary, according to the auto-fluorescence microscopy results, the gut membrane is largely covered with the fluorescent ChlBP. Due to reversible binding via its GPI-anchor, large amounts of the protein also occur in the gut lumen (depending on the presence of phospholipases). The protein consists of several lipocalin domains (up to 15 for *S. littoralis*) and easily reaches molecular weights of $>$1 MDa [123]. Moreover, the protein is not recycled in the gut, but excreted with the feces [121]. Due to this huge investment of biosynthetic energy into ChlBP, the protein should be of special importance for the insect. The arrangement of the ChlBP lining the brush border membrane of the intestinum also might have a functional relevance. Especially, as the ChlBP is widely spread in the midgut of all Lepidopteran species, e.g., *B. mori*, *M. sexta*, *H. armigera*, and *S. littoralis*, all of which were studied recently with respect to chlorophyll degradation [129, 130]. ChlBP has been reported as antiviral and antibacterial due to the binding of Chlide, especially in the presence of light [122].

An outstanding property of many Chl catabolites is their ability to activate molecular oxygen in the presence of light to produce highly toxic singlet oxygen [131]. Although the insect gut is an anoxic area, demonstrated by absence of oxydatively cleaved Chl metabolites and by the high density of Clostridia in the gut [132], the only area with limited availability of oxygen is the hemolymph embedded gut membrane. Due to the alignment of ChlBP along the peritrophic membrane, even limited access of light might lead in the presence of molecular oxygen to the formation of the short lived singlet oxygen. Together with H_2O_2 produced by the cells of the gut membrane, the reactive oxygen species may serve the insect to prevent infections by the gut bacteria and fungi. The same formation of singlet oxygen also may contribute to the previously reported deterrent property of the fecal shields of tortoise beetles [133].

6

Discussion of SIM as a biomedical imaging tool

The results presented in Chapters 4 and 5 demonstrate that both the resolution enhancement and the optical sectioning capabilities of SIM can be utilised to make previously indiscernible structural details visible. This allowed for a finer localization of the substances of interest and helped founding a hypothesis about their biochemical role.

The results of chapter 4 have demonstrated that high resolution fluorescence microscopy enables the observation of the fine structure of biological samples below the diffraction limit, allowing us to see previously unnoticed details of the protein architecture of podosomes. In combination with image processing techniques, a mathematical analysis of these features allows for the characterization of geometrical attributes of sub-cellular structures.

The price for increased resolution is the at least 9 times higher number of images that need to be acquired, which increases light exposure, acquisition time, accumulated data and demands of computational power (since the acquired raw images have to reconstructed in Fourier space). In particular for the insect larvae samples, the handling of large image data posed a challenge. Tile scan images easily reached a size of ≈ 1 GB each and were thus recorded as widefield and only where better optical sectioning performance was required, a small representative region of interest was chosen and SIM images were recorded.

Acquistion time and computational power can be considered as soft technological limitations. A novel fastSIM system based on a spatial light modulator (SLM) significantly improves the acquisition speed [134].

For imaging situations, where out-of-focus light is undesirable but sample light exposure is critical, light sheet–based fluorescence microscopy (LSFM) may be used to minimize fluorophore bleaching and phototoxic effects [135].

In both studies presented here, the possibility to image fluorescence with multiple colours has proven to be an invaluable asset of this method.

Part III.

Coherent Imaging

7
Extended Focus Illumination for OCT

In this chapter, the possibility to enhance the depth of field in optical coherence tomography without compromising its lateral resolution by using Bessel beam illumination is explored.
Because OCT is a broadband imaging method, the use of an axicon would lead to dispersion effect in the illumination. Instead, a spatial light modulator (SLM) can be used to create an achromatic Bessel beam. Furthermore, the applicability of an image inversion interferometer for detection in combination with Bessel illumination is investigated.

7.1. Calibration of a Spatial Light Modulator for Beam Shaping

SLMs consist of a liquid crystal on silicon (LCoS) chip and a driver unit, which connects the SLM with the DVI port of a computer (see Fig. 7.1). Images produced, for example, in Matlab are displayed according to the colourmap settings and processed as 8-bit integers [0;255]. These values are translated according to the driver unit's internal look-up-table (LUT) into voltage sequences. In this manner, the electric field across the liquid crystal layer can be controlled pixelwise. It leads to a tilt of the liquid crystal molecules and a change in refractive indeces (n_0, n_e) and hence optical path length which varies the incoming wave by $\Delta\varphi(x, y)$.
The colourmap and LUT might however not translate the displayed image linearly into phase modulations and the SLM surface itself is generally not manufactured

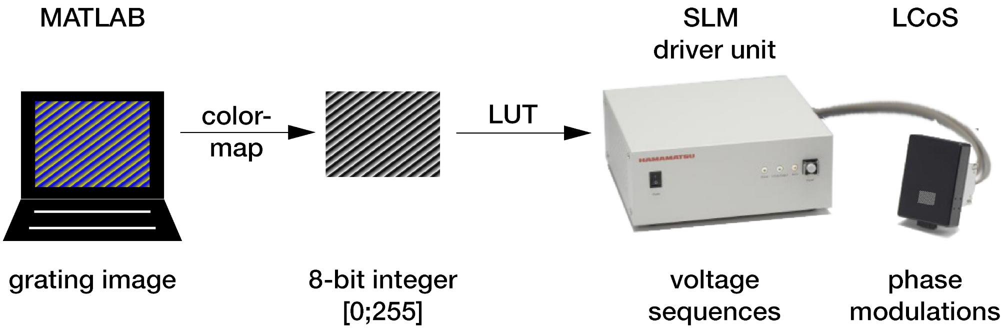

Figure 7.1.: **Operation of spatial light modulators** (SLMs). Gray-level images displayed by the computer are translated into voltage levels by the SLM driver unit which again translate into pixelwise phase modulations on the incoming plane and linearly polarized wave.

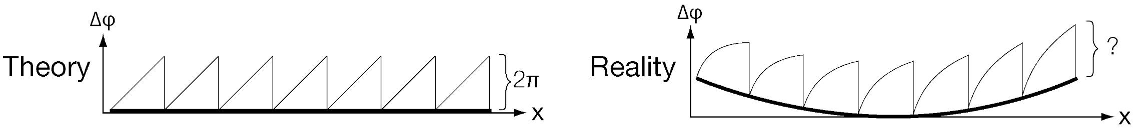

Figure 7.2.: **Intended and real phase modulations** if the SLM has an uneven surface or is not calibrated adequately.

perfectly flat, which adds an additional optical path difference in the order of the wavelength between different pixels. The applied phase modulations to an incoming plane and linearly polarized wave can thus differ dramatically in reality from the intended theoretical phase modulation as illustrated in Fig. 7.2. Furthermore it is crucial to know which displayed gray-value corresponds to a 2π phase shift to calculate the far-field diffraction pattern of the modulated wave front. In the following, experimental procedures to characterize and calibrate an SLM prior to its application for beam shaping are outlined and the results are presented. Two different phase-only SLMs were tested for Bessel beam generation in this thesis, a Holoeye Pluto (Holoeye, Berlin) and a Hamamatsu X10468-01.

7.1.1. Linearity Calibration

The SLM is addressed with a rectangular grating and the resulting intensity of the zero and first order diffraction spots are recorded. Both the base value n and the grating height m (see Fig. 7.3 below)are stepwise increased and the diffraction intensities are measured again for each height. The result is an $m \times n$ matrix containing the relative intensity in the first order diffraction spots

$$I_{rel} = \frac{(I_{-1} + I_{+1})/2}{I_{-1} + I_0 + I_{+1}}.$$

Alternatively, the zero order diffraction intensity can also be analyzed. Higher order diffraction is neglected here. At a grating height $m_{2\pi}$ which corresponds to a phase change of 2π the first diffraction order is expected to become zero, independent of the base value n. Experimentally measured matrices for both SLMs are displayed in Figs. 7.4 and 7.5. The 2π phase shift can also be found from this data as the grating height at which the first diffraction orders disappear. It is highlighted by a yellow dashed line.

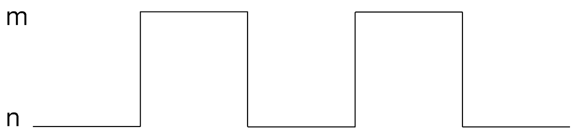

Figure 7.3.: **Rectangular grating** with base value n and height m.

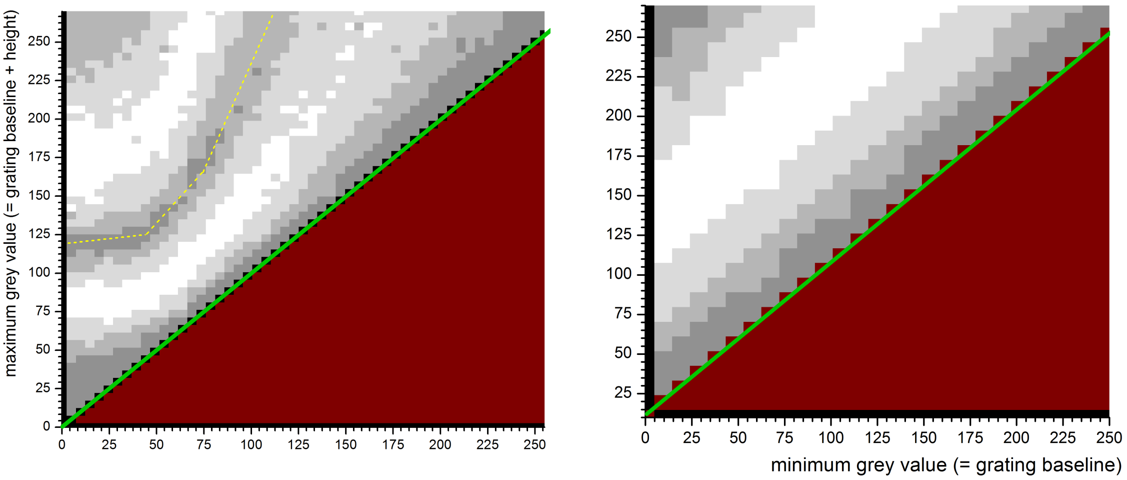

Figure 7.4.: **The linearity of the Holoeye SLM** was characterized by the intensity of the first order diffraction spots upon display of a rectangular grating with changing height. *Left*: default look-up-table. *Right*: corrected look-up table. Axes are identical on both matrices. The green line corresponds to the grating baseline and the yellow dashed line to the value of 2π. Both graphs have identical axes. The visible "blocks" results from the increment with which the grating height was varied and was smaller on the left.

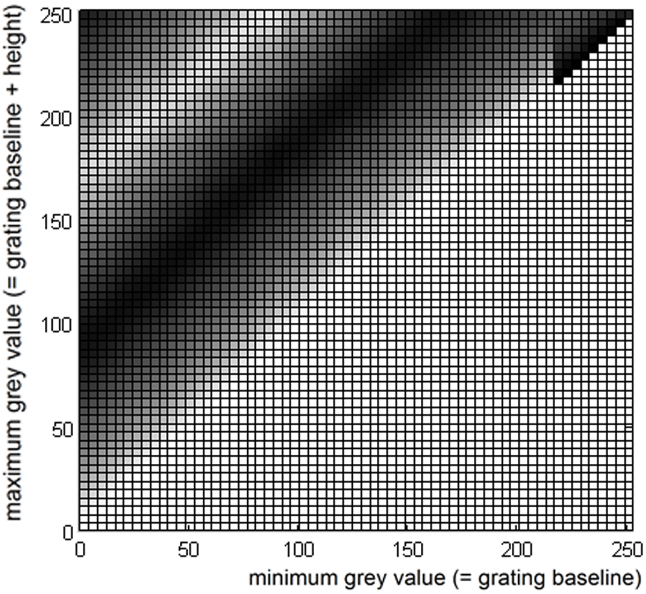

Figure 7.5.: **The linearity of the Hamamatsu SLM** was characterized by the intensity of the zero order diffraction spots. This measurement was provided by A. Jost. The darker corner is probably a measurement error.

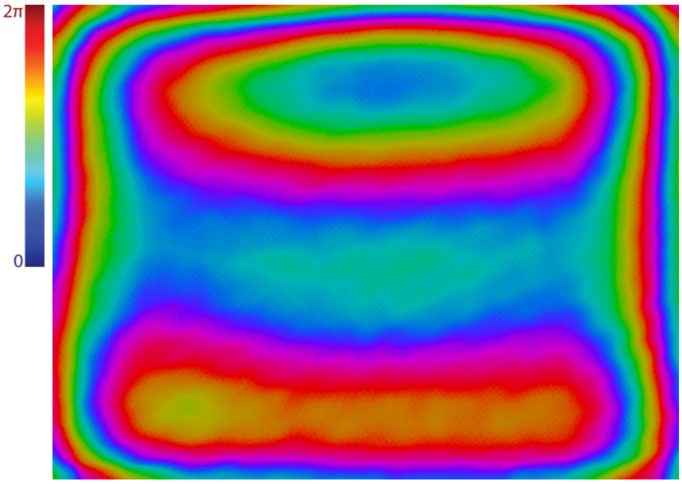

Figure 7.6.: **Phase compensation map** to account for the surface of the SLM.

7.1.2. Surface Calibration

To correct for manufacturing inaccuracies of the SLM flatness, a compensation map which evens out the phase offset can be added to all displayed gray-value images. The SLM surface is typically an astigmatic, slightly focussing, but smooth surface. Betzig et al. [136] displayed blazed gratings on overlapping sub-apertures of the SLM and compared the location of the resulting diffraction spot in an image plane to a reference to create a slope map. (This concept is very similar to the principle of a Hartmann-Shack-sensor.)
Another possibility is to fit a Taylor expansion to the SLM surface

$$f(x, y) = a + bx + cy + dxy + ex^2 + f^2y + ...$$

. The parameters a, b, c, d, e, f are iteratively optimized in a feedback-loop. During each iteration, a new $f(x, y)$ is created and displayed on the SLM. In an image plane, the resulting focussed spot is imaged with a webcam and its intensity evaluated. The *Strehl ratio* is a common measure of the quality of optical image formation. Here, a simplified Strehl ratio is used as a quality factor. The intensity distribution of the focussed spot is fitted with a 2D Gaussian curve and the height of the Gaussian curve over the image background is maximized. A resulting compensation map is shown in Figure 7.6.

7.1.3. Conclusion

Both SLMs are suitable for Bessel beam generation. Although the Hamamatsu SLM has lower resolution, we achieved a better linearity and a good surface flatness compensation. Furthermore, measurements by Dr. Martin Kielhorn suggest that the Holoeye SLM has a considerable phase noise which increases at higher gray value [personal communication]. All following experiments were conducted with the Hamamatsu SLM.

7.2. Engineering an Achromatic Bessel Beam

Most of this section including figures has been previously published in [3][1].

7.2.1. Bessel Beam Generation

The motivation of this Chapter was to produce a Bessel beam illumination for multicolour and broad-spectrum imaging applications such as OCT. Several approaches for generating Bessel beams have been mentioned in Section 3.5, however they are not straightforward for applications with a broad wavelength range or multicolour illumination. General drawbacks of axicons are chromatic problems for broadband light and the high manufacturing requirements to achieve the high angles required for high lateral resolution. With a diffractive element in the image plane, the radius of the ring pupil function will change with λ due to wavelength-dependent diffraction, thus a narrow annular aperture as a spatial filter would not be suited. Furthermore the different diffraction orders for different λ can overlap.

It is desirable to use the conjugate as opposed to the Fourier plane to maintain the image plane relation, minimize chromatic aberrations on the Bessel beam and make the illumination point spread function wavelength-independent. In order to generate a multicolour Bessel beam with a wavelength-independent profile over a broad λ-range, the pupil function is allowed to vary. To avoid superposition of different diffraction orders due to dispersion, a good separation between them is necessary. An an iterative Fourier transformation algorithm was designed based on these constraints with the goal to find a suitable SLM phase pattern for a simple multicolour Bessel beam implementation.

7.2.2. Algorithm and Results

A first naïve approach was to simply maximize the integrated intensity in the ring illumination. A circular symmetric grating of triangular phase ripples produces a first diffraction order ring distribution in the Fourier plane to the SLM (see Fig. 7.8A). However, this ring was observed to be effectively a double ring (Fig. 7.8B-C). When working with a monochromatic source, very precise alignment of an annular mask in the ring plane could be used to block one of the rings, similar to the approach in [29], however for a broadband source this solution is not applicable.

To seek an SLM phase pattern suitable for a broad light spectrum a custom IFTA was written. The goal function is an annular illumination of uniform phase on the ring with an area of zero intensity around it (see Fig. 7.9A). In the physical setup this corresponds to a wide ring aperture in a baffle. Due to dispersion, the radius of the ring scales with the wavelength of the light source and will change during

---

[1] This manuscript was published under the Creative Commons Attribution (CC BY) license and no permission for reprinting it here is required.
Prof. R. Heintzmann, Dr. K.Wicker and M. Walde conceived and designed the experiments. M. Walde and A. Jost built the optical setup, performed measurements. M. Walde wrote the manuscript.

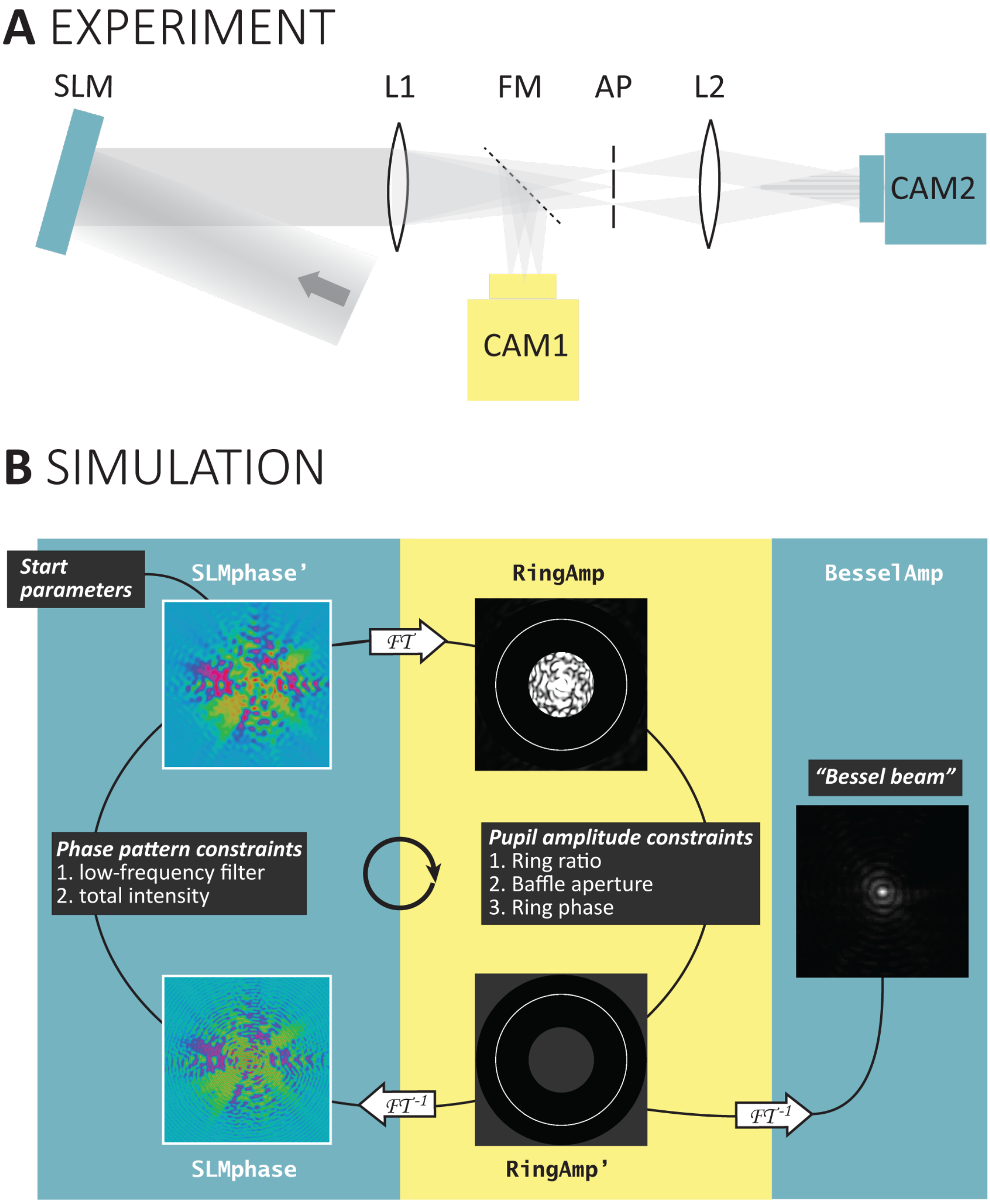

Figure 7.7.: **Schematic summary of the setup and algorithm**. *A*: A collimated beam is reflected by the spatial light modulator (SLM). The light is focused to a ring by lens L1. A flip mirror (FM) allows for observation of this ring on a CCD camera (CAM1). Undesired (zero diffraction order) light is blocked by a ring aperture (AP). Behind lens L2 the resulting interference pattern of the Bessel beam can be observed on camera CAM2. *B*: Starting from a given set of parameters, the algorithm jumps back and forth between the planes of the SLM phase pattern (blue) and the ring pupil function (yellow). In both planes certain constraints are applied. At each iteration the error to a desired goal function is evaluated. Function outputs are the final phase pattern (for the SLM) and simulated intensity distribution of the Bessel beam.

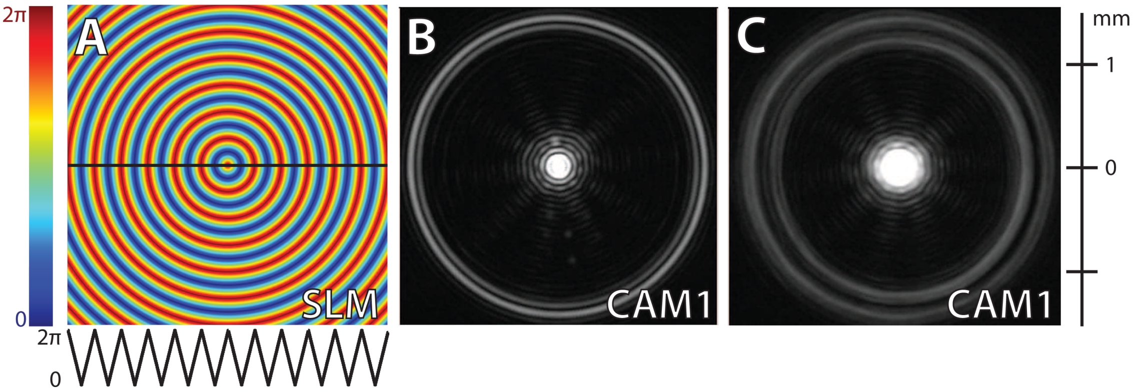

Figure 7.8.: **The double ring**. *A:* For monochromatic light and a circular symmetric grating of triangular phase on the SLM, we observed such double rings in the front focal plane of L1. A precisely aligned annular mask in the ring plane could be used to block one of the rings, which is however not applicable when working with a broadband source. *B:* in focus. *C:* slight defocus. The images were intentionally overexposed to highlight the rings.

wavelength tuning (Fig. 7.9C). This is exemplified by a red and green ring illumination and corresponding Bessel beam in Fig. 7.11A-B. The aperture on the baffle must thus be much wider than the ring itself. Furthermore, it greatly facilitates alignment to have a dark zone around the ring. Higher diffraction order light can be efficiently blocked even if the aperture is slightly misaligned (Fig. 7.9B). In the baffle zone (light grey areas in Fig. 7.9), the algorithm has the freedom to allow light intensity (in the experimental setup, this corresponds to light blocked by the aperture).

Fig. 7.7B summarizes the basic steps of the algorithm. As start values, a Gaussian illumination distribution, a constant phase distribution and desired parameters of the goal function (such as the ratio of intensity in the ring as compared to total intensity in Fourier plane, and the desired size of the ring are defined. Furthermore, a Boolean mask called `Baffle` is applied. This corresponds to the annular aperture in the physical setup (black areas in Fig. 7.9). At each iteration, the resulting complex amplitude `RingAmp` in the ring plane is calculated and amplitude constraints are applied:

1. The intensity in the ring (as percentage of the total intensity) is set equal to the pre-defined ratio. We achieved good results for 0.1.
2. The `Baffle` function is applied: The amplitude outside the ring but within the aperture area is forced to 0.
3. The phase along the ring is forced to 0.

The variable `RingAmp` which now carries these constraints is denoted here as `RingAmp'`. It represents the ideal result. The error of `RingAmp` compared to `RingAmp'` as the sum of absolute squares of deviations in each pixel is calculated and will be minimized through the iterative process. The complex amplitude `RingAmp'` is backpropagated to the SLM plane and `SLMphase` is retrieved by the Matlab `phase` function

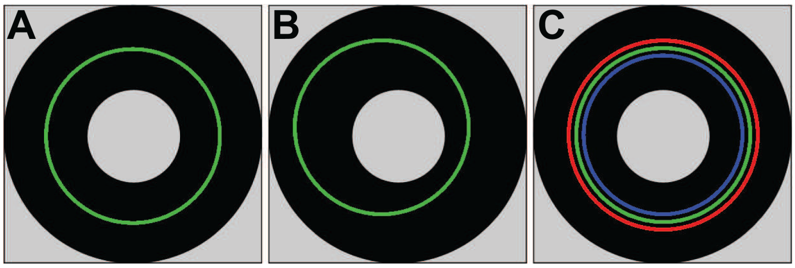

Figure 7.9.: *A:* **Goal function** of our IFTA is an annular illumination (green) of uniform phase on the ring with a zone of zero intensity (black) around it. Both undiffracted and higher order diffraction light is blocked by a circular baffle in the experimental setup (grey). *B:* The wide ring aperture around the ring illumination allows for small misalignments. *C:* Dispersion effects in the ring plane occur for polychromatic light.

which returns phase angles, in radians, of a complex image. Intensity values at the SLM plane are forced to a predefined illumination intensity and a phase constraint is also applied: A low-frequency filter prevents the algorithm from optimizing for patterns with high-frequency content to reduce higher-order diffraction. Then, a new Fourier Transformation is performed and `RingAmp` is calculated and constrained. The process is iterated typically 5000 times, each iteration leading to a smaller error criterium.
The associated MATLAB code can be found in the Appendix D on page 109ff. The script `MyBesselIFTA` contains the optimization rountine to find a suitable phase pattern for shaping a Bessel beam with an SLM. `Bessel_video_import` shows how the acquired raw video data of the resulting Bessel beams was processed.

An inverse scale relation exists between the radius of the ring and the radii of the Bessel beam maxima, since they are connected by a Fourier transform. Here, the final ring diameter ($\rho = 4\ mm$) was adjusted to match the camera sensor size and translation stage range. The illumination incident upon the SLM was simulated as a Gaussian distribution with $\sigma = 268$ pxl. The final phase pattern is shown in Figure 7.10 Fig. 7.10A–B. The final error was $7 \cdot 10^{-9}$.

Addressing the SLM with the resulting optimized `SLMphase'` pattern from the IFTA simulation, yielded the interference patterns presented in Fig. 7.11 in the BFP of *L1* (ring, Fig. 7.11A) and behind *L2* (Bessel beam, Fig. 7.11B–D). Note that the resulting rings are not anymore double rings. The light concentration in the ring (as percentage of the light intensity on the SLM) was measured to be 8.9% which is in good agreement with the algorithm input parameter of 10%. Higher light concentrations can be chosen if the light source is not strong enough. To demonstrate the effect of a broader wavelength spectrum, as green and red laser were used. While the rings in the BFP show dispersion (Fig. 7.11A), the resulting Bessel beams overlap well. A cross-section perpendicular to the optical axis and a corresponding radial intensity profile are shown in Fig. 7.11B+C. The extended focus of the central maximum can be seen in Fig. 7.11D.

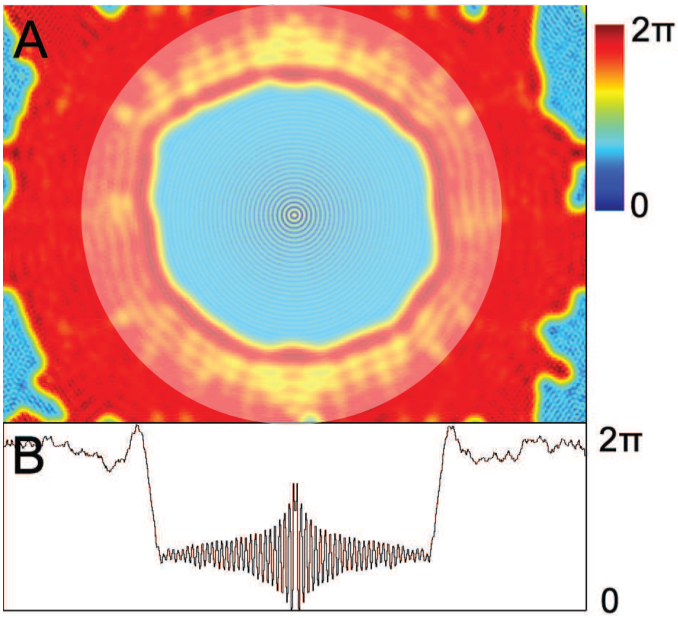

Figure 7.10.: **Final phase pattern**. After execution of the IFTA we displayed this *A* 800x600 periodic pattern on the SLM to modulate the incoming plane wave. The size of the beam incident on the SLM ist indicated by the superimposed semi-transparent white circle. *B* Cross-section through the center of A.

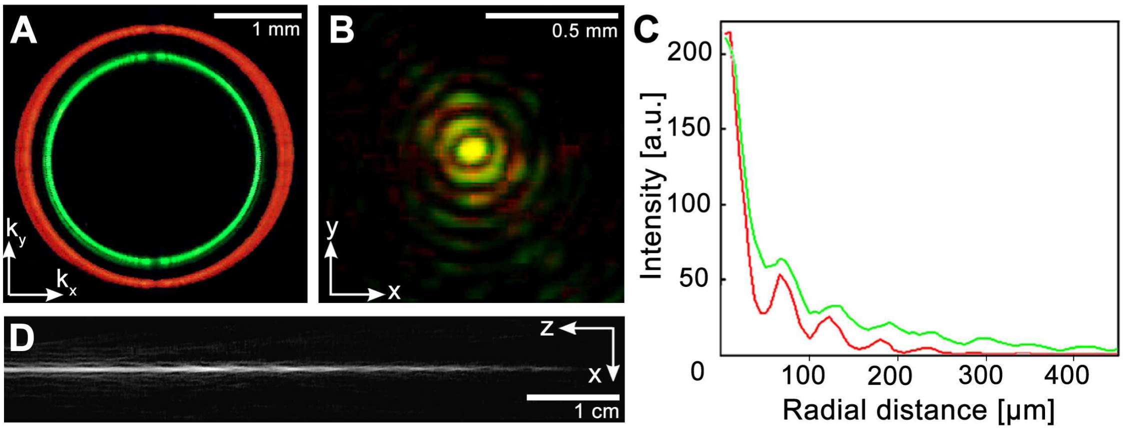

Figure 7.11.: **Experimental results**. *A:* Dispersion effects occur in the intermediate ring plane upon illumination with a red & green laser. Zero order diffraction is blocked by a baffle. *B:* Overlap of achromatic Bessel beams shown for red and green illumination. *C:* Radial profiles of red & green beams shown in B.*D:* Extended focus performance.

7.3. Discussion

It was shown that a phase-only spatial light modulator and an iterative Fourier Transformation algorithm can be used to create a multicolour Bessel beam. As a goal pupil function an annular light distribution with a sufficiently wide dark area around it was designed to avoid superposition of different diffraction orders due to dispersion. The 2D Fourier transformation of such a ring pupil function yields a Bessel beam.

The SLM was used to alter the phase distribution of an incoming plane wave with a Gaussian intensity profile. The phase pattern displayed on the SLM was determined by means of a custom-written IFTA. It has been shown that the resulting phase pattern did indeed yield the desired ring illumination and extended focus Bessel beam.

In principle one could have also searched for a purely radial solution, that is a phase modulation of the type $\varphi(r)$ by the algorithm instead of $\varphi(x, y)$. However, the phases of the incoming light are modulated by means of a phase-only SLM which has a discrete number of pixels arranged in a square grid pattern without radial symmetry. This phase image $\varphi(x, y)$ is optimized during each iteration. It is not immediately clear, whether allowing the algorithm to break the symmetry might allow more freedom.

Because the SLM and the Bessel beam are in conjugate planes, this approach is applicable to broadband applications. Constraints were designed such that a sufficiently sized area of zero intensity around the ring illumination exists. This allows for a dispersion in the intermediate ring plane as well as little misalignment. A wide ring aperture in the mechanical baffle is sufficient to spatially filter undesired zero- and higher-order diffraction light.

In contrast to previous work on achromatic Bessel beams by Leach et al. [137], no chromatic compensation techniques (such as a grating or prism) are required in this setup due to the image plane-to-image plane relation of the SLM and the Bessel beam center.

One major drawback of Bessel beams is that the central lobe contains only a small part of the total intensity, while the remaining intensity is in the ring system around the central lobe from where it is continuously transported to the beam center [25]. Depending on the application, this can deteriorate image contrast.

7.4. Bessel Illumination and Image Inversion Interferometry

As mentioned above, one major drawback of Bessel beams is the ring system around the central lobe which contains a large part of the total energy. This can be utilized to suppress image depth degradation from shadowing effects behind highly absorbing or scattering sample features and create a "self-reconstructing" effect. On the other hand, the signal to noise ratio in the focal region is significantly lowered and the lateral resolution for depths distant from the detection confocal position [138] is deteriorated.

Image inversion interferometry has previously only been demonstrated for incoherent detection. In this Section, its applicability to coherent scattering with Bessel illumination is investigated.

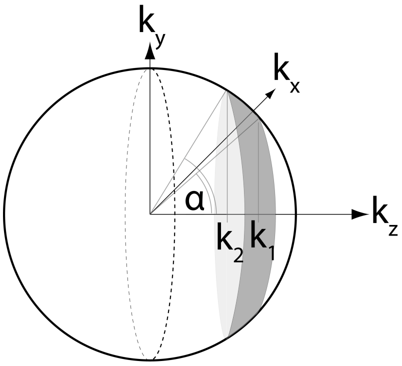

Figure 7.12.: Bessel illumination corresponds to a ring on the Ewald sphere

Scattering & Normal Detection

The illumination amplitude distribution created by a Bessel beam shall be denoted by $B(\mathbf{r})$. Its Fourier transform is $\tilde{B}(\mathbf{k})$. The k-vectors which form the beam corresponds to a ring on the Ewald sphere (see Fig. 7.12 and Appendix A.2). The incident light is scattered by the sample $\eta(\mathbf{r}-\mathbf{d})$ (with sample scanning vector $\mathbf{d}$), but only scattered waves within the aperture of the detection lens will contribute to the image. As shown in section 2.7.3, the resulting amplitude transfer function forms a "cap" on the Ewald sphere. The amplitude in an image plane of the optical system is a convolution of the APSF with the collected scattered field

$$E_O(\mathbf{r}) = [\eta(\mathbf{r}-\mathbf{d}) \cdot B(\mathbf{r})] \otimes \mathrm{APSF}(\mathbf{r}). \tag{7.1}$$

Interference with Reference Wave

The detected scattered light is coherently superimposed by a reference wave, which is also a Bessel beam. The reference mirror position is defined as $z = 0$.

$$\begin{aligned} E_{\mathrm{OCT}}(\mathbf{r}) &= E_O(\mathbf{r}) + E_R(\mathbf{r}) \\ &= E_O(\mathbf{r}) + B(\mathbf{r}) \otimes \mathrm{APSF}(\mathbf{r}) \\ &= [\eta(\mathbf{r}-\mathbf{d}) \cdot B(\mathbf{r})] \otimes \mathrm{APSF}(\mathbf{r}) + B(\mathbf{r}) \otimes \mathrm{APSF}(\mathbf{r}) \\ &= [\{\eta(\mathbf{r}-\mathbf{d}) + 1\} \cdot B(\mathbf{r})] \otimes \mathrm{APSF}(\mathbf{r}) \end{aligned} \tag{7.2}$$

Image Inversion Interferometry

Interference in the constructive (+) and destructive (-) channel of the UZI (see Eq. 3.4) is described by

$$\mathrm{UZI}_{+/-}(\mathbf{d}) = \int\limits_{R^3} \left| E_{\mathrm{OCT}}(\mathbf{r}) \pm E_{\mathrm{OCT}}(\hat{\mathbf{r}}) \right|^2_{z=0} \mathrm{d}x\mathrm{d}y, \tag{7.3}$$

where $\hat{\mathbf{r}} = (-x, -y, z)$.
Inserting 7.3 in 3.7 yields

$$\begin{aligned} \mathrm{UZI}_+ - \mathrm{UZI}_-(\mathbf{d}) &= \int 4\Re \left(E_{\mathrm{OCT}}(\mathbf{r}) \cdot E^*_{\mathrm{OCT}}(\hat{\mathbf{r}}) \right)\big|_{z=0} \mathrm{d}x\mathrm{d}y & (7.4) \\ &=: 4\Re \left\{ \mathfrak{G}(\mathbf{r}) \right\}. & (7.5) \end{aligned}$$

The meaning of

$$\mathfrak{G}(\mathbf{r}) = \int \left[E_{\mathrm{OCT}}(\mathbf{r}) \cdot E^*_{\mathrm{OCT}}(\hat{\mathbf{r}}) \right]\big|_{z=0} \mathrm{d}x\mathrm{d}y$$

is analysed in Appendix B on page 103. Using the prior knowledge that amplitude transfer function, the Bessel ring and the Delta function are rotationally symmetric and the assumption that the ATF is 1 everywhere on the cap and fully supports the Bessel ring, the integration terms can be separated and simplified to

$$\begin{aligned} \mathfrak{G}(\mathbf{r}) = &\int \left[\left\{ \tilde{\eta}(\mathbf{k})\ e^{\mathrm{i}\ \mathbf{kd}} \otimes \tilde{B}(\mathbf{k}) \right\} \cdot \left\{ \tilde{\eta}^*(\hat{\mathbf{k}})\ e^{\mathrm{i}\ \hat{\mathbf{k}}\mathbf{d}} \otimes \tilde{B}(\mathbf{k}) \right\} \right] \cdot \mathrm{ATF}(\mathbf{k})\ \mathrm{d}\mathbf{k} \\ &+ \int \tilde{B}^2(\mathbf{k})\ \mathrm{d}\mathbf{k} \\ &+ \int \left\{ \tilde{\eta}^*(\hat{\mathbf{k}})\ e^{\mathrm{i}\ \hat{\mathbf{k}}\mathbf{d}} \otimes \tilde{B}(\mathbf{k}) \right\} \cdot \tilde{B}(\mathbf{k})\ \mathrm{d}\mathbf{k} \\ &+ \int \left\{ \tilde{\eta}(\mathbf{k})\ e^{\mathrm{i}\ \mathbf{kd}} \otimes \tilde{B}(\mathbf{k}) \right\} \cdot \tilde{B}(\mathbf{k})\ \mathrm{d}\mathbf{k}. \end{aligned}$$

In contrast to other coherent imaging methods it does not appear straightforward to isolate the sample information from this expression. On the contrary, they always appear in convolution with the Bessel ring. If we consider the concept of convolution

as painting one function with the other function as a brush, this means that the sample frequencies will be smeared along the Bessel ring in Fourier space.
Hence it could **not** be shown, that the combination of the image inversion interferometer and a Bessel illumination leads an improved resolution or contrast for coherent backscattering imaging.

8
Holoscopic Recording

Instead of scanning the scattering sample with a Bessel beam, full-field recording would offer higher acquisition speed. To this end, OCT can be combined with reconstruction methods from digital holography. Full-field holograms are recorded at many wavelengths with a tunable laser and a very fast sCMOS camera, thus eliminating the need for scanning. For this holographic approach to extended focus OCT, a custom optical system was built, which is shown and explained in this Chapter. A full list of parts is given on p. 38 in Section 3.9. An operation manual for future users is attached in Appendix C.

The depth information is then obtained from the spectral dependence of the recorded holograms. An off-axis-configuration allows for separation of auto-correlation and cross-correlation terms in the recorded interference images. The reconstruction of the holograms is explained in the following Chapter 9 and first results are shown.

8.1. The Holoscopy Platform

The optical setup is based on a Mach-Zehnder type interferometer in which one arm is slightly tilted. This off-axis design was chosen to separate the auto- (AC) and cross-correlation (CC) terms in the holograms. Full-field holograms are recorded at many different wavelength with low coherence light: Typically 1800 holograms are recorded at 2000 fps between 790 and 880 nm with a wavelength separation of $\Delta\lambda = 0.1$ nm. The sample is illuminated with an extended collimated beam. Backscattered (and reflected) light within the coherence length of the virtual reference plane in the sample will interfere with the reference wave in the detection plane to form the hologram. Scattering contributions outside this range are removed by coherence gating.

A polarizing beam splitter, quarter-wave plate and a linear polarizer are used to suppress artifacts from unwanted reflections. The camera is mounted on a 45°tilted mount to make best use of the sensor area.

8.1.1. Alignment

Due to the low coherence length of the light source, a precise alignment of sample and reference arm is required. The path length of the reference arm can be adjusted with mirror M2 that is mounted on a z-translation stage. Lens L3 is mounted on a flip-mount and can be inserted to create an image plane on the camera and see the focal plane of the objective.

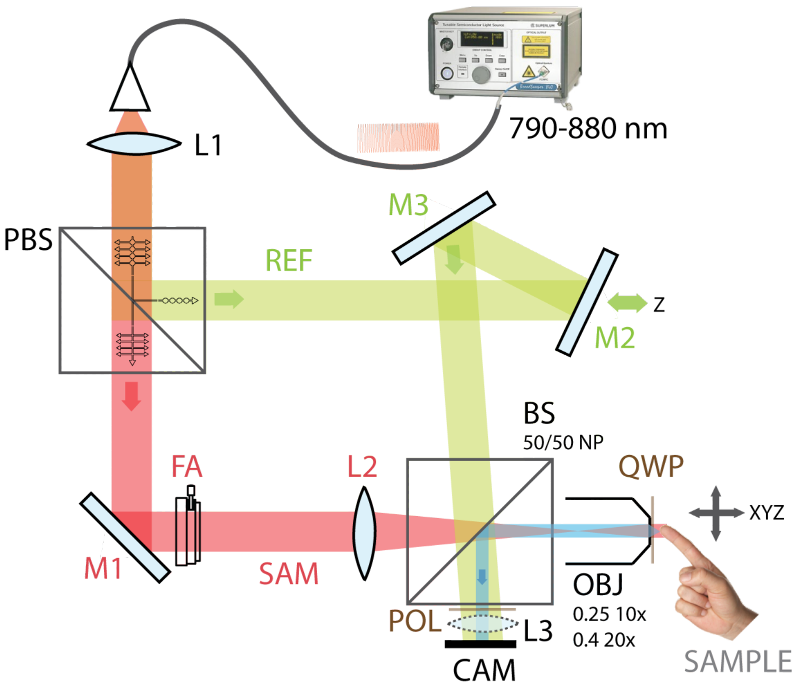

Figure 8.1.: **Experimental setup for hologram recording**. REF reference arm (red); SAM sample illumation arm (red); L1, L2, L3 lenses (L3 is on a flip-mount and not used for hologram acquisition); M1, M2, M3 silver mirrors; POL linear polarizer; FA field aperture; PBS polarizing cube beam splitter; BS non-polarizing cube beam splitter; QWP quarter-wave plate; CAM camera; OBJ microscopy; objective.

The off-axis configuration introduces a separation of the CC and AC terms in Fourier space. It is crucial that the CC areas stay within the resolvable frequency range of the camera sensor, but are well enough separated from the larger AC area (see Fig. 8.3B). This can be adjusted with mirrors M2 and M3 and the field aperture FA. A custom-written Matlab script supports manual alignment by displaying both the real space and Fourier space camera image side-by-side in a high-contract colormap (Fig. 8.2).

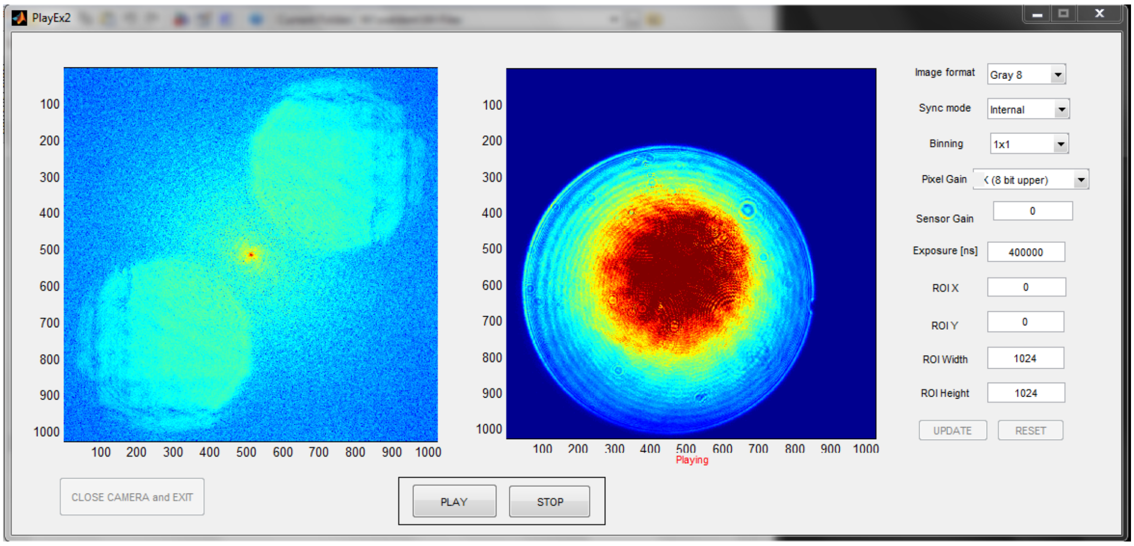

Image format: Gray 8
Sync mode: Internal
Binning: 1x1
Pixel Gain: (8 bit upper)
Sensor Gain: 0
Exposure [ns]: 400000
ROI X: 0
ROI Y: 0
ROI Width: 1024
ROI Height: 1024

Figure 8.2.: **The graphical user interface of the alignment support function.** *Left*: FFT of the camera image, *middle*: camera image, *right*: parameters.

8.2. Practical Considerations and Limitations

8.2.1. Acquisition Speed

Recording 1800 holograms at 1 MP resolution requires some memory. Typically 1-2 GB of data are acquired for each hologram sequence within 0.9 sec recording time. Where appropriate, a slightly reduced region of interest was recorded. Subsequently, it takes approximately 10 min to download this data from the camera's on-board memory. Recording the **holograms** alone is however not sufficient for the reconstruction. Another sequence of the **reference** wave field is required. A set of **dark images** is necessary, too, but does not need to be recorded anew each time. It is furthermore desirable to record a sequence of the **sample** wave field alone. Naturally, each of these data sets with produce another 1-2 GB of data to be transferred and despite the very rapid laser sweep, the overall acquisition time can hence become quite long.

To achieve faster acquisition, perhaps even series of holograms, a larger on-board memory and image pre-processing on the graphics processing unit of the camera could be used. For the purpose of this study, this limitation is admissible.

8.2.2. Sampling

A scattering sample of interest is illuminated with a plane wave under straight illumination. For a sample with sparse point scatterers (Born approximation), the back-scattered light is assumed to be a spherical wave for each scatterer. The different positions of the scatterers translate into different angles in the back focal plane (BFP) of the microscope objective. Thus, parallel waves under a limited range of angles fall onto the camera sensor and are interfered with the reference wave (within the coherence gate). The resulting interference fringe separation follows from Eq. 2.6 on page 11.

$$d_f(\theta) = \frac{\lambda}{\sin\theta}\,.$$

For a sufficient sampling rate according to the *Nyquist–Shannon theorem*, the pixel spacing should be at least 2 (or even better 3) pixels per interference fringe.

$$d_{\text{pxl}} = \frac{d_f}{2} = \frac{\lambda}{2 \cdot \sin\theta}$$

The IDT NX4-S2 high-speed camera has a pixel spacing of $d_{\text{pxl}} = 13.68\ \mu\text{m}$ and a sensor size of $(13.9\ \text{mm})^2$.

Interference fringe separation increases with wavelength λ and decreases with angle θ. This imposes a limit on the biggest resolvable angle θ at the shortest λ of 790 nm

$$\sin\theta = \frac{790\ \text{nm}}{2 \cdot 13.68\ \mu\text{m}}.$$

If the θ-plane is parallel to one of the coordinates of the camera sensor edges the maximum angle is $\theta_{x,y} \approx \pm\ 1.65°$. If the camera is tilted by 45°, the corners of the sensor area can be filled and θ is increased by a factor $\sqrt{2}$ to

$$\theta_{\text{diag}} \approx \pm\ 2.33°.$$

8.2.3. Space-Bandwidth-Product and Field of View

The maximum achievable field of view in the off-axis geometry is limited by the image sensor size. In Fig. 8.3A a scenario for the maximum extent of AC and CC terms is illustrated. This scenario comes at the cost of a substantial overlap of these terms and requires other means of separating them (such as phase-stepping approaches). Maximally half the image sensor size (in each direction) is available for imaging the sample. This area measures

$$A_{\text{cam}} = \pi k_r^2\,. \tag{8.1}$$

The *space-bandwidth-product* (SBP) of the camera available for imaging the CC term is the ratio of the detection area A_{cam} to the area of one pixel d_{pxl}^2

$$\text{SBP}_{\text{cam}} = \frac{A_{\text{cam}}}{d_{\text{pxl}}^2}.$$

Within the Abbe sine condition, the SBP remains constant in the imaging process

$$\text{SBP}_{\text{cam}} \equiv \text{SBP}_{\text{sample}}.$$

We can imagine the sample plane to be subdivided by a pixel grid like the camera plane. The minimum resolvable distance d_{min} according to Abbe's resolution limit is listed for all available objectives in Table 3.2 on page 40. For the 10×/0.25 NA objective it is $d_{\text{min}} \approx 3.16\ \mu\text{m}$.

To image the smallest resolvable detail at appropriate sampling with full resolution and field of view (FOV), a pixel size of $d_{\text{samp}} = d_{\text{min}}/2 = 1.58\ \mu\text{m}$ over the entire

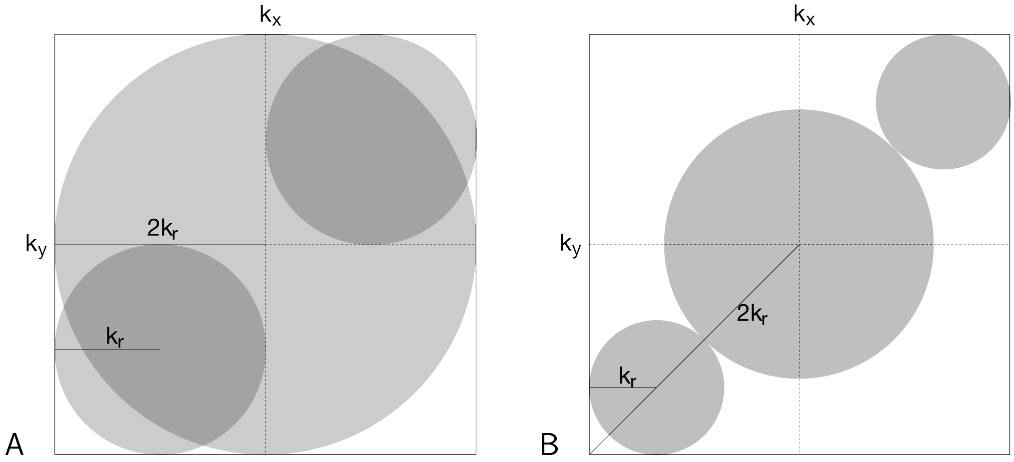

Figure 8.3.: **Bandwidth of auto-correlation (AC) and cross-correlation (CC) terms** on the Fourier transform of the camera image in an off-axis hologram recording setup. Due to the off-axis configuration, the CC terms have a spatial offset. The AC bandwidth is twice as wide as the CC bandwidth. *A:* Maximum bandwidth with substantial overlap of AC and CC terms. *B:* Clean spatial separation of AC and CC terms.

FOV area on the sample would be needed. Assuming a square pixel size, the maximum FOV area that can be captured is

$$\mathrm{FOV}_{\mathrm{max}} = \mathrm{SBP}_{\mathrm{sample}} \cdot d_{\mathrm{samp}}^2. \tag{8.2}$$

By combining Eqs. 8.1 and 8.2, its diameter $\varnothing_{\mathrm{FOV}}$ of the field can be simply expressed as

$$\varnothing_{\mathrm{FOV}} = \frac{d_{\mathrm{min}}}{d_{\mathrm{pxl}}}\, k_r = \frac{1.58\ \mu\mathrm{m}}{13.68\ \mu\mathrm{m}}\, \frac{13.9}{2}\ \mathrm{mm} \approx \mathbf{803}\ \mu\mathrm{m}$$

For practical imaging applications a larger FOV can be desirable. If that is the case, a larger sensor, smaller pixel size or an inline-holography configuration can be chosen instead.

8.2.4. Geometric Limitations on the Field of View

Let us consider an imaging geometry as shown in Figure 8.4. Depending on the radius R of the back focal plane and the size d_{max} of the camera sensor (CAM), only a limited area (field of view) πd_{FOV}^2 of the object can be imaged.
The maximum radius of the image on the camera is given by

$$d_{\mathrm{max}} = R + d_m = R + s \cdot \tan\beta = R + \frac{s \cdot d_{\mathrm{FOV}}}{f_{\mathrm{obj}}}.$$

The size of the camera chip is (13.9 mm)^2. For the same 10×/0.25 NA objective as in the previous Section, the maximum Δ_{FOV} is thus

$$d_{\mathrm{FOV}} = \frac{d_{\mathrm{max}} - R}{s} \cdot f_{\mathrm{obj}} = \frac{(13.9/2 - 4.5)}{156} \cdot 18\ \mathrm{mm} \approx 282.7\ \mu\mathrm{m}$$

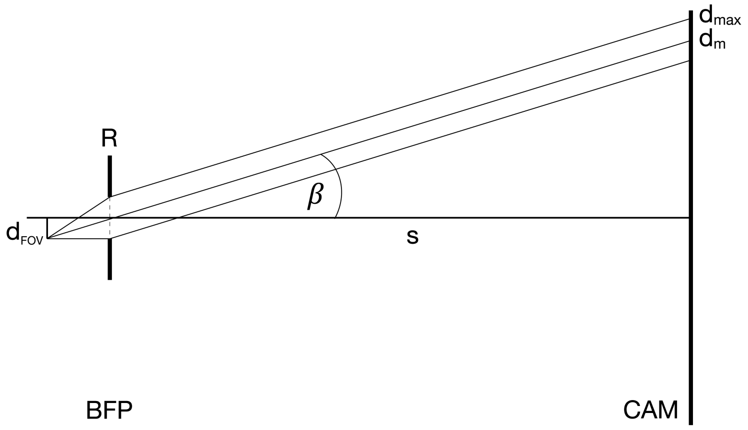

Figure 8.4.: **Geometric limitations.** Illustration of the outermost rays in the field of view that will pass the back focal plane (BFP) of the objective and hit the camera sensor (CAM).

and the diameter $\varnothing_{\text{obj}} = 2d_{\text{FOV}} \approx \mathbf{565.4}\ \mu\text{m}$.

Depending on the **recording mode**, different FOVs can be practically realized:

1. **On-axis configuration** (for $\beta = 1.65°$)

$$\begin{aligned} d_{\text{FOV,A}} &= f_{\text{obj}} \cdot \tan\beta \\ &= 18\ \text{mm} \cdot \tan 1.65° \approx 518.5\ \mu\text{m} \\ \varnothing_{\text{obj},A} &= 2d_{\text{FOV,A}} \approx \mathbf{1.04}\ \text{mm} \end{aligned}$$

2. **Off-axis configuration** As can be seen from Fig. 8.3B, it is practical to make the bandwidth of the AC and CC terms smaller than the maximum possible size shown in Fig. 8.3A (for instance, by use of a field aperture in the optical setup) to achieve a good spatial separation. This allows for an extraction of the CC terms in the hologram reconstruction.

   From the geometry shown in Fig. 8.3B it follows that:

$$k_{max} = \sqrt{2} \cdot 3k_r + k_r = k_r \left(1 + 3\sqrt{2}\right)$$

$$\begin{aligned} d_{\text{FOV,B}} &= d_{\text{FOV,A}} / \left(1 + 3\sqrt{2}\right) \\ &\approx 518.5\ \mu\text{m}/5.24 \approx 98.9\ \mu\text{m} \end{aligned}$$

$$\varnothing_{obj,B} = 2d_{\text{FOV,B}} \approx \mathbf{197.8}\ \mu\text{m}.$$

From these values it can be seen that while an off-axis configuration offers the advantage of a simple separation of CC and AC terms from a single hologram, it sacrifices a lot of the field of view size. For the purpose of this thesis, a small FOV is acceptable. An on-axis (also referred to as inline) configuration should however by kept in mind as a future alternative.

9
Holoscopic Reconstruction

An offline reconstruction algorithm separates the cross-correlation (CC) and auto-correlation (AC) terms in Fourier space. CC terms are windowed and extracted and shifted back to the origin, which reverses the angular offset caused by the off-axis recording setup. The thereby extracted amplitudes are then backpropagated to the back focal plane of the objective lens. In the following, the reconstruction procedure is explained in detail and possible alternatives are discussed. The Matlab script may be found in Appendix E.

9.1. Reconstruction Algorithm

Fig. 9.1 gives an overview over the steps of the hologram reconstruction algorithm. It can be divided into three stages: (1) Pre-processing of the raw data, (2) separation of the cross-correlation term from the acquired holograms and its backpropagation to the nominal back focal plane of the objective lens, (3) reconstruction of the emitted wave distribution in the sample. Stage (2) and (3) are based on the angular spectrum approach.

9.1.1. Pre-Processing

1. **Load holograms.**
   From the choice of convertible data formats (3.9.3), AVI format was chosen. It offers a comparably fast data transfer without quality loss due to compression. For each dataset, holograms are imported into Matlab as DIPimage (an object class defined by the DIPimage toolbox, similar to an array). The loaded DIPimage stacks are abbreviated as `AllHolo`: holograms; `AllRef`: reference arm; `AllSam`: sample arm and `AllDark`: dark images in Fig. 9.1 and the attached Matlab script. The last two stacks are optional and not always recorded). Each stack currently requires approximately 1.2 GB of memory and 5 min loading time.

2. **Remove pre-trigger frames & sub-sampling.**
   The BroadSweeper source sends a trigger at the beginning of each sweep which is used to initiate the image acquisition. (The detailed camera and source settings can also be found in the attached operation manual in Appendix C). As a visual control 2-3 pre-trigger frames are stored and have to be removed here. For a faster reconstruction it can be useful to reduce the number of holograms by increasing the wavelength sampling distance.

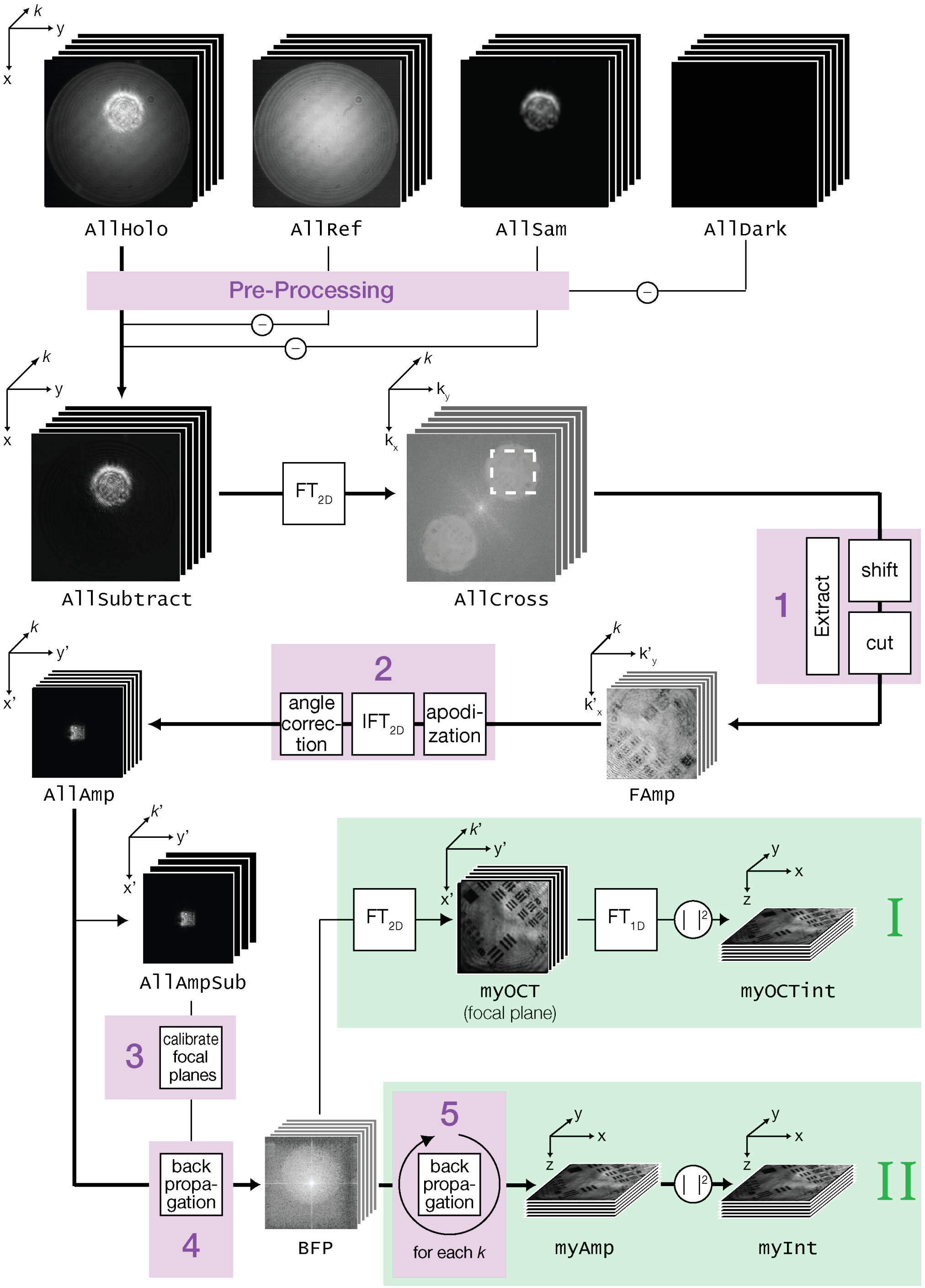

Figure 9.1.: **Reconstruction of acquired holoscopic data** was executed in a custom-written MATLAB routine. The main reconstruction steps are shown here. Data inputs are the acquired image stacks (`AllSam` and `AllDark` are optional) and outputs are reconstructed 3D amplitude and intensity images. A classic OCT reconstruction (I) is also simulated and compared to the holographic reconstruction approach (II). Purple numbers represent called sub-routines which perform the indicated operations: 1 `ExtractCrossCorrelation`, 2 `ApodizeHolo`, 3 `FindFocalPlane`, 4 `PropagateField`, 5 `ReconHolo` (calling `SimLens` and `PropagateField`).

3. **Remove offset.** If no dark images were acquired, the background is estimated from the offset in a dark region of the stacks. This procedure yields an array of values (one for each frame) which is subsequently subtracted from the image stacks.

4. **Normalization & Subtraction.**
   The reference images are subtracted from the holograms. This step significantly removes brightness fluctuations by the light source and reduces the strength of the AC terms in the Fourier transform of the holograms. A comparison of mean image intensities over all recorded wavelengths before and after subtraction of the references is shown in Fig. 9.2.

5. **Remove background pattern.**
   The camera has an inherent line pattern which can be extracted from the images and removed.

The pre-processed data sets (named `AllSubtract`) can be saved/loaded to continue processing from here.

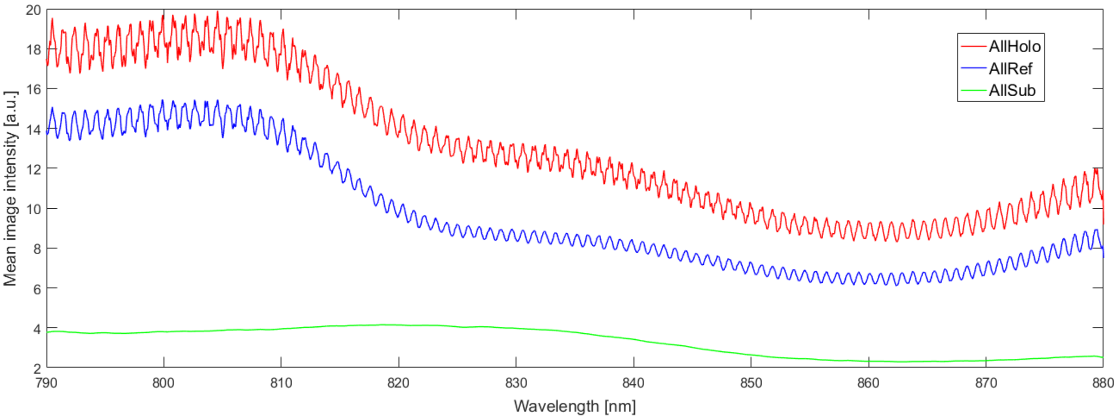

Figure 9.2.: **Intensity fluctuations from the light source** are significantly removed after subtraction of the references from the holograms and removal of the camera line pattern.

9.1.2. Separation and Backpropagation

1. **Extract the CC terms via 2D Fourier filtering**
   The zero-frequency position of the CC term changes with wavelength. A subroutine `ExtractCrossCorrelation.m` is called. Image regions which correspond to the CC terms are chosen manually for one wavelength and calculated accordingly for all others. From the distance of this region to the image center, a phase term `refphase`(k) is calculated. Multiplying `AllSubtract`(k) with this phase is similar to illuminating with the reference wave in analogue holography. In Fourier space, the phase multiplication causes a shift of the CC terms to the origin where they are cut out to obtain `myFAmp`(k). The change in FT image size influences the scaling of the real image and the pixelsize has to be adjusted.

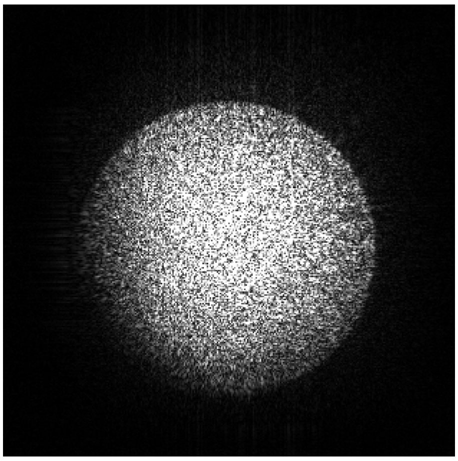

Figure 9.3.: Calibration of the propagation distance to the back focal plane of the objective lens can be done very precisely by focussing the holograms to a pupil.

2. **Apodize holograms**
   A subroutine `ApodizeHolo.m` is called. To avoid ringing effects in the Fourier transform due to sharp image edges, a Hann window can be applied. A 2D FT of the extracted CC terms in `myFAmp`(k) yields the complex wave field `AllAmp`(k). Small misaligments in the optical system can lead to an additional angle offset in `AllAmp`. An optional angle correction is also included in `ApodizeHolo.m`.

3. **Calibration of the focal planes**
   Before `AllAmp` can be backpropagated, the precise distance of the front and back focal plane of the objective lens to the camera plane has to be calibrated. This value can usually be re-used from previous reconstructions unless the optical setup has been altered or re-aligned.
   To reduce computing time, it is sufficient to call `FindFocalPlane.m` which propagates only a few or even only one wavelength back to a z-range from which the best focus can be selected.
   The BFP position is similarly calibrated with a function `FindBFPlane.m`. In the back focal plane a focused pupil becomes visible (shown in Figure 9.3). In this plane the real and conjugate CC terms can be distinguished, as the wave contributions of the latter do not form a pupil here.

4. Once the position of the BFP is known, the complex wave field `AllAmp`(λ) can be backpropagated with a propagator that is calculated in `PropagateField.m`. The resulting amplitude distribution is simply called `BFP`.

9.1.3. Reconstruction

Two different reconstruction routines have been tested and results will be shown and compared in Section 9.2.

OCT Reconstruction

In full-field OCT, the scattered light would be recorded in an image plane and after separation of the CC term an inverse FT over k yields the scattering potential. To simulate this, a 2D FT is applied to the `BFP` to create an image plane `OCTraw`. Next, a pixelwise 1D IFT along k is applied. The resulting amplitude `myOCT` distribution is proportional to the scattering potential. Its absolute square is the intensity `myOCTInt`.

Holographic Reconstruction

The holographic reconstruction is executed by the subroutine `ReconHolo3.m`.

1. The `BFP` is mapped onto the 3 vector components of the electric field vector (E_x, E_y, E_z) by `SimLens.m` in order to create a vectorial PSF. This means that for higher NA objectives, polarization effects can be accounted for.

2. The mapped `FPlane` is propagated to the sample plane with `PropagateField.m` which calculates the k_x, k_y, k_z components.
   All amplitude distributions are summed to `myAmp`(x, y, z) and the absolute squares are taken to form `myInt`(x, y, z). This is the slowest step of the reconstruction and has to be calculated for each wavelength.

`PropagateField.m` and `SimLens.m` are part of the `ElectricFields` toolbox written by Rainer Heintzmann for Matlab and CUDA. The CUDA platform allows for parallel computing on the graphics processing unit (GPU) and considerably speeds up the calculations.

9.2. Reconstructed Holograms

9.2.1. Test Samples

First measurements were taken from a negative USAF resolution target, which is very reflective.
Resolution targets have a series of horizontal and vertical lines that can be used to determine the lateral resolution. The resolution chart is composed of seven "groups" and each group consists of a set of six "elements" (three lines).
The absolute square of the sum of the backpropagated amplitudes (`myInt`) reconstructed by the holographic reconstruction is shown in an XY-slice in Fig. 9.4. On the left side of the image, the smallest group N°7 is visible. While the last two elements (#5 and #6) are blurred, #4 is just discernible and #3 is well separated. This corresponds to a lateral resolution of approximately 3 μm.

For a comparison of the reconstruction algorithms, scattering phantoms with 5 μm polystyrene beads as individual point scatterers were used. Only 180 holograms ($\Delta\lambda = 0.5$ nm) were used for this reconstruction. Stepping through the holographically reconstructed 3D intensity volume showed several beads in different focal positions. In Fig. 9.5A, the maximum projection of this volume along z is shown.

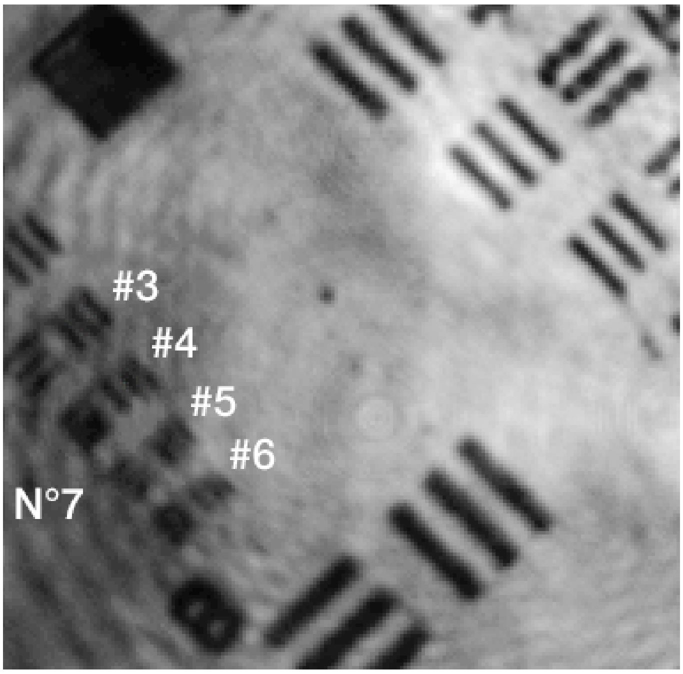

Figure 9.4.: **Reconstructed negative USAF target** with element #4 in group N°7 just discernible, which corresponds to a lateral resolution of approximately 3 μm.

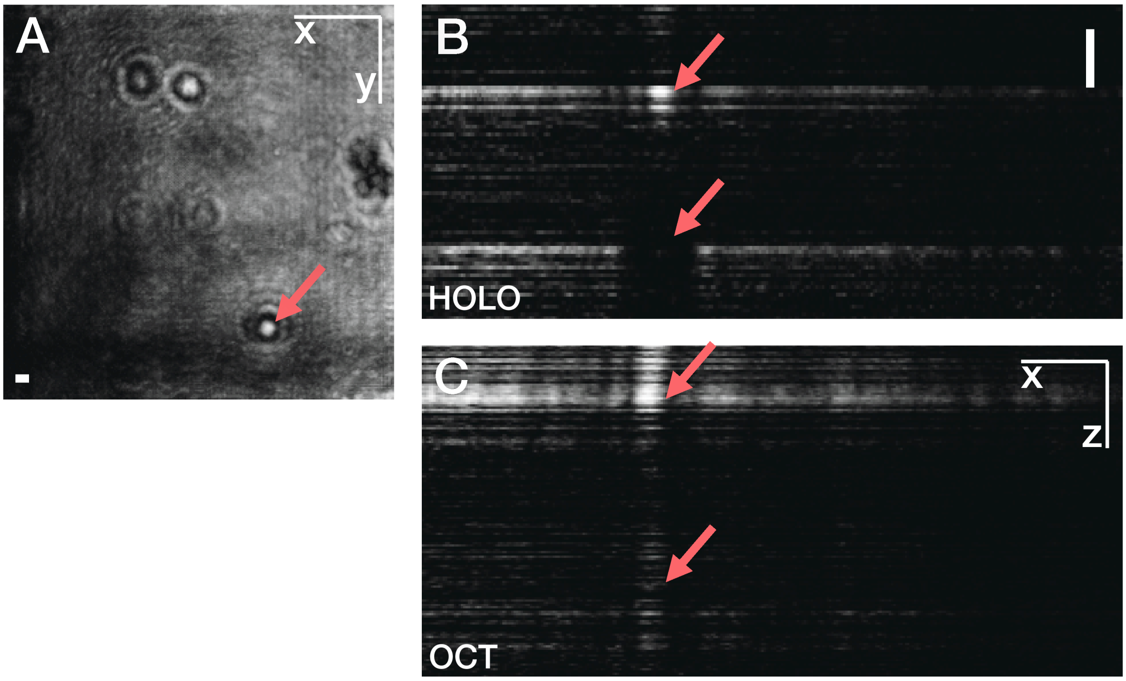

Figure 9.5.: **Reconstructed bead sample** for a comparison of both reconstructions. *A:* Maximum intensity projection with selected bead of the resulting intensity image stack (`myInt`) by holographic reconstruction . *B-C*: XZ cross-sections along the same bead shows a shadow in the holographic reconstruction (B) and a bright smear in the classic OCT reconstruction (C). Scale bars are 10 μm

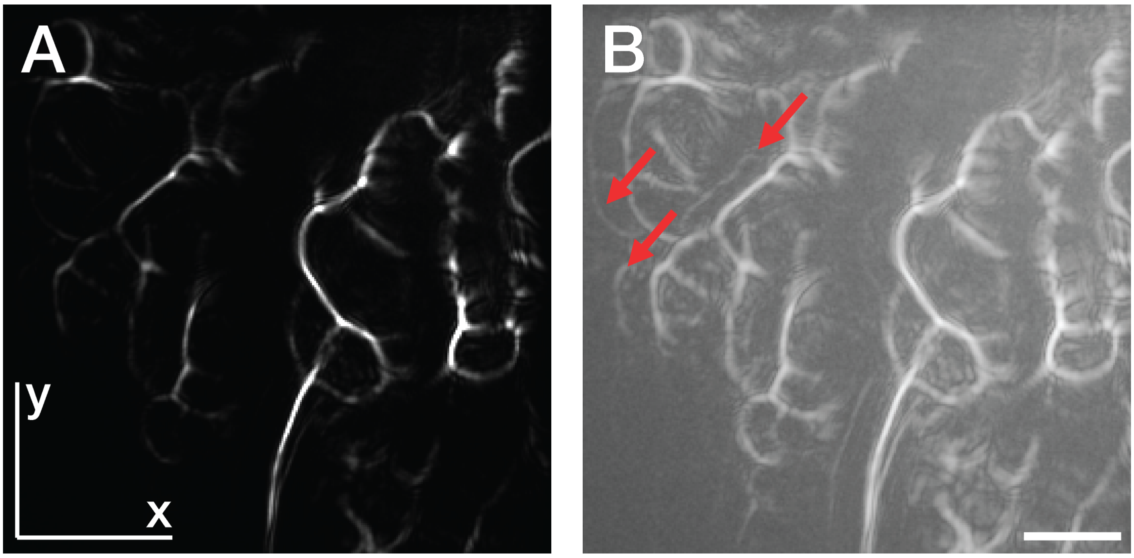

Figure 9.6.: **Grape cross-sections** from the holographic reconstruction are shown as XY intensity slices. *A:* Linear scale. *B:* On the logarithmically scaled version, image artifacts are visible. Scale bar is 50 μm

Figs. 9.5B and C show side by side XZ cross-sections through the reconstructed volume in the Y-plane one of the beads (arrow), reconstructed by the holographic and classical OCT approach, respectively. In the holographically reconstructed image (B) a dark shadow behind the bead is visible, while in the classical OCT reconstruction (C) the bead smears out along z.

9.2.2. Biological Samples

As a biological test sample, fresh cut grapes were used. At this resolution, their parenchyma cells should be visible. An intensity image slice of the holographic reconstruction is shown in Fig. 9.6A. The log-scaled version in Fig. 9.6B reveals that the reconstruction still suffers from severe image artifacts which might arise from ghost reflections in the optical setup or multiple scattering events that change the optical path length of the collected light.

9.3. Discussion

OCT has made a big impact on medical diagnostics since its introduction more than 20 years ago. In ophtalmology, subtypes of ablations of the retinal epithelium were discovered which could not be distinguished previously [19]. With holoscopic recording and reconstruction even higher spatial resolutions and faster image acquisition speed could potentially be achieved. The optical setup does not require lateral or axial scanning and could be miniaturized for clinical application. However, the results shown in the previous section have to be considered preliminary and leave potential for various enhancements.

The data transfer between camera and file server is currently quite slow, which is however only a technological limit. The fundamental limit of the acquisition speed of full-field holograms is the scattered signal from the sample. Currently 1800 holograms were recorded in 0.9 s, but with a faster camera this could be driven to video rate (30 full data sets in one second).

A related technological limitation is the amount of memory required to record and reconstruct the data. To speed up calculation, some of the calculations had been parallelized on the graphic card's GPU with CUDA. For calibration steps only hologram subsets were used. Unfortunately memory problems persisted and could not be entirely dissolved to date. Future work should therefore focus on improving the effciency of the reconstruction procedure. The reconstructions shown here only used a fraction of the acquired holograms due to these memory limitations.

To improve image reconstructions, the source of imaging artifacts need to be better understood and memory usage has to be optimized.

A fundamental dilemma in digital holography is the poor use it makes of the limited space-bandwidth product of the camera. A large number of sensor pixels would allow for a larger field of view. Alternatively, an in-line holographic could be explored [139].

It should be noted that the images shown in Figs. 9.5 to 9.6 do not represent the reconstructions of the original sample, but the scattered wave field emitted from the sample region. The emitted near-field waves cannot be collected by holographic recording and this information is thus lost.

The advantage of holographic over classical OCT reconstruction becomes stronger for high NA. If the reconstruction is to be applied to holograms acquired with a high NA objective, polarization effects can be taken into account and aberrations can be corrected numerically. Another advantage is the higher imaging speed due to the parallel acquisition over the full field of view. To achieve this, high-speed cameras are required.

The current reconstruction does not solve the problem of missing low spatial frequency components on the Ewald sphere. Taking the absolute square of the reconstructed amplitudes shifts spatial frequencies down into this range, but cannot reconstruct the missing information and might even lead to unwanted artifacts. A promising approach to improve the reconstruction are therefore deconvolution-based methods which take the additional phase information into account.

In comparison to inverse scattering approaches such as ISAM [78] no regularization techniques for a mathematical inversion of the scattering model are required. Instead, the reconstruction models propagation of light and the imaging of a lens, both of which are well-described in the literature.

Multiple scattering is a remaining problem in this approach. The first order Born approximation has been assumed throughout this thesis and multiple scattering effects have been neglected. A novel reconstruction based on maximum-likelihood deconvolution was recently published [140], which allows for reconstruction of multiple scattered light in transmission by training an artificial neural network to reproduce the complex amplitude of the experimentally measured scattered light.

An interesting application of full-field holoscopy could be hybrid imaging methods with inelastic scattering methods such as fluorescence or Raman imaging [141].

Elastically and inelastically scattered light has different wavelengths and can be separated by suitable filters. A full-field OCT acquisition with holographic reconstruction can provide cross-sectional images of tissue structures while fluorescence or Raman imaging add chemical selectivity. This helps to differentiate pathological tissue with similar morphological or optical properties to normal tissue.

Part IV.

Appendix

A

Fourier Transforms and their Properties

The following sections follow closely the chapters 2.1.4 & 2.1.5 of the book *Introduction to Fourier Optics* by J. W. Goodman [41].

A.1. Fourier Transform Pairs

Object plane	*Fourier plane*
Plane wave	Delta peak
Delta peak	constant (if δ is at zero) or phase slope of constant amplitude
Gaussian	Gaussian*
δ-comb	δ-comb with inverse scaling
sin function	Two delta peaks

A.2. Separable Functions

If a function g is separable in polar coordinates (r, θ) if

$$g(r,\theta) = g_R(r)\; g_\Theta(\theta)\,.$$

The Fourier transform of a function which is separable in polar coordinates can be written as an infinte sum of weighted *Hankel transformations*. The Hankel transform operator $\mathcal{H}$ is defined as

$$\mathcal{H}_k\left\{g_R(r)\right\} = 2\pi \int\limits_0^\infty r\, g_R(r)\, J_k(2\pi r\rho)\, d$$

where J_k is the k^{th}-order Bessel function of the first kind.

$$\mathcal{F}\left\{g(r,\theta)\right\} = \sum_{k=-\infty}^{\infty} c_k\,(-i)^k\; e^{ik\phi}\mathcal{H}_k\left\{g_R(r)\right\}$$

with

$$c_k = \frac{1}{2\pi} \int_0^{2\pi} g_\Theta(\theta)\; e^{-ik\theta} d\theta.$$

Functions with Circular Symmetry

A function g is called *circular symmetric* if it can be expressed as a function of r alone:

$$g(r,\theta) = g_R(r).$$

Its Fourier transform is given by

$$\begin{aligned} \mathcal{F}\{g(r,\theta)\} &= G(\rho,\phi) \\ &= \int_{\theta=0}^{2\pi} \int_{r=0}^{\infty} g_R(r)\; e^{-i2\pi\cdot f(\phi,\rho)} r\, dr\, d\theta. \end{aligned}$$

This can be rewritten by using a *zero-order Bessel function of the first kind* J_0 [142]

$$J_0(a) = \frac{1}{2\pi} \int_0^{2\pi} e^{-ia\cos(\theta-\phi)}\, d\theta.$$

The dependence of the transform on the angle ϕ disappers and the Fourier transform G becomes circularly symmetric itself. The *zero-order Hankel transform* is essentially the two dimensional Fourier transform of a circularly symmetric function

$$\begin{aligned} G(\rho,\phi) = G(\rho) &= 2\pi \int_0^{\infty} r\, g_R(r)\, J_0(2\pi r\rho)\, dr \\ &= \mathcal{H}\{g_R(r)\} \end{aligned}$$

Zero-order Hankel transform of a circle

A ring-delta function is given by

$$g(r) = \frac{1}{2\pi r}\delta(r - r_0).$$

Because this function is circular symmetric, its 2D Fourier transform is

$$\begin{aligned}
G(\rho) &= \mathcal{F}_{\mathrm{2D}}\left\{g(r)\right\} = \mathcal{H}\left\{g(r)\right\} \\
&= 2\pi \int\limits_0^\infty g(r)\, J_0(2\pi r\rho)\; r\, dr \\
&= 2\pi \int\limits_0^\infty \left(\frac{1}{2\pi r}\delta(r-r_0)\right) J_0(2\pi r\rho)\; r\, dr \\
&= \int\limits_0^\infty \delta(r-r_0)\, J_0(2\pi r\rho)\; dr \\
&= J_0(2\pi r_0\rho),
\end{aligned}$$

a zero-order Bessel function.

B

Calculation of $\mathfrak{G}(\mathbf{r})$

To analyze the meaning of $\mathfrak{G}(\mathbf{r})$ and simplify the expression in Eq. 7.5 on page 78, *Parseval's theorem* can be applied. It states that since the Fourier transform is unitary, the integral of the square of a function is equal to the integral of the square of its transform

$$\begin{aligned} \mathfrak{G}(\mathbf{r}) &= \int \left[E_{\mathrm{OCT}}(\mathbf{r}) \cdot E^*_{\mathrm{OCT}}(\hat{\mathbf{r}})\right]\big|_{z=0} \,\mathrm{d}x\mathrm{d}y \\ &= \int \left[\tilde{E}_{\mathrm{OCT}}(\mathbf{k}) \cdot \tilde{E}^*_{\mathrm{OCT}}(\hat{\mathbf{k}})\right] \mathrm{d}k_x \mathrm{d}k_y \mathrm{d}k_z. \end{aligned} \tag{B.1}$$

$\tilde{E}_{\mathrm{OCT}}(\mathbf{k})$ can be derived from the expression for $E_{\mathrm{OCT}}(\mathbf{r})$ found in Eq. 7.2.

$$\tilde{E}_{\mathrm{OCT}}(\mathbf{k}) = \left[\left\{\tilde{\eta}(\mathbf{k}) \cdot e^{\mathrm{i}\ \mathbf{kd}} + \delta(\mathbf{k})\right\} \otimes \tilde{B}(\mathbf{k})\right] \cdot \mathrm{ATF}(\mathbf{k}) \tag{B.2}$$

Inserting B.2 back into B.1 gives the expression

$$\begin{aligned} \mathfrak{G}(\mathbf{r}) = & \int \left(\left[\left\{\tilde{\eta}(\mathbf{k}) \cdot e^{\mathrm{i}\ \mathbf{kd}} + \delta(\mathbf{k})\right\} \otimes \tilde{B}(\mathbf{k})\right] \cdot \mathrm{ATF}(\mathbf{k})\right) \\ & \cdot \left(\left[\left\{\tilde{\eta}^*(\hat{\mathbf{k}}) \cdot e^{\mathrm{i}\ \hat{\mathbf{k}}\mathbf{d}} + \delta^*(\hat{\mathbf{k}})\right\} \otimes \tilde{B}^*(\hat{\mathbf{k}})\right] \cdot \mathrm{ATF}^*(\hat{\mathbf{k}})\right) \mathrm{d}\mathbf{k}. \end{aligned} \tag{B.3}$$

Of course the amplitude transfer function, the Bessel ring and the Delta function are rotationally symmetric, if the entire system has been well centered. Hence,

$$\mathrm{ATF}(\mathbf{k}) \equiv \mathrm{ATF}^*(\hat{\mathbf{k}}) \quad \text{and} \quad \tilde{B}(\mathbf{k}) \equiv \tilde{B}^*(\hat{\mathbf{k}}) \quad \text{and} \quad \tilde{\delta}(\mathbf{k}) \equiv \tilde{\delta}^*(\hat{\mathbf{k}})$$

and we can rewrite B.3 as

$$\begin{aligned} \mathfrak{G}(\mathbf{r}) = & \int \left(\left[\left\{\tilde{\eta}(\mathbf{k}) \cdot e^{\mathrm{i}\ \mathbf{kd}} + \delta(\mathbf{k})\right\} \otimes \tilde{B}(\mathbf{k})\right] \cdot \mathrm{ATF}(\mathbf{k})\right) \\ & \cdot \left(\left[\left\{\tilde{\eta}^*(\hat{\mathbf{k}}) \cdot e^{\mathrm{i}\ \hat{\mathbf{k}}\mathbf{d}} + \delta(\mathbf{k})\right\} \otimes \tilde{B}(\mathbf{k})\right] \cdot \mathrm{ATF}(\mathbf{k})\right) \mathrm{d}\mathbf{k}. \end{aligned} \tag{B.4}$$

The expression can be further simplified if we consider that $\delta(\mathbf{k}) \otimes \tilde{B}(\mathbf{k}) = \tilde{B}(\mathbf{k})$ and if we assume that the ATF is 1 everywhere on the cap and fully supports the Bessel ring

$$\mathrm{ATF}(\mathbf{k}) \cdot \mathrm{ATF}(\mathbf{k}) = \mathrm{ATF}(\mathbf{k}) \quad \text{and} \quad \tilde{B}(\mathbf{k}) \cdot \mathrm{ATF}(\mathbf{k}) = \tilde{B}(\mathbf{k})$$

$$\begin{aligned}
\mathfrak{G}(\mathbf{r}) &= \int \Big[\big\{ \tilde{\eta}(\mathbf{k}) \cdot e^{\mathrm{i}\ \mathbf{kd}} + \delta(\mathbf{k}) \big\} \otimes \tilde{B}(\mathbf{k}) \Big] \\
&\quad \cdot \Big[\Big\{ \tilde{\eta}^*(\hat{\mathbf{k}}) \cdot e^{\mathrm{i}\ \hat{\mathbf{k}}\mathbf{d}} + \delta(\mathbf{k}) \Big\} \otimes \tilde{B}(\mathbf{k}) \Big] \cdot \mathrm{ATF}(\mathbf{k})\ \mathrm{d}\mathbf{k}. \\
&= \int \Big\{ \tilde{\eta}(\mathbf{k}) \cdot e^{\mathrm{i}\ \mathbf{kd}} \otimes \tilde{B}(\mathbf{k}) + \tilde{B}(\mathbf{k}) \Big\} \\
&\quad \cdot \Big\{ \tilde{\eta}^*(\hat{\mathbf{k}}) \cdot e^{\mathrm{i}\ \hat{\mathbf{k}}\mathbf{d}} \otimes \tilde{B}(\mathbf{k}) + \tilde{B}(\mathbf{k}) \Big\} \cdot \mathrm{ATF}(\mathbf{k})\ \mathrm{d}\mathbf{k}. \qquad \text{(B.5)}
\end{aligned}$$

To reconstruct an OCT image, we have to isolate the cross-correlation term from this expression. To this end, the multiplications are expanded to

$$\begin{aligned}
\mathfrak{G}(\mathbf{r}) = \int \Big[&\Big\{ \tilde{\eta}(\mathbf{k})\ e^{\mathrm{i}\ \mathbf{kd}} \otimes \tilde{B}(\mathbf{k}) \Big\} \cdot \Big\{ \tilde{\eta}^*(\hat{\mathbf{k}})\ e^{\mathrm{i}\ \hat{\mathbf{k}}\mathbf{d}} \otimes \tilde{B}(\mathbf{k}) \Big\} + \tilde{B}^2(\mathbf{k}) \\
&+ \Big\{ \tilde{\eta}^*(\hat{\mathbf{k}})\ e^{\mathrm{i}\ \hat{\mathbf{k}}\mathbf{d}} \otimes \tilde{B}(\mathbf{k}) \Big\} \cdot \tilde{B}(\mathbf{k}) + \Big\{ \tilde{\eta}(\mathbf{k})\ e^{\mathrm{i}\ \mathbf{kd}} \otimes \tilde{B}(\mathbf{k}) \Big\} \cdot \tilde{B}(\mathbf{k}) \Big] \cdot \mathrm{ATF}(\mathbf{k})\ \mathrm{d}\mathbf{k}.
\end{aligned}$$

Separating the integration terms yields

$$\begin{aligned}
\mathfrak{G}(\mathbf{r}) = &\int \Big[\Big\{ \tilde{\eta}(\mathbf{k})\ e^{\mathrm{i}\ \mathbf{kd}} \otimes \tilde{B}(\mathbf{k}) \Big\} \cdot \Big\{ \tilde{\eta}^*(\hat{\mathbf{k}})\ e^{\mathrm{i}\ \hat{\mathbf{k}}\mathbf{d}} \otimes \tilde{B}(\mathbf{k}) \Big\} \Big] \cdot \mathrm{ATF}(\mathbf{k})\ \mathrm{d}\mathbf{k} \\
&+ \int \tilde{B}^2(\mathbf{k}) \cdot \mathrm{ATF}(\mathbf{k})\ \mathrm{d}\mathbf{k} \\
&+ \int \Big\{ \tilde{\eta}^*(\hat{\mathbf{k}})\ e^{\mathrm{i}\ \hat{\mathbf{k}}\mathbf{d}} \otimes \tilde{B}(\mathbf{k}) \Big\} \cdot \tilde{B}(\mathbf{k}) \cdot \mathrm{ATF}(\mathbf{k})\ \mathrm{d}\mathbf{k} \\
&+ \int \Big\{ \tilde{\eta}(\mathbf{k})\ e^{\mathrm{i}\ \mathbf{kd}} \otimes \tilde{B}(\mathbf{k}) \Big\} \cdot \tilde{B}(\mathbf{k}) \cdot \mathrm{ATF}(\mathbf{k})\ \mathrm{d}\mathbf{k}
\end{aligned}$$

which can again be simplified to

$$\begin{aligned}
\mathfrak{G}(\mathbf{r}) = &\int \Big[\Big\{ \tilde{\eta}(\mathbf{k})\ e^{\mathrm{i}\ \mathbf{kd}} \otimes \tilde{B}(\mathbf{k}) \Big\} \cdot \Big\{ \tilde{\eta}^*(\hat{\mathbf{k}})\ e^{\mathrm{i}\ \hat{\mathbf{k}}\mathbf{d}} \otimes \tilde{B}(\mathbf{k}) \Big\} \Big] \cdot \mathrm{ATF}(\mathbf{k})\ \mathrm{d}\mathbf{k} \\
&+ \int \tilde{B}^2(\mathbf{k})\ \mathrm{d}\mathbf{k} \\
&+ \int \Big\{ \tilde{\eta}^*(\hat{\mathbf{k}})\ e^{\mathrm{i}\ \hat{\mathbf{k}}\mathbf{d}} \otimes \tilde{B}(\mathbf{k}) \Big\} \cdot \tilde{B}(\mathbf{k})\ \mathrm{d}\mathbf{k} \\
&+ \int \Big\{ \tilde{\eta}(\mathbf{k})\ e^{\mathrm{i}\ \mathbf{kd}} \otimes \tilde{B}(\mathbf{k}) \Big\} \cdot \tilde{B}(\mathbf{k})\ \mathrm{d}\mathbf{k}.
\end{aligned}$$

C

Operation of the Holoscopic Imaging System

This chapter serves as a reference for the operation of the holoscopic platform for future users.

Operation Manual for the Holoscopy system

1. Turn on the laser and camera
2. Connect to the University **via Shrew Soft VPN**
3. Start **camera software**

   a) Open Camera

   In the list, select **Motion Xtra N/NR/NX/O on Gigabit-Ethernet**
   If the it does not appear in the list, the camera might not be ready yet. Wait a minute and try again.

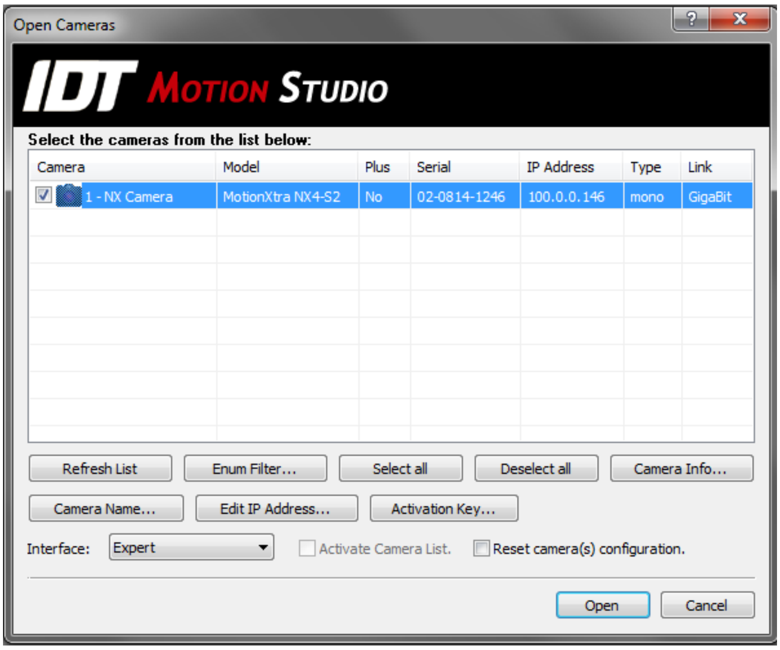

Select the cameras from the list below:

Camera	Model	Plus	Serial	IP Address	Type	Link
☑ 1 - NX Camera	MotionXtra NX4-S2	No	02-0814-1246	100.0.0.146	mono	GigaBit

Interface: Expert

☐ Activate Camera List.

☐ Reset camera(s) configuration.

   b) Open the **Camera Calibration** dialogue
   Menu > Camera > Advanced > Camera Calibration

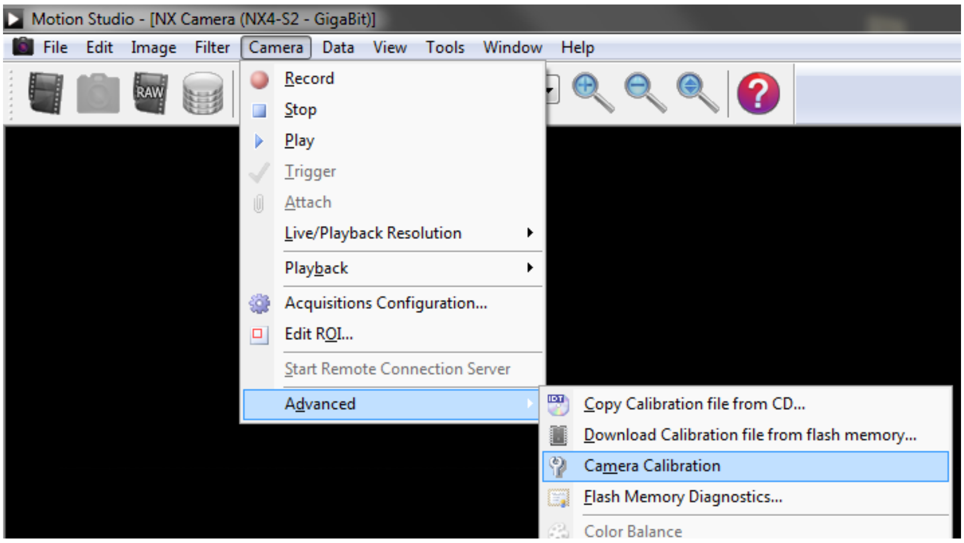

c) Disable all automatic correction and show the histrogram to avoid overexposure

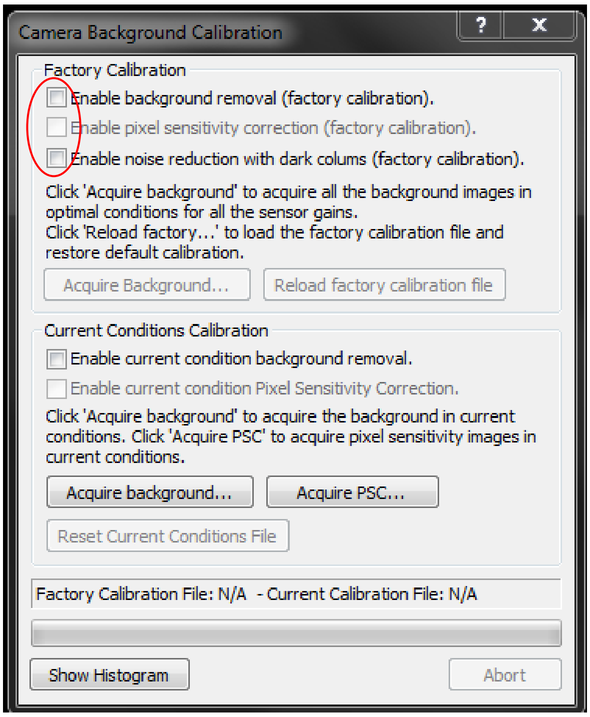
Camera Background Calibration

Factory Calibration

☐ Enable background removal (factory calibration).
☐ Enable pixel sensitivity correction (factory calibration).
☐ Enable noise reduction with dark colums (factory calibration).

Click 'Acquire background' to acquire all the background images in optimal conditions for all the sensor gains.
Click 'Reload factory...' to load the factory calibration file and restore default calibration.

Current Conditions Calibration

☐ Enable current condition background removal.
☐ Enable current condition Pixel Sensitivity Correction.

Click 'Acquire background' to acquire the background in current conditions. Click 'Acquire PSC' to acquire pixel sensitivity images in current conditions.

Factory Calibration File: N/A - Current Calibration File: N/A

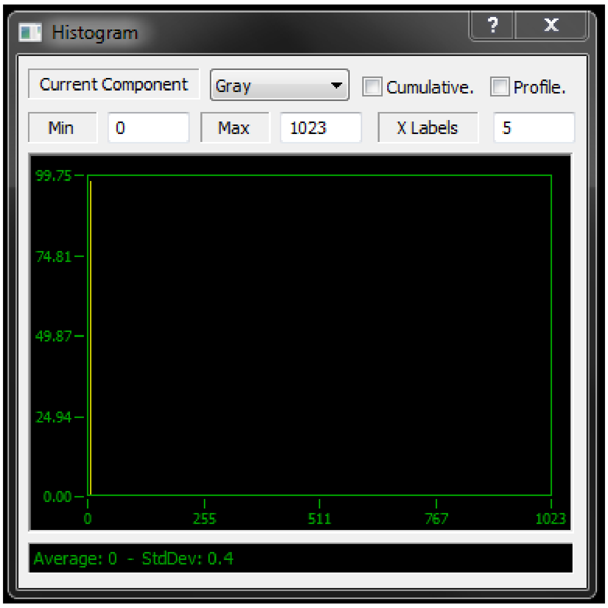
Histogram

Current Component: Gray ☐ Cumulative. ☐ Profile.

Min 0 Max 1023 X Labels 5

Average: 0 - StdDev: 0.4

Set the **Camera & Trigger settings**

- *Rate* 2000 Hz, *Exposure* dependent on sample
- *ROI* and *Pixel Depth* according to desired experiment
- 1800 *Frames* + 1-2 *Pre-Trigger* frames
- *Trigger*: Edge-High (= triggered by start of sweep of the BroadSweeper)

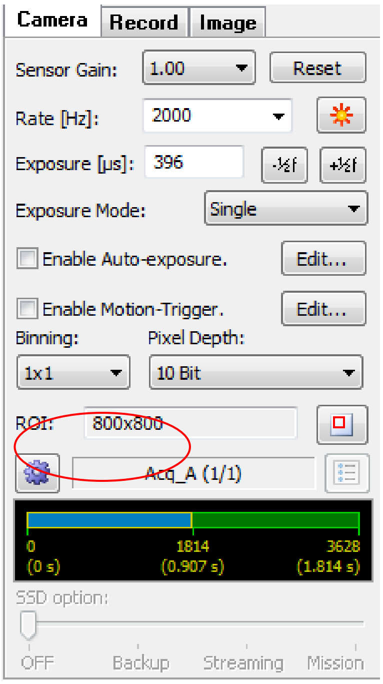

Sensor Gain: 1.00

Rate [Hz]: 2000

Exposure [µs]: 396

Exposure Mode: Single

☐ Enable Auto-exposure.

☐ Enable Motion-Trigger.

Binning: 1x1

Pixel Depth: 10 Bit

ROI: 800x800

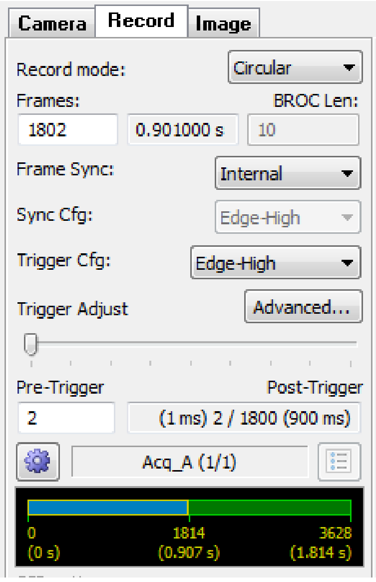

Record mode: Circular

Frames: 1802 0.901000 s

BROC Len: 10

Frame Sync: Internal

Sync Cfg: Edge-High

Trigger Cfg: Edge-High

Trigger Adjust

Pre-Trigger: 2

Post-Trigger: (1 ms) 2 / 1800 (900 ms)

4. Start **laser remote control**
    - Connected via “fake” USB-COM port
    - High power mode is recommended

    a) **Automatic Mode**: Sweep with defined speed and range (for recording)

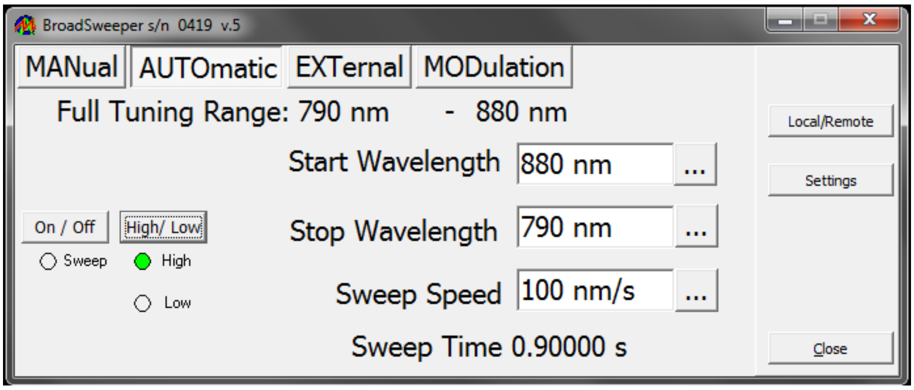
BroadSweeper s/n 0419 v.5

Full Tuning Range: 790 nm - 880 nm

Start Wavelength 880 nm

Stop Wavelength 790 nm

Sweep Speed 100 nm/s

Sweep Time 0.90000 s

○ Sweep ● High ○ Low

    b) **Manual Mode**: One wavelength (for alignment)

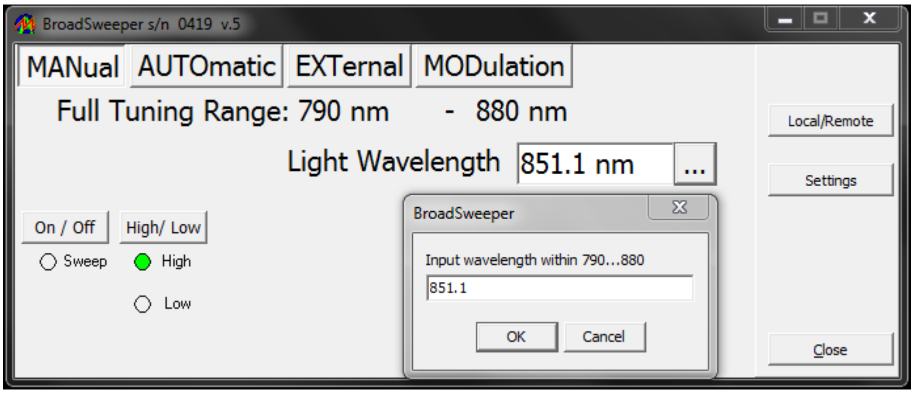
BroadSweeper s/n 0419 v.5

Full Tuning Range: 790 nm - 880 nm

Light Wavelength 851.1 nm

○ Sweep ● High ○ Low

BroadSweeper

Input wavelength within 790...880

851.1

5. Mount sample
    a) Close reference arm and use flip-mounted lens to focus the sample plane on the camera and adjust the position

6. Start Matlab
    a) Run script
        - Maybe increase integration time
        - Right: live image, Left: FT of live image

    b) Use **field aperture** to limit the field of view (-> bandwidth of cross-correlation terms in the FT) to approx. ¼ of the chip size (or more, if you want)

    c) Use **reference arm beam walk** to change the angle offset and position the cross-correlation terms until they do no overlap or wrap around the edges

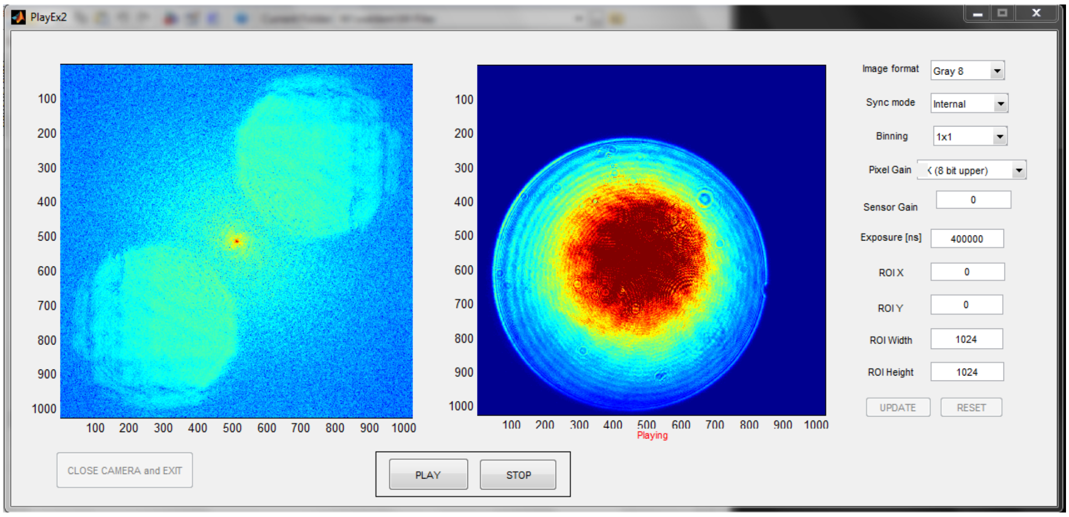
PlayEx2

Image format: Gray 8

Sync mode: Internal

Binning: 1x1

Pixel Gain: (8 bit upper)

Sensor Gain: 0

Exposure [ns]: 400000

ROI X: 0

ROI Y: 0

ROI Width: 1024

ROI Height: 1024

Playing

D

IFTA Code

```
% Experiment filename & settings string
    filename='test';
    IFTA_settings='SETTINGS';

%% PARAMETERS
    exx=40;         % DEBUG: overlap to be sure that pattern is
       displayed
    sx=800; sy=600; % size of the Hamamatsu SLM in pxl (+exx)

    ring=0.38;          % ring diameter in pixels along x direction
        (~150/800)
    % ring=0.075;

    ringDiam=0.003;     % Thickness of ring (~5/800)
    ringDiamBig=0.006;  % Thickness of ring (~5/800)
    maxfreq=0.3;        % maximal relative frequency to limit
       pattern display
    IFTA_settings=strcat(IFTA_settings,'\n','Maximum Frequency:   '
       ,num2str(maxfreq));
    iter=1000;
    illusize=268;
      % illusize=sx/6;  % 0 means plane illumination, other :
         Gaussian illu
      % illusize=0;
      % illusize=175*2; % First estimation of the size of the
         Gaussian
    % NB : Gaussian illumination yields better results

    ForceRingRatio=0.15; % Percentage of power that will be in the
       ring

    baffle_border_low=0.5; %0.4; % Borders for the baffle
    baffle_border_high=1.3; %1.7;
    apmax=ring*baffle_border_high;
    apmin=ring*baffle_border_low;
    IFTA_settings=strcat(IFTA_settings,'\n','Baffle Size:   ',
       num2str(baffle_border_low),' ; ',num2str(baffle_border_high)
       );


%% OPTION SWITCHES
    phase_switch='triangular';
    % 'random' | 'constant' | 'rectangular' | 'triangular'
```

```
    ring_apodization=true;  % {ON} |  OFF
    watch_iteration=false;  %  ON  | {OFF}
    display_on_SLM=false;   %  ON  | {OFF}

%% SIMULATE ILLUMINATION
    if illusize>0
        illu=exp(-(rr(sx,sy)/illusize).^2);
        IFTA_settings=strcat(IFTA_settings,'\n','Illumination Mode:
               Gaussian');
    else
        illu=1+newim(sx,sy);
        IFTA_settings=strcat(IFTA_settings,'\n','Illumination Mode:
               Plane');
    end
    illu = illu / sum(illu); % WHY?

    myrr            = rr(sx,sy,'freq');
        % For Fourier space (so that SLM display is not stretched
           after ift)
        % myrr=cut(myrr,[sx sy]);

    Baffle1         = myrr<apmax  & myrr>apmin;
    ForceRingSmall  = myrr<ring+ringDiam/2  & myrr>ring-ringDiam/2;
    ForceRing       = myrr<ring+ringDiamBig/2  & myrr>ring-
       ringDiamBig/2;
        % Ring where the constraints will be applied

%% SIMULATE PHASE DISTRIBUTION (start value)
    period=6; %16  % choose even numbers
    SLM_2pi=158;   % Hamamatsu value for 2pi for our wavelength

    switch phase_switch
        case 'random'
        % NB: yields entirely different results
        myphase=pi*noise(newim(sx,sy));
        IFTA_settings=strcat(IFTA_settings,'\n','Start Phase:
           randomized');

        case 'rectangular'
        mymask  = mod(rr(sx,sy),period)<(period/2);   % [0,1]
        myphase = mymask*SLM_2pi;                      % [0,2pi]
        IFTA_settings=strcat(IFTA_settings,'\n','Start Phase:
           annular rectangular grating');

        case 'triangular'
        mymask  = abs(mod(rr(sx,sy)/period,1)-0.5)*2; % [0,1]
        myphase = mymask*SLM_2pi;                      % [0,2pi]
        IFTA_settings=strcat(IFTA_settings,'\n','Start Phase:
           annular triangular grating');

        otherwise %constant
        myphase=newim(zeros(sy,sx));
        IFTA_settings=strcat(IFTA_settings,'\n','Start Phase:
           constant');
```

```
    end

    MyInt=1;

%% SIMULATE RING
    MyRing = newim(sx,sy);
    if (ring_apodization)    % {ring is apodized}
        MyRing(ForceRingSmall)=sqrt(ForceRingRatio/sum(ForceRing));
        MyRing=gaussf(MyRing);  % Apodization
        IFTA_settings=strcat(IFTA_settings,'\n','Ring Apodization:
            apodized');
    else                     % ring is constant
        MyRing(ForceRing)=sqrt(ForceRingRatio/sum(ForceRing));
        IFTA_settings=strcat(IFTA_settings,'\n','Ring Apodization:
            constant');
    end


%% ITERATION
IFTA_settings=strcat(IFTA_settings,'\n','# Iterations: ', num2str(
   iter));
for n=1:iter

% AMPLITUDE DISTRIBUTION IN REAL SPACE :
        close all;
    % Apply low frequency constraint to display pattern
        myphase = real(ift(ft(myphase) .* (rr(myphase,'freq') <
           maxfreq)));
    % calculate amplitude distribution
        famp=ft(exp(i*myphase) .* illu);
            % famp(~Baffle1)=0;

        sfamp=famp % Save amplitude before applying constraints

% APPLY FOURIER SPACE CONSTRAINTS
      % 1/ Intensity in the ring should be equal to the defined
         ratio, as
      % compared to total intensity in Fourier plane
      % sum(ForceRing) is the number of pixels in the ring
            myamp= sqrt(sum(real(famp.*conj(famp))));
            famp(ForceRing)=MyRing(ForceRing)*myamp;

      % 2/ The amplitude outside the ring but inside the baffle
         should be 0
            famp(~ForceRing & Baffle1)=0;

% QUANTIFY ERROR (should decrease at each iteration => 1e-8) :
        myerr=sum(real((famp(Baffle1)-sfamp(Baffle1)).*conj(famp(
           Baffle1)-sfamp(Baffle1))));
        freal=ift(famp);

% FORCE TO BE PHASE-ONLY
% (because SLM is phase only and illumination is fixed
   experimentally)
```

```
        myphase=phase(freal);
        fprintf('N : %d, Err : %g\n',n,myerr)
        MyInt=real(freal .* conj(freal));

% WATCH
% to look at intermediate results of every 20th iteration
    if watch_iteration && (mod(n,20)==0) % OFF
            dipshow(sfamp);
            dipshow(freal);
            dipshow(myphase);
    end
end

% apply low frequency filter again to final phase display
myphase = real(ift(ft(myphase) .* (rr(myphase,'freq') < maxfreq)));

frealF=ift(sfamp .* Baffle1);

MyIntFinal=real(frealF .* conj(frealF))
sfamp
myphase

%% PHASE PATTERN TO ADDRESS SLM WITH
    DipsPhase=(phase(freal*i)+pi)/2/pi*255

%% SAVE IMAGE & EXPERIMENTAL PARAMETERS
     % Save image (used in display_grating option 7)
    imagename=[filename '.tif'];
    writeim(DipsPhase,imagename)

    % Save textfile with paras
    textname=[filename '.txt'];
    txt = fopen(textname,'w');
    fprintf(txt,IFTA_settings);
    fclose(txt);

%% SHIFT PATTERN TO DESIRED POSITION AND DISPLAY ON SLM
    if(display_on_SLM)
        DispPhase
    end
```

E

Holoscopy Reconstruction Code

```
% Reconstruction algorithm for holograms recorded with a swept source
% holoscopic system
% %%%%%%%%%%%%%%%%%%%%%%%%%%%%%%%%%%%%%%%%%%%%%%%%%%%%%%%%%%%%%%%%%%%%%%%


% Has this data been pre-processed before?
    % Experimental meta data
    myPath=[holoroot '2015-04-02_ScatteringSamplesBHeise\0-5 square_MediumFOV\'];
    if (exist([myPath 'paras'],'file')>0)
        load([myPath 'paras']);
    end

    % Acquired data
    if ~(exist([myPath 'AllSubtract180'],'file')>0)
    % if not existent: load it, else: jump to QUICK LOAD


    %%%%%%%%%%%%%%%%%%%%%%%%%%%%% PRE-PROCESSING %%%%%%%%%%%%%%%%%%%%%%%%%%%%%
        %% LOAD RAW DATA
            if ~exist('AllHolo','var')
                fprintf('Reading in holograms \n');
                AllHolo = myaviread([myPath 'Holo.avi']);
                % AllHolo = readavi([myPath 'Holo']);

                fprintf('Reading in references \n');
                AllRef  = myaviread([myPath 'Ref.avi']);
                % AllRef  = readavi([myPath 'Ref']);

                %SAMPLE and DARK images have not been recorded for each
                %data set and only loaded here if they exist.
                if (exist([myPath 'Sam.avi'],'file')>0)
                    fprintf('Reading in sample images \n');
                    AllSam  = myaviread([myPath 'Sam.avi']);
                    % AllSam=readavi([myPath 'Sam']);
                end

                if (exist([myPath 'Dark.avi'],'file')>0)
                    %AllDark=readavi([myPath 'Dark']);
```

```
            fprintf('Reading in dark images \n');
            AllDark=myaviread([myPath 'Dark.avi']);
        end

        % old/alternative load functions
        %       AllHolo=readtimeseries([myPath 'file']);
        %       AllHolo=AllHolo{1}; AllHolo=squeeze(AllHolo
           (:,:,1,:));
        %       AllRef=readavi('file');
    end


%% REMOVE PRE-TRIGGER FRAMES & SELECT SUBSET
    ntrig=2; % Number of pre-Trigger frames
        % this number is either a known acquisition
           parameter or can be
        % found manually by looking at the CC in the FT:
        % AllHoloFT=ft2d(AllHolo(:,:,0:10));
        % dipshow(AllHoloFT,'log')
    darkleft=3; % some problematic pixels on the left
    lambdaSub=10; %to sub-sample the data stack for faster
       reconstruction

    % HOLOGRAMS (Ref+Sam)
        AllHoloSub=AllHolo(darkleft:end,:,ntrig:lambdaSub:
           end); %clear AllHolo;
        % Indexing starts at 0 (otherwise it would be ntrig
           +1)
    % REFERENCE arm alone
        AllRefSub=AllRef(darkleft:end,:,ntrig:lambdaSub:end
           ); %clear AllRef;
    % SAMPLE arm alone
        if (exist('AllSam','var'))
            AllSamSub=AllSam(darkleft:end,:,ntrig:lambdaSub
               :end); %clear AllSam;
        end
    % DARK image
        if (exist('AllDark','var'))
            AllDarkSub=AllDark(darkleft:end,:,ntrig:
               lambdaSub:end); %clear AllDark;
        end


%% REMOVE OFFSET
    AllHoloSub=AllHoloSub-mean(AllHoloSub(0:100,0:100,:)
       ,[],[1 2]);
    AllRefSub=AllRefSub-mean(AllRefSub(0:100,0:100,:),[],[1
        2]);
    if (exist('AllSamSub','var'))
        AllSamSub=AllSamSub-mean(AllSamSub(0:100,0:100,:)
           ,[],[1 2]);
    end

%% NORMALIZATION; SUBTRACT SAMPLE & REFERENCE IMAGES
```

```
            myFilterSize=10;
            LeftEdge=10;  % Pixels to the data region on the left side (for BG pattern removal)

            % calculate the mean brightness (over xy) in each image
            mhol  = mean(AllHoloSub,[],[1 2]);
            mref  = mean(AllRefSub,[],[1 2]);
            if (exist('AllSamSub','var'))
                msam  = mean(AllSamSub,[],[1 2]);
                AllSubtract = (AllHoloSub./mhol).*gaussf(mhol,[0 0 myFilterSize]) - (AllRefSub./mref).*gaussf(mref,[0 0 myFilterSize]) - (AllSamSub./msam).*gaussf(msam,[0 0 myFilterSize]);
            else
                AllSubtract = (AllHoloSub./mhol).*gaussf(mhol,[0 0 myFilterSize]) - (AllRefSub./mref).*gaussf(mref,[0 0 myFilterSize]);
            end


        %% REMOVE CAMERA LINE PATTERN
            mleft=mean(AllSubtract(0:LeftEdge,:,:),[],[1 3]);
            mright=mean(AllSubtract(end-LeftEdge:end,:,:),[],[1 3]);
            myxx=xx([size(AllSubtract,1) size(AllSubtract,2)],'freq')+0.5;
            AllSubtract = cuda(AllSubtract) - myxx.*mright - (1-myxx).*mleft;
                % Alternative:
                % AllSubtract=AllSubtract-dip_image_force(myxx.*mright+(1-myxx).*mleft);
            msub  = mean(AllSubtract,[],[1 2]);


        %% CONTROL OPTIONS
            % COMPARE MEAN
                % figure;plot(double(squeeze(msam)),'b');hold on;plot(double(squeeze(mhol)),'g');plot(double(squeeze(mref)),'r');plot(double(squeeze(msub)),'m')
            % LOOK AT FTs OF HOLOGRAMS?
                % AllHoloFT=ft2d(AllHoloSub(:,:,:));
                % dipshow(AllHoloFT,'log')
            writeim(AllSubtract,[myPath 'AllSubtract'],'ICSv2'); % to load quickly next time

    else %% QUICK LOAD
        AllSubtract=readim([myPath 'AllSubtract1800'])-128.0;
        enableCuda();
        a=AllSubtract; AllSubtract=cuda(AllSubtract(:,:,0:10:end));

%         %WORKAOUND FOR LAPTOP (Memory...)
%             AllSubtract=readim([myPath 'AllSubtract180']);
%             AllSubtract=AllSubtract(:,:,0:6:end);
```

```
%             AllSubtract=AllSubtract-128.0;
    end


%%%%%%%%%%%%%%%%%%%%%%%%%%%%% RECONSTRUCTION
   %%%%%%%%%%%%%%%%%%%%%%%%%%%%%
    %% PARAS
        %Objective parameters
            NA = 0.25; Magn = 10; f_TL = 0.18;
                % tube length = 180 mm (Olympus 10x/0.25); 164,5 mm
                    (ZEISS 20x/0.4)
            FocalLength = f_TL / Magn; %[m]
            R_BFP = FocalLength* NA; %[m]

        % Camera parameters
            pxlsize=13.9 *10^(-6); %[m] IDT NX4
            % pxlsize=6.45*10^(-6); % [m] Andor Clara

        % Light source parameters
                % Broadsweeper provides k-linear wavelength tuning
            k_start  = (2*pi./880).*10^9;   k_end = (2*pi./790)
               .*10^9;
            dk       = k_end-k_start; %[1/m]
            ks       = k_start + (k_end-k_start)*[0:(size(
               AllSubtract,3)-1)]/(size(AllSubtract,3)-1);
            lambdanm = 2*pi./ks;
                %lambda=880-90*[0:(size(AllSubtract,3)-1)]/(size(
                   AllSubtract,3)-1); %[nm]
                %lambdanm=lambda.*10^(-9); %[m]

    %% STEP 1: Extract the cross-correlation terms from the
       recorded holograms
        fprintf('STEP 1: Extract the cross-correlation terms from
           the recorded holograms\n');
        if (exist('HoloCenter','var'))  %If this parameter has been
            saved before, re-use it
            [myFAmp,HoloRange]=ExtractCrossCorrelation2(AllSubtract
               ,lambdanm,HoloRange);
        else
            [myFAmp,HoloRange]=ExtractCrossCorrelation2(AllSubtract
               ,lambdanm);
        end

        %CONTROL OPTION: compare real and conjugate image
        if(0)
            mysize=size2d(AllSubtract);
            myx=mysize(1); myy=mysize(2);
            HoloRange2=[myx-HoloRange(2),myy-HoloRange(4);myx-
               HoloRange(1),myy-HoloRange(3)];
            [myFAmp2,HoloRange2]=ExtractCrossCorrelation2(
               AllSubtract,lambdanm,HoloRange2);
        end

        xysize=abs(HoloRange(2,:)-HoloRange(1,:));
```

```
%% STEP 2: Apodization & optional Angle Correction
    fprintf('STEP 2: Apodization\n');
    num=size(lambdanm,2);
    origsize=size(AllSubtract); %clear AllSubtract;

        if (exist('HoloCenter','var'))  %If this parameter has been saved before, re-use it
            [AllAmp,HoloCenter]=ApodizeHolo(myFAmp,num,HoloCenter);
            if (exist('myFAmp2','var'))
                [AllAmp2,HoloCenter]=ApodizeHolo(myFAmp2,num,HoloCenter);
            end

        else % manually check if there is an angle offset in the data
            [AllAmp,HoloCenter]=ApodizeHolo(myFAmp,num);
            if (exist('myFAmp2','var'))
                [AllAmp2,HoloCenter]=ApodizeHolo(myFAmp2,num);
            end
        end
    %clear myFAmp;


%%  PARAMETERS
    newsize=size(AllAmp);
    CCDPix=[pxlsize pxlsize]; %[m]
    pxlsize=CCDPix .* (origsize(1:2) ./ newsize(1:2)); %[m]


%% STEP 3: Find focal planes
    fprintf('STEP 3: Determine the focal planes from a hologram subset\n');
    % Values from previous calibrations
        BFPPos=0.0860;
        BestFocus = -4.2346e-04;

    %Create sub-sampled image stack
        sub=6;
        % AllAmp=dip_image_force(AllAmp); %for CUDA
        AllAmpSub=AllAmp(:,:,0:sub:end);
        lambdaSub=880-90*[0:(size(AllAmpSub,3)-1)]/(size(AllAmpSub,3)-1); %[nm]
        lambdanmSub=lambdaSub.*10^(-9); %[m]

     if ~(exist('BFPPos','var'))
        nn=floor(size(AllAmp,3)/2);  a=AllAmp(:,:,nn); % pick center image
        DZ=(0.05:0.002:0.15); %experimentally plausible range
        BFP=PropagateField(a,DZ,lambdanm(nn+1),pxlsize,1);
        fh=dipshow(abs(BFP)); fprintf('click back focal plane\n');
        clicks=dipgetcoords(fh,1);
        BFPPos=DZ(clicks(3)+1);
```

```
        clear BFP;
    end

    if ~(exist('BestFocus','var'))
        TestPos=-4.544358e-04;
        % This can be repeated several times with different
           TestPos and sampling values
        % BestFocus = FindFocalPlane(AllAmp,lambdanm,pxlsize,NA
           ,FocalLength,BFPPos,TestPos,sampling,DZ);
        BestFocus=FindFocalPlane(AllAmpSub,lambdanm,pxlsize,NA,
           FocalLength,BFPPos,TestPos,pxlsize(1));
    end


%% CONTROL Look at BFP
% only the real image focusses here
    if ~(exist('AllAmp2','var'))
        [AllAmp2,HoloCenter]=ApodizeHolo(myFAmp2,num,HoloCenter
           );
        BFPlane  = ReconBFP(AllAmp,lambdanm,pxlsize,NA,BFPPos);
        BFPlane2 = ReconBFP(AllAmp2,lambdanm,pxlsize,NA,BFPPos)
           ;
        view = cat(1,BFPlane,BFPlane2)
    end


%% Step 4: DISPERSION CORRECTION (optional)
    %     fhb=dipshow(abs(BFP));
    %     fprintf('Click on Focus in BFP\n');
    %     BFPoff=dipgetcoords(fhb,1);
    if(0)
        DispersionROI=[247,220;304,268];
        [myAmpCor,DZ,DispersionVal,SamplePix]=ReconHolo3(AllAmp
           ,lambdanm,pxlsize,NA,FocalLength,BFPPos,TestPos,
           BestFocus,[],DispersionROI)

        plot(angle(DispersionVal))
        plot(abs(DispersionVal))
    end


%% Step 5: BACKPROPAGATION
    sampling=pxlsize(1);
    DZ=BestFocus; % nominal focus plane
    %DZ=(BestFocus-15*sampling):sampling:(BestFocus+15*%
       sampling);
        %stack of z-positions around nominal focal plane,
        %start:intervall:end

    if exist('cuda_cuda')
        cuda_clearheap; %avoid memory problems
    end

    % optional branch to deconvolution-based reconstruction
```

```
        %   => [myInt]=ReconDeconv(AllAmp,lambdanm,pxlsize,NA,DZ)

        % angular spectrum backpropagation
        [myInt,myAmp,DZ,DispersionVal,SamplePix]=ReconHolo4(AllAmp,
           lambdanm,pxlsize,NA,FocalLength,BFPPos,BestFocus,DZ)


    %% SIMULATE OCT RECONSTRUCTION
        % 1D FT along k
          myOCT=dip_fouriertransform(myOCTAmp,'inverse',[0 0 1]);
          %myOCT=dip_image_force(myOCT); %for CUDA
          myOCTint=abssqr(myOCT);

          % views
              aa=sum(myOCTint,[],3)
              aa2=sum(myOCTint,[],2)

          % write output
              tiffwrite([holoroot 'myInt.tif'],myInt-min(myInt),'
                 yes')


    %% PRINT PARAMETERS
        fprintf('PARAMETERS \n');
        fprintf([' HoloCenter: [' num2str(HoloCenter) ']']);
        fprintf(['\n HoloRange: [' num2str(HoloRange(1,:)) '; '
           num2str(HoloRange(2,:)) ']']);
        fprintf('\n BestFocus: %d \n',BestFocus);
        fprintf('\n BFPPos: %d \n',BFPPos);

%%%%%%%%%%%%%%%%%%%%%%%%%% END OF RECONSTRUCTION
   %%%%%%%%%%%%%%%%%%%%%%%%%%
```

Bibliography

[1] M. Walde, J. Monypenny, R. Heintzmann, G. E. Jones, and S. Cox, "Vinculin binding angle in podosomes revealed by high resolution microscopy," *PLoS ONE*, vol. 9, no. 2, 2014.

[2] A. Badgaa, R. Büchler, N. Wielsch, M. Walde, R. Heintzmann, Y. Pauchet, A. Svatos, K. Ploss, and W. Boland, "The Green Gut: Chlorophyll Degradation in the Gut of Spodoptera littoralis," *Journal of Chemical Ecology*, vol. 41, no. 11, pp. 965–974, 2015.

[3] M. Walde, A. Jost, K. Wicker, and R. Heintzmann, "Engineering an achromatic Bessel beam using a phase-only spatial light modulator and an iterative Fourier transformation algorithm," *Optics Communications*, vol. 383, pp. 64–68, 2017.

[4] R. Hooke, *Micrographia, or, Some physiological descriptions of minute bodies made by magnifying glasses :with observations and inquiries thereupon.* 1665.

[5] A. van Leeuwenhoek, "Part of a letter from Mr Antony van Leeuwenhoek, concerning the worms in sheeps livers, gnats, and animalcula in the excrements of frogs," *Philosophical Transactions (1683-1775)*, vol. 22, pp. 509–518, 1700.

[6] R. Heintzmann and G. Ficz, "Breaking the resolution limit in light microscopy.," *Briefings in Functional Genomics & Proteomics*, vol. 5, pp. 289–301, dec 2006.

[7] R. Y. Tsien, "The green fluorescent protein," *Annual Review of Biochemistry*, vol. 67, no. 1, pp. 509–544, 1998.

[8] W. S. Boyle and G. E. Smith, "Charge Coupled Semiconductor Devices," *Bell System Technical Journal*, vol. 49, no. 4, pp. 587–593, 1970.

[9] R. R. Brown, A. Deletic, and T. H. F. Wong, "Interdisciplinarity: How to catalyse collaboration," *Nature*, vol. 525, pp. 315–317, 2015.

[10] T. Čižmár, "Exploiting multimode waveguides for in vivo imaging," *SPIE Biomedical Optics & Medical Imaging*, 2015.

[11] J. B. Pawley, *Handbook of Biological Confocal Microscopy.* Plenum Press, New York, 2006.

[12] B. Judkewitz, R. Horstmeyer, I. M. Vellekoop, I. N. Papadopoulos, and C. Yang, "Translation correlations in anisotropically scattering media," *Nature Physics*, vol. 11, no. June, pp. 1–6, 2015.

[13] P. C. Lauterbur, "Image Formation by Induced Local Interactions: Examples Employing Nuclear Magnetic Resonance," *Nature*, vol. 242, no. 5394, pp. 190–191, 1973.

[14] G. N. Hounsfield, "Computerized transverse axial scanning (tomography): I. Description of system," *British Journal of Radiology*, vol. 46, no. 552, pp. 1016–1022, 1973.

[15] C. K. Hitzenberger, "Optical measurement of the axial eye length by laser Doppler interferometry," *Investigative Ophthalmology & Visual Science*, vol. 32, no. 3, p. 616, 1991.

[16] D. Huang, E. A. Swanson, C. P. Lin, J. S. Schuman, W. G. Stinson, W. Chang, M. R. Hee, T. Plotte, K. Gregory, C. A. Puliafito, and J. G. Fujimoto, "Optical Coherence Tomography," *Science*, vol. 254, pp. 1178–1181, 1991.

[17] J. J. Armstrong, M. S. Leigh, D. D. Sampson, J. H. Walsh, D. R. Hillman, and P. R. Eastwood, "Quantitative upper airway imaging with anatomic optical coherence tomography," *American Journal of Respiratory and Critical Care Medicine*, vol. 173, no. 2, pp. 226–233, 2006.

[18] A. F. Fercher, C. K. Hitzenberger, G. Kamp, and S. Y. El-Zaiat, "Measurement of intraocular distances by backscattering spectral interferometry," *Optics Communications*, vol. 117, no. 1-2, pp. 43–48, 1995.

[19] M. A. Gamulescu and H. Helbig, "OCT in macular diagnostics - possibilities and limitations.," *Klinische Monatsblätter für Augenheilkunde*, vol. 228, no. 7, pp. 599–606, 2011.

[20] N. D. Gladkova, G. A. Petrova, N. K. Nikulin, S. G. Radenska-Lopovok, L. B. Snopova, Y. P. Chumakov, V. A. Nasonova, V. M. Gelikonov, G. V. Gelikonov, R. V. Kuranov, A. M. Sergeev, and F. I. Feldchtein, "In vivo optical coherence tomography imaging of human skin: norm and pathology," *Skin Research and Technology*, vol. 6, no. 1, pp. 6–16, 2000.

[21] G. J. Tearney, M. E. Brezinski, B. E. Bouma, S. A. Boppart, C. Pitris, J. F. Southern, and J. G. Fujimoto, “In vivo endoscopic optical biopsy with optical coherence tomography.,” *Science*, vol. 276, no. 5321, pp. 2037–9, 1997.

[22] A. M. Sergeev, V. Gelikonov, G. Gelikonov, F. Feldchtein, R. Kuranov, N. Gladkova, N. Shakhova, L. Snopova, A. Shakhov, I. Kuznetzova, A. Denisenko, V. Pochinko, Y. Chumakov, and O. Streltzova, “In vivo endoscopic OCT imaging of precancer and cancer states of human mucosa,” *Optics Express*, vol. 1, no. 13, pp. 432–440, 1997.

[23] A. M. Rollins, R. Ung-Arunyawee, A. Chak, R. C. Wong, K. Kobayashi, M. V. Sivak, and J. a. Izatt, “Real-time in vivo imaging of human gastrointestinal ultrastructure by use of endoscopic optical coherence tomography with a novel efficient interferometer design.,” *Optics Letters*, vol. 24, no. 19, pp. 1358–1360, 1999.

[24] J. Schmitt, S. Lee, and K. Yung, “An optical coherence microscope with enhanced resolving power in thick tissue,” *Optics Communications*, vol. 142, no. 4-6, pp. 203–207, 1997.

[25] F. O. Fahrbach, P. Simon, and A. Rohrbach, “Microscopy with self-reconstructing beams,” *Nature Photonics*, vol. 4, pp. 780–785, nov 2010.

[26] M. Villiger, C. Pache, and T. Lasser, “Dark-field optical coherence microscopy.,” *Optics Letters*, vol. 35, pp. 3489–91, oct 2010.

[27] R. A. Leitgeb, M. Villiger, A. H. Bachmann, L. Steinmann, and T. Lasser, “Extended focus depth for Fourier domain optical coherence microscopy,” *Optics Letters*, vol. 31, no. 16, pp. 2450–2452, 2006.

[28] V. Garces-Chavez, D. McGloin, H. Melville, W. Sibbett, and K. Dholakia, “Simultaneous micro-manipulation in multiple planes using a self-reconstructing light beam,” *Nature*, vol. 419, no. 6903, pp. 145–147, 2002.

[29] E. J. Botcherby, R. Juskaitis, and T. Wilson, “Scanning two photon fluorescence microscopy with extended depth of field,” *Optics Communications*, vol. 268, pp. 253–260, dec 2006.

[30] T. Čižmár and K. Dholakia, “Tunable Bessel light modes: engineering the axial propagation,” *Optics Express*, vol. 17, no. 18, pp. 12688–12700, 2009.

[31] D. Gabor, “A new microscopic principle.,” *Nature*, vol. 161, no. 4098, pp. 777–778, 1948.

[32] U. Schnars and W. Jueptner, *Digital Holography. Digital Hologra Recording, Numerical Reconstruction and Related Techniques.* 2005.

[33] J. W. Goodman and R. W. Lawrence, “Digital image formation from electronically detected holograms,” *Applied Physics Letters*, vol. 11, no. 3, pp. 77–79, 1967.

[34] U. Schnars and W. Jüptner, “Direct recording of holograms by a CCD target and numerical reconstruction.,” *Applied Optics*, vol. 33, pp. 179–81, jan 1994.

[35] P. Ferraro, S. Grilli, D. Alfieri, S. De Nicola, A. Finizio, G. Pierattini, B. Javidi, G. Coppola, and V. Striano, “Extended focused image in microscopy by digital Holography,” *Optics Express*, vol. 13, pp. 6738–49, sep 2005.

[36] W. Drexler, M. Liu, A. Kumar, T. Kamali, A. Unterhuber, and R. A. Leitgeb, “Optical coherence tomography today: speed, contrast, and multimodality,” *Journal of Biomedical Optics*, vol. 19, no. 7, pp. 071412–071412, 2014.

[37] D. Hillmann, G. Franke, C. Lührs, P. Koch, and G. Hüttmann, “Efficient holoscopy image reconstruction.,” *Optics Express*, vol. 20, pp. 21247–63, sep 2012.

[38] E. Wolf, “Three-dimensional structure determination of semi-transparent objects from holographic data,” *Optics Communications*, vol. 1, no. 4, pp. 153–156, 1969.

[39] E. Wolf, “Electromagnetic diffraction in optical systems. I. An integral representation of the image field,” *Proceedings of the Royal Society of London*, vol. 19, no. February, 1959.

[40] B. E. A. Saleh and M. C. Teich, *Fundamentals of Photonics, 2nd Edition.* John Wiley & Sons, 2007.

[41] J. W. Goodman, *Introduction to Fourier Optics.* Roberts and Company Publishers, 2005.

[42] J. C. Maxwell, *A treatise on electricity and magnetism.* Clarendon Press, 1881.

[43] C. Huygens, *Traité de la Lumière.* 1678.

[44] L. Novotny, “Lecture script: Electromagnetic fields and waves,” 2013.

[45] S. L. Jacques and S. Prahl, "Optical Spectra."

[46] A. Beer, "Bestimmung der Absorption des rothen Lichts in farbigen Flüssigkeiten," *Annalen der Physik*, vol. 162, no. 5, pp. 78–88, 1852.

[47] L. V. Wang and H.-I. Wu, *Biomedical optics: principles and imaging.* John Wiley & Sons, 2012.

[48] D. Hillmann, *Holoscopy.* Springer, 2014.

[49] P. P. Ewald, "Introduction to the dynamical theory of X-ray diffraction," *Acta Crystallographica Section A*, vol. 25, no. 1, pp. 103–108, 1969.

[50] C. W. McCutchen, "Generalized aperture and the three-dimensional diffraction image: erratum," *Journal of the Optical Society of America A*, vol. 19, no. 8, p. 1721, 2002.

[51] C. M. Sparrow, "On Spectroscopic Resolving Power," *The Astrophysical Journal*, vol. 44, no. 76, p. 76, 1916.

[52] L. Rayleigh, "LVI. Investigations in optics, with special reference to the spectroscope," *Philosophical Magazine Series 5*, vol. 8, no. 51, pp. 477–486, 1879.

[53] E. Abbe, "Beiträge zur Theorie des Mikroskops und der mikroskopischen Wahrnehmung," *Archiv für Mikroskopische Anatomie*, vol. 9, no. 1, pp. 413–418, 1873.

[54] R. Heintzmann, "Lecture script: Light Microscopy," 2016.

[55] K. Wicker and R. Heintzmann, "Resolving a misconception about structured illumination," *Nature Photonics*, vol. 8, no. May, pp. 342–344, 2014.

[56] L. Schermelleh, R. Heintzmann, and H. Leonhardt, "A guide to super-resolution fluorescence microscopy," 2010.

[57] M. Heilemann, "Fluorescence microscopy beyond the diffraction limit," *Journal of Biotechnology*, vol. 149, no. 4, pp. 243–251, 2010.

[58] B. Huang, "Super-resolution optical microscopy: multiple choices," 2010.

[59] M. Walde, *High-Resolution Fluorescence Microscopy with Photoswitchable Proteins.* Master thesis, King's College London, 2010.

[60] M. G. L. Gustafsson, "Surpassing the lateral resolution limit by a factor of two using structured illumination microscopy," *Journal of Microscopy*, vol. 198, pp. 82–87, 2000.

[61] R. Heintzmann and C. Cremer, "Lateral modulated excitation microscopy: improvement of resolution by using a diffraction grating," *Proceedings of SPIE*, vol. 3568, pp. 185–196, 1999.

[62] K. Wicker, *Increasing resolution and light efficiency in fluorescence microscopy.* PhD thesis, King's College London, 2010.

[63] K. Wicker, O. Mandula, G. Best, R. Fiolka, and R. Heintzmann, "Phase optimisation for structured illumination microscopy," *Optics Express*, vol. 21, no. 2, pp. 2032–2049, 2013.

[64] S. W. Hell and J. Wichmann, "Breaking the diffraction resolution limit by stimulated emission - Stimulated-emmision-depletion fluorescence microscopy," *Optics Letters*, vol. 19, pp. 780–782, 1994.

[65] T. A. Klar and S. W. Hell, "Subdiffraction resolution in far-field fluorescence microscopy," *Optics Letters*, vol. 24, no. 14, pp. 954–956, 1999.

[66] J. M. Rust, M. Bates, and X. Zhuang, "Sub-diffraction-limit imaging by stochastic optical reconstruction microscopy (STORM)," *Nature Methods*, vol. 3, no. 10, pp. 793–796, 2006.

[67] E. Betzig, G. H. Patterson, R. Sougrat, O. W. Lindwasser, S. Olenych, J. S. Bonifacino, M. W. Davidson, J. Lippincott-Schwartz, and H. F. Hess, "Imaging intracellular fluorescent proteins at nanometer resolution," *Science*, vol. 313, p. 1642, sep 2006.

[68] S. T. Hess, T. P. K. Girirajan, and M. D. Mason, "Ultra-high resolution imaging by fluorescence photoactivation localization microscopy," *Biophysical Journal*, vol. 91, no. 11, pp. 4258–4272, 2006.

[69] S. Cox, E. Rosten, J. Monypenny, T. Jovanovic-Talisman, D. T. Burnette, J. Lippincott-Schwartz, G. E. Jones, and R. Heintzmann, "Bayesian localization microscopy reveals nanoscale podosome dynamics," *Nature Methods*, vol. 9, pp. 195–200, feb 2011.

[70] M. B. M. Meddens, B. Rieger, C. G. Figdor, A. Cambi, and K. van den Dries, "Automated podosome identification and characterization in fluorescence microscopy images.," *Microscopy and Microanalysis*, vol. 19, pp. 180–9, feb 2013.

[71] M. E. Brezinski, *Optical Coherence Tomography: Principles and Applications.* Academic Press, 2006.

[72] A. F. Fercher, W. Drexler, C. K. Hitzenberger, and T. Lasser, "Optical coherence tomography - principles and applications," *Reports on Progress in Physics*, vol. 66, pp. 239–303, 2003.

[73] K. Grieve, M. Paques, A. Dubois, J. Sahel, C. Boccara, and J. F. Le Gargasson, "Ocular tissue imaging using ultrahigh-resolution, full-field optical coherence tomography," *Investigative Ophthalmology and Visual Science*, vol. 45, no. 11, pp. 4126–4131, 2004.

[74] S.-W. Huang, A. D. Aguirre, R. A. Huber, D. C. Adler, and J. G. Fujimoto, "Swept source optical coherence microscopy using a Fourier domain mode-locked laser.," *Optics Express*, vol. 15, no. 10, pp. 6210–6217, 2007.

[75] B. Považay, A. Unterhuber, B. Hermann, H. Sattmann, H. Arthaber, and W. Drexler, "Full-field time-encoded frequency-domain optical coherence tomography," *Optics Express*, vol. 14, no. 17, pp. 7661–7669, 2006.

[76] T. Bonin, G. Franke, M. Hagen-Eggert, P. Koch, and G. Hüttmann, "In vivo Fourier-domain full-field OCT of the human retina with 1.5 million A-lines/s," *Optics Letters*, vol. 35, no. 20, pp. 3432–3434, 2010.

[77] T. S. Ralston, D. L. Marks, S. A. Boppart, and P. S. Carney, "Inverse scattering for high-resolution interferometric microscopy.," *Optics Letters*, vol. 31, no. 24, pp. 3585–7, 2006.

[78] T. S. Ralston, D. L. Marks, P. S. Carney, and S. A. Boppart, "Inverse scattering for optical coherence tomography.," *Journal of the Optical Society of America A*, vol. 23, pp. 1027–37, may 2006.

[79] J. Durnin, J. J. Miceli Jr, and J. H. Eberly, "Diffraction-free beams," *Physical Review Letters*, vol. 58, no. 15, pp. 1499–1501, 1987.

[80] D. McGloin and K. Dholakia, "Bessel beams: diffraction in a new light," *Contemporary Physics*, vol. 46, pp. 15–28, jan 2005.

[81] R. M. Herman and T. A. Wiggins, "Production and uses of diffractionless beams," *JOSA A*, vol. 8, no. 6, pp. 932–942, 1991.

[82] J. McLeod, "The axicon: a new type of optical element," *JOSA*, vol. 44, pp. 592–597, 1954.

[83] O. Brzobohatý, T. Cizmár, and P. Zemánek, "High quality quasi-Bessel beam generated by round-tip axicon.," *Optics Express*, vol. 16, no. 17, pp. 12688–12700, 2008.

[84] J. A. Davis, J. Guertin, and D. M. Cottrell, "Diffraction-free beams generated with programmable spatial light modulators," *Applied Optics*, vol. 32, no. 31, pp. 6368–6370, 1993.

[85] L. Thomson and J. Courtial, "Holographic shaping of generalized self-reconstructing light beams," *Optics Communications*, vol. 281, no. January 2008, pp. 1217–1221, 2008.

[86] N. Chattrapiban, E. A. Rogers, D. Cofield, W. T. Hill III, and R. Roy, "Generation of nondiffracting Bessel beams by use of a spatial light modulator," *Optics Letters*, vol. 28, no. 22, pp. 2183–2185, 2003.

[87] Z. Ding, H. Ren, Y. Zhao, J. S. Nelson, and Z. Chen, "High-resolution optical coherence tomography over a large depth range with an axicon lens," *Optics Letters*, vol. 27, no. 4, pp. 243–245, 2002.

[88] R. W. Gerchberg and W. O. Saxton, "Phase determination for image and diffraction plane pictures in the electron microscope," *Optik*, vol. 34, no. 3, pp. 275–284, 1971.

[89] W. O. Saxton and R. W. Gerchberg, "A practical algorithm for the determination of phase from image and diffraction plane pictures," *Optik*, vol. 35, p. 237246, 1972.

[90] O. Ripoll, V. Kettunen, and H. P. Herzig, "Review of iterative Fourier-transform algorithms for beam shaping applications," *Optical Engineering*, vol. 43, pp. 2549–2556, 2004.

[91] K. Wicker, S. Sindbert, and R. Heintzmann, "Characterisation of a resolution enhancing image inversion interferometer.," *Optics Express*, vol. 17, pp. 15491–501, aug 2009.

[92] Y. N. Denisyuk, "On the reflection of optical properties of an object in a wave field of light scattered by it," *Doklady Akademii Nauk SSSR*, vol. 144, no. 6, pp. 1275–1278, 1962.

[93] E. N. Leith and J. Upatnieks, "Reconstructed Wavefronts and Communication Theory," *Journal of the Optical Society of America A*, vol. 52, no. 10, p. 1123, 1962.

[94] A. F. Fercher, H. Bartelt, H. Becker, and E. Wiltschko, "Image formation by inversion of scattered field data: experiments and computational simulation," *Applied Optics*, vol. 18, no. 14, p. 2427, 1979.

[95] G. Burgstaller and M. Gimona, "Podosome-mediated matrix resorption and cell motility in vascular smooth muscle cells," *American Journal of Physiology-Heart and Circulatory Physiology*, vol. 288, no. 6, pp. H3001–H3005, 2005.

[96] P. Jurdic, F. Saltel, A. Chabadel, and O. Destaing, "Podosome and sealing zone: specificity of the osteoclast model," *European Journal of Cell Biology*, vol. 85, no. 3-4, pp. 195–202, 2006.

[97] A. M. Weaver, "Invadopodia: specialized cell structures for cancer invasion," *Clinical and Experimental Metastasis*, vol. 23, no. 2, pp. 97–105, 2006.

[98] Y. Calle, I. M. Anton, A. J. Thrasher, and G. E. Jones, "WASP and WIP regulate podosomes in migrating leukocytes," *Journal of Microscopy*, vol. 231, no. 3, pp. 494–505, 2008.

[99] S. Linder, "The matrix corroded: podosomes and invadopodia in extracellular matrix degradation," *Trends in Cell Biology*, vol. 17(3), pp. 107–117, 2007.

[100] S. Linder and M. Aepfelbacher, "Podosomes: adhesion hot-spots of invasive cells," *Trends in Cell Biology*, vol. 13, no. 7, pp. 376–385, 2003.

[101] K. van den Dries, M. B. M. Meddens, S. de Keijzer, S. Shekhar, V. Subramaniam, C. G. Figdor, and A. Cambi, "Interplay between myosin IIA-mediated contractility and actin network integrity orchestrates podosome composition and oscillations.," *Nature Communications*, vol. 4, p. 1412, jan 2013.

[102] S. Linder and P. Kopp, "Podosomes at a glance," *Journal of Cell Science*, vol. 118, pp. 2079–2082, 2005.

[103] A. del Rio and R. Perez-Jimenez, "Stretching single talin rod molecules activates vinculin binding," *Science*, vol. 323, no. January, 2009.

[104] J. A. DePasquale and C. S. Izzard, "Accumulation of talin in nodes at the edge of the lamellipodium and separate incorporation into adhesion plaques at focal contacts in fibroblasts.," *The Journal of Cell Biology*, vol. 113, pp. 1351–9, jun 1991.

[105] J. D. Humphries, P. Wang, C. Streuli, B. Geiger, M. J. Humphries, and C. Ballestrem, "Vinculin controls focal adhesion formation by direct interactions with talin and actin.," *The Journal of Cell Biology*, vol. 179, pp. 1043–57, dec 2007.

[106] C. Badowski and G. Pawlak, "Paxillin phosphorylation controls invadopodia/podosomes spatiotemporal organization," *Molecular Biology of the Cell*, vol. 19, no. February, pp. 633–645, 2008.

[107] N. O. Deakin and C. E. Turner, "Paxillin comes of age," *Journal of Cell Science*, vol. 121, pp. 2435–44, aug 2008.

[108] C. Luxenburg, D. Geblinger, and E. Klein, "The architecture of the adhesive apparatus of cultured osteoclasts: from podosome formation to sealing zone assembly," *PLoS ONE*, vol. 2, no. 1, p. e179, 2007.

[109] E. Dougherty, "An introduction to morphological image processing," in *Tutorial Texts in Optical Engineering*, SPIE, 1992.

[110] A. W. Bowman and A. Azzalini, *Applied smoothing techniques for data analysis.* Oxford University Press, 1997.

[111] T. M. Svitkina and G. G. Borisy, "Arp2/3 complex and actin depolymerizing factor/cofilin in dendritic organization and treadmilling of actin filament array in lamellipodia," *The Journal of cell biology*, vol. 145, no. 5, pp. 1009–1026, 1999.

[112] L. Blanchoin, K. J. Amann, H. N. Higgs, J.-B. Marchand, D. A. Kaiser, and T. D. Pollard, "Direct observation of dendritic actin complex and WASP / Scar proteins," *Nature*, vol. 171, no. 1994, pp. 1007–1011, 2000.

[113] C. Gawden-Bone, Z. Zhou, E. King, A. Prescott, C. Watts, and J. Lucocq, "Dendritic cell podosomes are protrusive and invade the extracellular matrix using metalloproteinase MMP-14," *Journal of Cell Science*, vol. 123, no. 9, p. 1427, 2010.

[114] L. Ma and D. Dolphin, "The metabolites of dietary chlorophylls," 1999.

[115] S. Hörtensteiner and B. Kräutler, "Chlorophyll breakdown in higher plants," 2011.

[116] S. Hörtensteiner, "Review Chlorophyll breakdown in higher plants and algae," *Cellular and Molecular Life Sciences*, vol. 56, pp. 330–347, 1999.

[117] P. Matile, S. Hortensteiner, H. Thomas, S. Hörtensteiner, and H. Thomas, "Chlorophyll degradation," *Annual Review of Plant Physiology and Plant Molecular Biology*, vol. 50, no. 1, pp. 67–95, 1999.

[118] S. Banala, S. Moser, T. Müller, C. Kreutz, A. Holzinger, C. Lütz, and B. Kräutler, "Hypermodified fluorescent chlorophyll catabolites: source of blue luminescence in senescent leaves," *Angewandte Chemie International Edition*, vol. 49, no. 30, pp. 5174–5177, 2010.

[119] Y.-J. Park, W.-S. Kim, S.-H. Ko, D.-S. Lim, H.-J. Lee, W.-Y. Lee, and D. W. Lee, "Separation and Characterization of Chlorophyll Degradation Products in Silkworm," *Journal of Liquid Chromatography & Related Technologies*, vol. 26, no. 19, pp. 3183–3197, 2003.

[120] J. P. Thornber, "Chlorophyll-proteins: light-harvesting and reaction center components of plants," *Annual Review of Plant Physiology*, vol. 26, no. 1, pp. 127–158, 1975.

[121] K. M. Matti, S. S. Singh, C. J. Savanurmath, and S. B. Hinchigeri, "A unique red fluorescent protein of silkworm bearing two photochromic moieties.," *Photochemical & Photobiological Sciences*, vol. 8, no. 10, pp. 1364–72, 2009.

[122] P. M. Campbell, A. T. Cao, E. R. Hines, P. D. East, and K. H. J. Gordon, "Proteomic analysis of the peritrophic matrix from the gut of the caterpillar, Helicoverpa armigera," *Insect Biochemistry and Molecular Biology*, vol. 38, no. 10, pp. 950–958, 2008.

[123] Y. Pauchet, A. Muck, A. Svatos, D. G. Heckel, and S. Preiss, "Mapping the larval midgut lumen proteome of Helicoverpa armigera, a generalist herbivorous insect," *Journal of Proteome Research*, vol. 7, no. 4, pp. 1629–1639, 2008.

[124] Y. Pauchet, A. Muck, A. Svatos, and D. G. Heckel, "Chromatographic and electrophoretic resolution of proteins and protein complexes from the larval midgut microvilli of Manduca sexta," *Insect Biochemistry and Molecular Biology*, vol. 39, no. 7, pp. 467–474, 2009.

[125] G. N. Pandian, T. Ishikawa, M. Togashi, Y. Shitomi, K. Haginoya, S. Yamamoto, T. Nishiumi, and H. Hori, "Bombyx mori midgut membrane protein P252, which binds to Bacillus thuringiensis Cry1A, is a chlorophyllide-binding protein, and the resulting complex has antimicrobial activity," *Applied and Environmental Microbiology*, vol. 74, no. 5, pp. 1324–1331, 2008.

[126] C. Angelucci, G. A. Barrett-Wilt, D. F. Hunt, R. J. Akhurst, P. D. East, K. H. J. Gordon, and P. M. Campbell, "Diversity of aminopeptidases, derived from four lepidopteran gene duplications, and polycalins expressed in the midgut of Helicoverpa armigera: Identification of proteins binding the δ-endotoxin, Cry1Ac of Bacillus thuringiensis," *Insect Biochemistry and Molecular Biology*, vol. 38, no. 7, pp. 685–696, 2008.

[127] B. Mauchamp, C. Royer, A. Garel, A. Jalabert, M. Da Rocha, A.-M. Grenier, V. Labas, J. Vinh, K. Mita, and K. Kadono, "Polycalin (chlorophyllid A binding protein): a novel, very large fluorescent lipocalin from the midgut of the domestic silkworm Bombyx mori L," *Insect Biochemistry and Molecular Biology*, vol. 36, no. 8, pp. 623–633, 2006.

[128] C. Bordier, R. J. Etges, J. Ward, M. J. Turner, and M. L. C. De Almeida, "Leishmania and Trypanosoma surface glycoproteins have a common glycophospholipid membrane anchor," *Proceedings of the National Academy of Sciences*, vol. 83, no. 16, pp. 5988–5991, 1986.

[129] A. Badgaa and W. Boland, "Chlorophyll catabolites in the frass of the small tortoiseshell caterpillars (Aglais urticae L.)," *Mongolian Journal of Chemistry*, vol. 14, no. 40, pp. 46–50, 2013.

[130] A. Badgaa, A. Jia, K. Ploss, and W. Boland, "Chlorophyll Degradation in the Gut of Generalist and Specialist Lepidopteran Caterpillars," *Journal of Chemical Ecology*, vol. 40, no. 11-12, pp. 1232–1240, 2014.

[131] A. A. Krasnovsky, K. V. Neverov, S. Y. Egorov, B. Roeder, and T. Levald, "Photophysical studies of pheophorbide a and pheophytin a. Phosphorescence and photosensitized singlet oxygen luminescence," *Journal of Photochemistry and Photobiology, B: Biology*, vol. 5, no. 2, pp. 245–254, 1990.

[132] X. Tang, D. Freitak, H. Vogel, L. Ping, Y. Shao, E. A. Cordero, G. Andersen, M. Westermann, D. G. Heckel, and W. Boland, "Complexity and variability of gut commensal microbiota in polyphagous lepidopteran larvae," *PLoS ONE*, vol. 7, no. 7, 2012.

[133] F. V. Vencl, N. E. Gómez, K. Ploss, and W. Boland, "The chlorophyll catabolite, pheophorbide a, confers predation resistance in a larval tortoise beetle shield defense," *Journal of Chemical Ecology*, vol. 35, no. 3, pp. 281–288, 2009.

[134] H.-W. Lu-Walther, M. Kielhorn, R. Förster, A. Jost, K. Wicker, and R. Heintzmann, "fastSIM: a practical implementation of fast structured illumination microscopy," *Methods and Applications in Fluorescence*, vol. 3, no. 1, p. 014001, 2015.

[135] E. H. K. Stelzer, "Light sheet fluorescence microscopy for quantitative biology," *Nature Methods*, vol. 12, no. 1, pp. 23–26, 2015.

[136] N. Ji, D. E. Milkie, and E. Betzig, "Adaptive optics via pupil segmentation for high-resolution imaging in biological tissues," *Nature Methods*, vol. 7, no. 2, pp. 141–147, 2009.

[137] J. Leach, G. M. Gibson, M. J. Padgett, E. Esposito, G. McConnell, A. J. Wright, and J. M. Girkin, "Generation of achromatic Bessel beams using a compensated spatial light modulator.," *Optics Express*, vol. 14, no. 12, pp. 5581–5587, 2006.

[138] C. Blatter, B. Grajciar, C. M. Eigenwillig, W. Wieser, B. R. Biedermann, R. Huber, and R. A. Leitgeb, "Extended focus high-speed swept source OCT with self-reconstructive illumination," *Optics Express*, vol. 19, no. 13, pp. 12141–12155, 2011.

[139] M. Kanka, R. Riesenberg, and H. J. Kreuzer, "Reconstruction of high-resolution holographic microscopic images.," *Optics Letters*, vol. 34, pp. 1162–4, apr 2009.

[140] U. S. Kamilov, I. N. Papadopoulos, M. H. Shoreh, A. Goy, C. Vonesch, M. Unser, and D. Psaltis, "Learning approach to optical tomography," *Optica*, vol. 2, no. 6, p. 517, 2015.

[141] K. Egodage, S. Dochow, T. Bocklitz, O. Chernavskaia, C. Matthaeus, M. Schmitt, and J. Popp, "The combination of optical coherence tomography and Raman spectroscopy for tissue characterization," *Journal of Biomedical Photonics & Engineering*, jun 2015.

[142] N. Baddour, "Operational and convolution properties of two-dimensional Fourier transforms in polar coordinates," *JOSA A*, vol. 26, no. 8, pp. 1767–1777, 2009.

Acknowledgement

I would like to express my sincerest gratitude to Prof. Dr. Rainer Heintzmann for all his time and dedication and for the freedom and inspiration he offers to his group members. I feel privileged to have had such a passionate and open-minded scientist as mentor and supervisor. The same holds for Dr. Kai Wicker who always had an open ear for my questions and has great talent for explaining complicated scientific matters. He provided the design for the custom-built UZI and helped with the theoretical considerations.

I am very grateful for the friendly and constructive atmosphere in Prof. Heintzmann's research group and would like to thank all my colleagues. I had the best office mates a PhD student can ask for and will miss the presence, advice and Gebäckmischung of Aurélie Jost, Sapna Shukla and Stephan Roth. Aurélie also worked with me on the SLM characterization and Bessel illumination. I also thank Dr. Martin Kielhorn who helped with drivers and triggering of devices and with critical questions, Robert Kretschmer for his invaluable technical support, Dr. Christian Karras for good chats over coffee or beer, Walter Müller and Dr. Elena Tolstik for advice and uplifting conversations and René Richter for his help with CUDA errors.

I am fortunate to have found myself working with a number of talented and kind researchers who have shared their knowledge and time with me. I owe a tremendous debt of gratitude to Dr. Martin Hammer and Sven Peters from the Experimental Ophtalmology in Jena, my co-authors Dr. Susan Cox, Prof. Gareth Jones, Dr. James Moneypenny from the Randall Division at King's College London and Dr. Amarsanaa Bagdaa and Prof. Dr. Wilhelm Boland from the Max Planck Institute for Chemical Ecology in Jena.

I thank Prof. Gereon Hüttmann's group at the BMO Lübeck whose work has inspired parts of this dissertation. In particular I wish to thank Dr. Dierck Hillmann, Gesa Franke and Dr. Tim Bonin for their advice and constructive discussions. Dr. Bettina Heise from the Johannes Kepler University Linz kindly lent me scattering test samples. I thank Prof. Dr. Anne Sentenac from the Institut Fresnel in Marseille for fruitful discussions and her help in the development of the IFTA. I am grateful to Prof. Richard Kowarschik from the Insitute of Applied Optics in Jena for crucial insights into holographic theory and Anka Schwuchow from IPHT for kindly lending me her infrared viewing card.

Furthermore I am deeply indebted to our secretaries Antje Raabe, Marion Krause and Bärbel Schäfer who helped me to navigate through the trials and tribulations of university bureaucracy. Monika Heinemann has been very supportive and patient throughout my employment at the university and greatly facilitated my parental leave. Benita Göbel always had a smile, gummy bear or a hard to get publication for me.

I thank Bea, Christian, Fabi, Heinrich, Lina and Nina for proof-reading chapters and sharing their individual expertise with me.

None of this would have been possible without my parents. I am eternally grateful for their constant support and unquestioning love. Last and certainly not least, I want to thank my boyfriend, Johann, for both support and occasional distraction through the stressful times of this thesis and my *sun* Konstantin without whom this thesis would have been finished much earlier.

Curriculum Vitae

Born 17th June 1987, Berlin

Education

05/2011–06/2017	PhD candidate Institute of Physical Chemistry, Friedrich-Schiller-Universität Jena and Leibniz Institute of Photonic Technology Jena
09/2009–11/2010	Master of Research in *Molecular Biophysics*, King's College London, UK
10/2006–09/2009	Bachelor of Science in *Biophysics* (minor: *Physics*), Humboldt-Universität zu Berlin
08/2001–06/2006	Abitur, Heinrich-Hertz-Gymnasium, Berlin

Career

from 01/2017	Postdoctoral Scientist, Light Microscopy Platform, Berlin Institute of Medical Systems Biology, Max Delbrück Center for Molecular Medicine in the Helmholtz Association, Berlin
11/2010–11/2016	Research and Teaching Assistant Nanobiophotonics, Institute of Physical Chemistry, Friedrich-Schiller-Universität Jena
09/2015–09/2016	Parental Leave
09/2014–09/2015	General Conference Chair of DoKDoK2015 (Doctoral conference on optics and photonics)

Ort, Datum

Unterschrift

Selbständigkeitserklärung

Ich erkläre, dass ich die vorliegende Arbeit selbstständig und unter Verwendung der angegebenen Hilfsmittel, persönlichen Mitteilungen und Quellen angefertigt habe.

Ort, Datum	Unterschrift